

## Chapter 4

---

# POROUS SILICON MICROCAVITIES

Claudio Vinegoni

*Department of Physics and Astronomy, University of Pittsburgh,  
Pittsburgh, Pennsylvania, USA*

Massimo Cazzanelli

*Department of Physics, Trinity College, Dublin, Ireland*

L. Pavesi

*INFM and Dipartimento di Fisica, Università di Trento, Trento,  
Italy*

### Contents

1. Introduction . . . . .	124
2. Porous Silicon . . . . .	125
2.1. Fabrication of Porous Silicon . . . . .	125
2.2. Structure of Porous Silicon . . . . .	130
2.3. Chemical Properties of Porous Silicon . . . . .	137
2.4. Optical Properties . . . . .	141
2.5. Luminescence in Porous Silicon . . . . .	143
3. Dielectric Multilayers . . . . .	146
3.1. Thin Slab . . . . .	147
3.2. Bragg Reflectors . . . . .	148
3.3. Fabry-Perot Interference Filters . . . . .	149
4. Semiconductor Microcavities . . . . .	151
4.1. Weak Coupling Mode . . . . .	152
4.2. Strong Coupling Mode . . . . .	152
5. Porous Silicon Multilayers . . . . .	153
5.1. Producing Porous Silicon Multilayers . . . . .	155
5.2. Bragg Reflectors . . . . .	158
5.3. Random Bragg Reflectors . . . . .	159
5.4. Fabry-Perot Filters . . . . .	161
5.5. Random Fabry-Perot Filters . . . . .	162
6. Porous Silicon Microcavities . . . . .	164
6.1. Physical Properties . . . . .	164
6.2. Aging Effects in Porous Silicon Microcavities . . . . .	167

6.3.	Simulation of the Optical Properties of Porous Silicon Microcavities . . . . .	168
6.4.	Time-Resolved Spectroscopy in Porous Silicon Microcavities . . . . .	169
6.5.	Temperature Dependence of Porous Silicon Microcavities .	175
6.6.	Coupled Porous Silicon Microcavities . . . . .	178
7.	Applications of Porous Silicon Multilayers and Microcavities .	182
7.1.	Waveguides . . . . .	182
7.2.	Enhancement of Weak Absorption Signals . . . . .	183
7.3.	Optical Nonlinearities . . . . .	183
7.4.	Resonant Cavity Light-Emitting Diodes . . . . .	183
7.5.	Optical Sensor . . . . .	185
7.6.	Color-Sensitive Photodiodes . . . . .	185
7.7.	Metal–Porous Silicon Microcavities . . . . .	186
8.	Conclusions . . . . .	187
	Acknowledgments . . . . .	188
	References . . . . .	188

## 1. INTRODUCTION

The end of the twentieth century has seen a progressive lowering in dimensionality of semiconductor systems. Quantum wells, quantum wires, and quantum dots were exotic terms a decade ago, whereas now they are at the very basis of many devices, for example, single electron memories or transistors. At the same time, new applications for silicon have been found either in the form of an alloy with germanium for high-frequency applications or as materials for photonics applications. This last aspect is the focus of this chapter.

The promotion of silicon from a key material for microelectronics to an interesting and competitive material occurred because photonics applications are based on the fact that the spontaneous emission of a material depends on the coupling between the initial and final states of the optical emission process, that is, on the coupling between the electronic systems and the photons. This is stated by the Fermi golden rule, which says that the spontaneous emission rate  $R_{\text{sp}}(\hbar\omega)$  of a material is given by

$$R_{\text{sp}}(\hbar\omega) \propto \Gamma(\hbar\omega) \times M_{\text{eh}}(\hbar\omega) \quad (1)$$

where  $\Gamma(\hbar\omega)$  is the photon mode density and  $M_{\text{eh}}(\hbar\omega)$  is the element of the dipole matrix between the initial state and the final state of the optical transition. By reducing the dimensionality of both the electronic system and the optical system it is possible to change dramatically the spontaneous emission of silicon.

The first exploitation of this fact was in reducing the dimensionality of the electronic system in silicon by using an inexpensive and easy technique. In fact, the first success in the improvement of silicon emission properties was the discovery of efficient light emission in porous silicon (PS) where nanocrystalline Si is

formed and quantum confinement of photoexcited carriers yields a band gap widening and an increased transition rate [1]. These observations have promoted a wide interest worldwide with the development of many other low-dimensional silicon-based systems: nanocrystals, quantum wells, superlattices, nanometric multilayers of amorphous material, and so forth.

The second accomplishment was made by Pavesi's group in 1995 with the development of all-porous silicon microcavities (PSM) in which the active PS is placed in an optical resonator formed by two PS mirrors (dielectric Bragg reflectors, DBR) [2, 3]. In this system not only is the electronic system of silicon changed through the use of porous silicon, but also the photonic system is promoted to lower dimensionality within a Fabry-Perot structure. Only those photons with the same wavelength as the Fabry-Perot resonance can propagate through the structure and couple with the electronic transitions. A one-dimensional confinement of the photons is indeed reached.

The use of PSM thus put to full exploitation the possibility of using Eq. (1) to change the spontaneous emission properties of silicon. The aim of this chapter is to show how this is feasible and which interesting and new properties these systems show.

The chapter is organized as follows:

- Section 2 presents the structure and optical properties of PS.
- Section 3 gives a general introduction to dielectric multilayers.
- Section 4 introduces semiconductor microcavities.
- Section 5 discusses PS multilayers.
- Section 6 deals with PS microcavities.
- Section 7 presents some applications of PS microcavities.
- Conclusions are drawn in Section 8.

## 2. POROUS SILICON

### 2.1. Fabrication of Porous Silicon

Porous silicon was discovered in 1956 by Uhlir [4] while performing electropolishing experiments on silicon wafers using an hydrofluoric acid (HF)-containing electrolyte. He found that, on increasing the current over a certain threshold, a partial dissolution of the silicon wafer started to occur. PS formation is then obtained by electrochemical dissolution of Si wafers in aqueous or ethanoic HF solutions.

#### 2.1.1. How to Produce Porous Silicon

A quite simple apparatus can be used to produce PS, and the typical setup is shown in Figure 1 [5]. The anode is the silicon wafer itself; the cathode can be a platinum spiral or a circular grid; the electrolyte is composed of high-purity HF in 40% aqueous solution diluted in ethanol ( $C_2H_5OH$ ) at different concentrations. The dilution is necessary because of the hydrophobic character of the clean Si surface: in this way it is possible to increase the wettability of the PS surface. In fact, ethanoic solutions infiltrate the pores; on the contrary, purely aqueous HF solutions do not. This is very important for the lateral homogeneity and the uniformity of the PS layer in depth. In addition, during the reaction there is hydrogen release. Bubbles form and stick on the Si surface in pure aqueous solutions; they can be removed if ethanol (or some other surfactant) is present. For the same reason, a careful design of the anodization cell is necessary, to promote hydrogen-bubble removal. Moreover, it has been observed that lateral homogeneity and surface roughness can be reduced by increasing the electrolyte viscosity and by decreasing the temperature or by introducing glycerol into the HF solution [6].

The process of growth is obtained by controlling either the anodic current or the potential. The practice of working

with constant current is widely spread, because it allows better control of the porosity, thickness, and reproducibility of the PS layer. Different kinds of cells can be used for the production of PS.

The first kind of cell is presented in Figure 2 [7]. The Si wafer acts as the anode; the cathode is generally made of platinum or other HF-resistant and conducting material. The cell body is usually made of a highly acid-resistant polymer such as Teflon. In this cell PS is formed all over the wafer surface exposed to HF. The advantage of this cell geometry is the simplicity of the equipment. On the other hand, the main drawback is the inhomogeneity in the porosity and the thickness of the PS layers. The presence of a difference in the potential between the top (point A in Fig. 2) and the bottom (point B in Fig. 2) of such a cell leads to different values of the local current density.

The second type of cell is the single cell approach that uses a back-side contact and is shown in Figure 1. In this cell, the Si wafer is placed on a copper disk and sealed through an O-ring so that only the front side of the sample is exposed to the electrolyte. The copper disk has to be cleaned with a lapping machine to remove the oxide film that forms itself after many etching processes. When a Si wafer with high resistivity (i.e., more than a few milliohms per centimeter) is used, a high-dose implantation on the back surface of the wafer is required to improve the electrical contact between the wafer and the copper disk. This geometry is particularly indicated for a uniform illumination of the sample during the etching.

The third type of cell is a double tank geometry with an electrolytic back-side contact. This cell (Fig. 3 [7]) consists of two half-cells that contain the platinum electrodes; the Si wafer is used to separate the two half-cells. The HF solution is made to flow by HF-resistant pumps. In this way it is possible to remove the gas bubbles and to avoid the decrease in the local concentration of HF. The current flows from one electrode to the other through the Si wafer. In this configuration the back side of the Si wafer

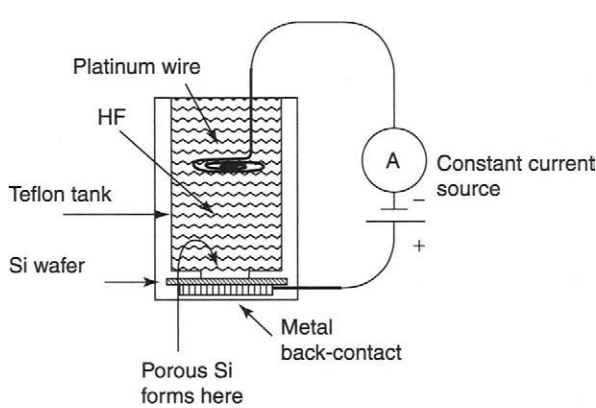


Fig. 1. Schematic drawing of the electrochemical cell used for the preparation of porous silicon. Adapted from [5].

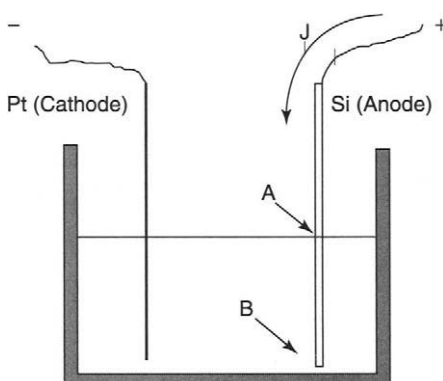


Fig. 2. Cross-sectional view of a lateral anodization cell. The silicon wafer acts as the anode. Reprinted with permission after Ref. [7].

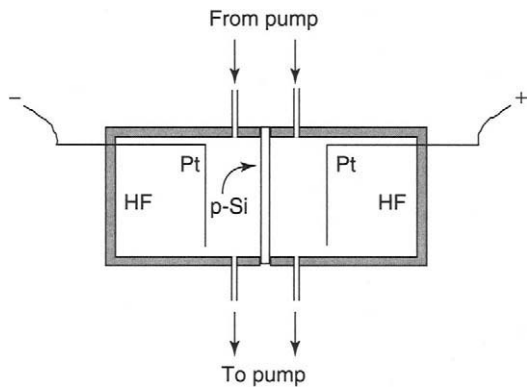


Fig. 3. Cross-sectional view of a double tank anodization cell. The Si wafer is used to separate the two half-cells. Reprinted with permission after Ref. [7].

acts as a secondary cathode where proton reduction takes place leading to hydrogen evolution. The front side of the wafer acts as a secondary anode, where PS is formed. Because the back-side contact is made electrolytically, no metallization is required, but a high-dose implantation is still necessary for highly resistive wafers. If illumination is required, the material used in the cell should be Plexiglas, which is transparent and HF resistant (up to 15% HF). With this cell, both front- and back-side illumination is possible.

#### 2.1.2. *i*-V Characteristics

It is known that applying a potential to silicon leads to an external current flowing through the system. Figure 4 shows the characteristic *i*-V curves for *n*- and *p*-type doped Si in aqueous HF [8]. Some similarities exist between the *i*-V curves shown in Figure 4 and those of a semiconductor-electrolyte interface, which behaves as a normal Schottky diode barrier. Some differences exist too: First, even though the type of majority carriers changes between *n*- and *p*-types, the chemical reactions at the interface remain the same. Second, reverse-bias dark currents have been reported at least three orders of magnitude higher than those normally expected for Schottky diodes.

Both *n*- and *p*-type silicon are stable under cathodic polarization. The only important cathodic reaction is the reduction of water at the Si-HF interface, with the contemporary formation of gaseous hydrogen. This reaction occurs only at high cathodic overpotentials or, using Schottky-diode terminology, at reverse-biased breakdown.

Dissolution of silicon occurs only under anodic polarization. At high anodic overpotentials the Si surface undergoes electropolishing. On the contrary, at low anodic overpotentials the surface morphology is dominated by a

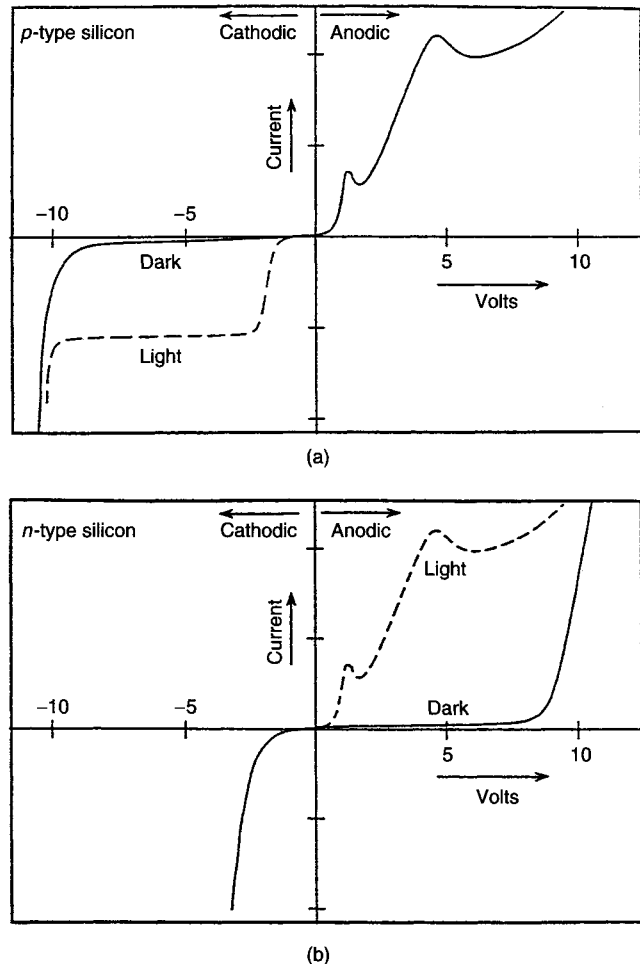


Fig. 4. Characteristic *i*-V curves for *n*- and *p*-type doped Si in aqueous HF. Reprinted with permission after Ref. [8].

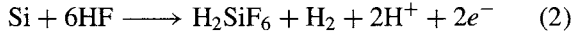
dense array of channels penetrating deeply into the bulk of the Si [9]. Pore formation occurs only during the initial rising part of the *i*-V curve, for a potential value below the potential of the small sharp peak (see Fig. 4 [8]). The current peak is named as electropolishing peak.

The quantitative values of the *i*-V curves, as well as the values corresponding to the electropolishing peak, depend on the etching parameters and wafer doping. For *n*-type substrates, this typical *i*-V behavior is observed only under illumination because hole supply is needed. We refer the reader interested in the details of these features to more specialized papers [8, 10, 11].

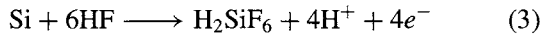
#### 2.1.3. Porous Silicon Formation Chemistry

Several different mechanisms regarding the dissolution chemistry of silicon have been proposed, but it is generally accepted that holes are required for both electropolishing and pore formation. During the process of pore formation two hydrogen atoms are released for every Si atom

that reacts [12, 13]. The hydrogen creation decreases approaching the electropolishing regime and stops during electropolishing. Two electrons for each Si atom that reacts are consumed during the pore formation, and about four electrons are used under the electropolishing regime [11, 12, 14]. The global anodic semireactions can be written during pore formation as



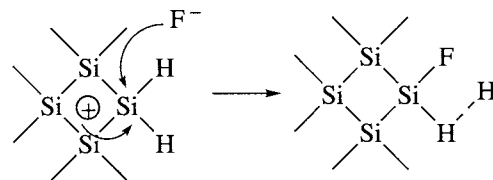
and during electropolishing as



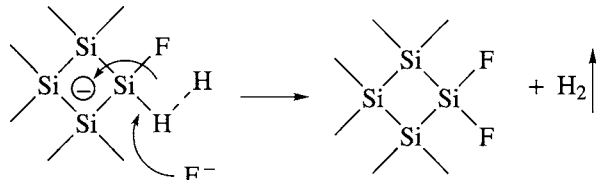
In both cases, the final and stable product for Si in HF is  $\text{H}_2\text{SiF}_6$  or some of its ionized forms; it follows

that during pore formation only two of the four available Si electrons participate in an interface charge transfer, whereas the remaining two undergo a corrosive hydrogen formation. During electropolishing all four Si electrons are electrochemically active.

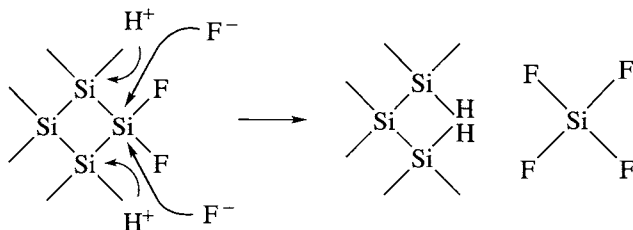
Among the various models proposed for the Si dissolution reaction, the mechanism presented by Lehmann and Gösele [15] (shown in Fig. 5 [16]) is the most accepted in the PS community. The mechanism is based on a surface-bound oxidation scheme, with hole capture and subsequent electron injection, which leads to the divalent Si oxidation state. According to the model, the Si hydride bonds passivate the Si surface unless a hole is available. Once PS is formed, the interpore region is depleted of holes as evidenced by the high resistivity of PS ( $\simeq 10^6 \Omega \text{ cm}$ , similar



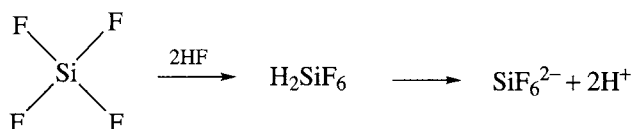
Hole injection and attack on a Si–H bond by a fluoride ion



Second attack by a fluoride ion with hydrogen evolution and electron injection into the substrate



HF attack to the Si–Si backbonds. The remaining Si surface atoms are bonded to the H atoms and a silicon tetrafluoride molecule is produced



The silicon tetrafluoride reacts with two HF molecules to give  $\text{H}_2\text{SiF}_6$  and then ionizes.

Fig. 5. Dissolution mechanism proposed by Lehmann and Gösele [15]. Reprinted with permission after Ref. [16].

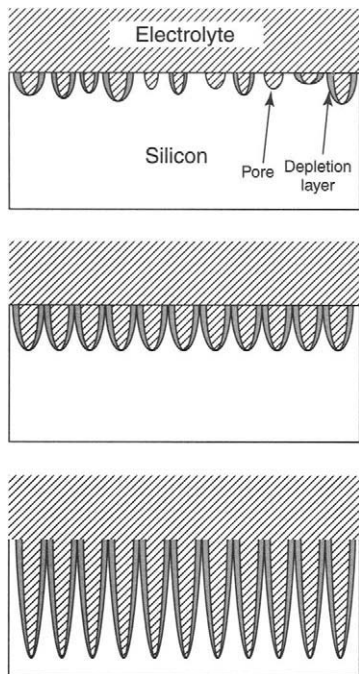


Fig. 6. Pore formation in PS: (top) the initial stage, where the pores develop randomly on the Si surface; (middle) the self-regulating process. When the depletion zones around each pore overlap, the pore growth changes from an isotropic growth to a highly directional growth. (bottom) how the dissolution advances only at the pore tips. Reprinted with permission after Ref. [17].

to intrinsic Si) [11]. Further dissolution occurs only at the pore tips, where enough holes are available (see Fig. 6 [17]). In this way the etching of PS proceeds in depth with an overall directionality that follows the anodic current paths inside Si. Once a PS layer is formed, no more electrochemical etching occurs but a slow chemical one starts because of the permanence in HF.

#### 2.1.4. Etching Parameters

The main requirements for PS formation are as follows:

1. The Si wafer must be anodically biased. This corresponds to forward biasing for *p*-type doped Si, reverse biasing for *n*-type doped Si.
2. For *n*-type doped and semi-insulating *p*-type doped Si, light must be supplied.
3. Current densities below the critical value  $j_{PS}$  must be used.

The first two conditions are due to the fact that holes are consumed during Si etching. When the third condition

is violated, the reaction is limited by mass transfer to the solution: holes pile up at the Si–HF interface and electropolishing occurs.

For all three conditions mentioned the holes play an important role; in fact, PS formation is a self-regulated mechanism, with hole depletion as the limiting agent. The dissolution reaction begins at defects on the Si wafer surface; the pores are formed and their walls are eroded until they are emptied of the holes. This formation process passivates them from further attack, and the reaction proceeds at the pore end (Fig. 6). Among the various models proposed to explain hole depletion [8], two are worth mentioning. Beale et al. [11] attribute the absence of holes in PS to the overlap of the depletion regions formed on the pore walls in a Schottky diode picture of the Si–electrolyte interface. Lehmann and Gösele [15] proposed the quantum model, by observing that the photoluminescence data are blueshifted with respect to the Si gap because of exciton confinement similar to the “particle-in-a-box” quantum problem. In fact, the difference between the energies of the crystalline silicon and the PS acts as a barrier for hole diffusion from the crystalline silicon to the pores.

In accordance with the previous mechanisms, Lehmann [18] proposed that the depletion width at the silicon–electrolyte interface depends on the doping. The depletion width is quite large for *n*-type doped Si, and this fact accounts for the formation of macropores; it exhibits a smaller value in *n*<sup>+</sup>-type and *p*<sup>+</sup>-type doped Si, which leads to mesopores, and it is zero for *p*-type doped Si. On the other side, the depletion caused by the quantum confinement is present independently of the substrate type, resulting in the formation of micropores. In this way the macropores or mesopores, typical of *n*<sup>−</sup>-type, *n*<sup>+</sup>-type, and *p*<sup>+</sup>-type doped Si, are coated by micropores.

The overall etching process is self-adjusting, and the average pore size is given by the electrochemical parameters only.

The quantum confinement effect yields microporous Si, with pore diameters below 2 nm. For a thin depletion layer, holes tunnel from Si to the electrolyte; this leads to the formation of mesopores, whose diameter ranges from 2 to 50 nm.

With thicker depletion, pore sizes pass from 50 nm to several micrometers and are independent of the layer thickness. These structures are named macropores. As the light emission originates in microporous Si, samples made from lightly *p*-type doped Si wafers have the best luminescent properties.

PS is macroscopically and empirically characterized by its porosity  $P$ , defined as the fraction of voids inside the porous layer versus the starting silicon; it is usually measured through a gravimetric technique that implies the measurement of the starting weight of the sample and the

subsequent weight of the sample after the etching:

$$P = \frac{W_1 - W_2}{W_1 - W_3} \quad (4)$$

where  $W_1$ ,  $W_2$ , and  $W_3$  are, respectively, the weight of the wafer before the electrochemical etch, after the electrochemical etch, and after the porous layer has been removed; the removal is made through a dip for some minutes in an aqueous solution of KOH (3% in volume), which leads to a selective removal of the PS layer without reacting with the bulk crystalline silicon.

Different techniques are employed to determine the porous layer thickness  $d$ . From the gravimetric measurements,

$$d = \frac{W_1 - W_3}{\rho S} \quad (5)$$

where  $\rho$  is the silicon density and  $S$  is the etched surface, or a measure, with a profilometer, of the depth of the hole left after dissolution of the PS layer. Optical and electrical microscope observations are also reported.

As a by-product of such measurements, a profile of the hole is obtained; an example of this is shown in Figure 7 [2].

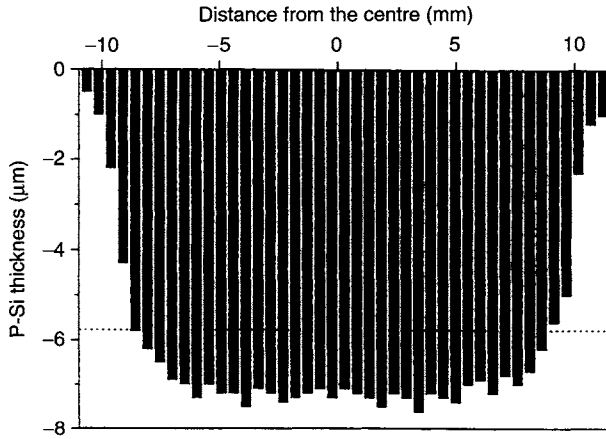


Fig. 7. Depth profile of the hole, left after dissolution, of the PS layer formed on a  $7 \Omega \text{ cm}$  substrate. The profile is taken on a diameter. The depths were determined by scanning electron microscopy measurements. Reprinted with permission after Ref. [2].

The PS formation is influenced by the following parameters:

- the substrate doping;
- the current density (which determines the depletion width and the carrier injection rate);
- the HF concentration (the higher the concentration, the lower the pore sizes and the porosity)—HF concentration determines  $j_{PS}$ , that is, the upper limit to current density values; with a fixed and low HF concentration the range over which the current density can be varied is short, and it becomes wider by increasing the HF concentration;
- the solvent in which the HF is diluted—because PS is organophilic and hydrophobic, the use of ethanol guarantees a higher homogeneity as a result of better wettability of the surface than with deionized water;
- the etching time—longer etching times lead to thicker layers, but for long times an anisotropy in depth of the layer due to the chemical action of the electrolyte is introduced;
- the illumination during the etch.

The porosity, thickness, pore diameter, and microstructure of PS depend on the anodization conditions. These conditions include HF concentration, current density, wafer type and resistivity, anodization duration, illumination (required for  $n$ -type silicon and semi-insulating  $p$ -type silicon), temperature, ambient humidity, and drying conditions (see Table I).

For  $p$ -type doped substrates and for a given HF concentration the porosity increases with increasing current density. For fixed current density, the porosity decreases with HF concentration (see Fig. 8 [7, 19]). Fixing the HF concentration and the current density, the porosity increases with the thickness. This happens because of the extra chemical dissolution of the PS layer in HF. To have a thicker layer, a longer anodization time is required. A longer permanence time of Si in HF solution results in a higher mass of chemically dissolved silicon. This effect is more important for lightly doped Si, whereas it is almost negligible for heavily doped Si. This is due to the lower specific surface area.

Table I Effect of Anodization Parameters on PS Formation

An increase of... yields	Porosity	Etching rate	Critical current
HF concentration	Decreases (see text)	Decreases	Increases
Current density	Increases	Increases	—
Anodization time	Increases	Almost constant	—
Temperature	—	—	Increases
Wafer doping ( $p$ -type)	Decreases	Increases	Increases
Wafer doping ( $n$ -type)	Increases	Increases	—

Source: Adapted from [16].

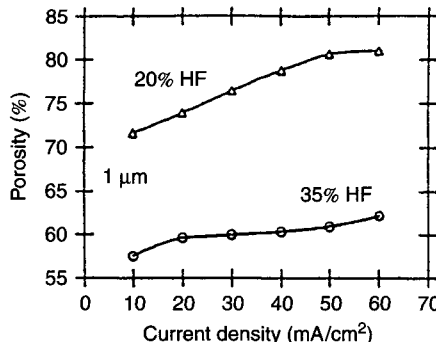


Fig. 8. Porosity as a function of the current densities for different HF concentrations: (top) for lightly doped and (bottom) for highly doped *p*-type silicon substrate. Reprinted with permission after Ref. [2, 19] and [7], respectively.

Samples of porosity between 20 and 75% can be fabricated with ease. Because of the fact that the fragile Si skeleton is unable to withstand the large capillary forces that are present within the pores during drying, higher porosities are difficult to achieve. What happens is that the samples crack and peel from the substrate. Sample cracking can be avoided via various drying techniques that have been proposed: supercritical drying [20], freeze-drying [21], the use of benzene during sample rinsing [22], and a simple slow rate of evaporation.

### 2.1.5. Drying of the Samples

An important step in the fabrication process of high-quality PS layers is the drying recipe employed immediately after etching the wafer. It has been reported several times that the formation of PS with high porosity (greater than 70%) and/or thickness (on the order of microns) leads to a systematic cracking of the layer during the evaporation of the solvent. A typical example of cracking pattern is reported in Figure 9 [16]. The origin of the cracking is the large capillary stress associated with the evaporation from the pores. During the evaporation a gas–liquid interface forms inside the pores and a pressure drop  $\Delta p$  across the gas–liquid interface occurs.  $\Delta p$  is given by

$$\Delta p = \gamma \frac{S \cos \Theta}{P} \quad (6)$$

where  $\gamma$  is the liquid surface tension,  $S$  is the interface area,  $\cos \Theta$  is the curvature of the gas–liquid interface, and  $P$  is the porosity. Values  $\Delta p$  as high as some megapascals are measured [23] (see Fig. 10).

In Section 2.1.4 we anticipated the different methods reported in the literature about the optimization of the drying procedures. Here we report the two worthy of mention:

- pentane drying;
- supercritical drying.

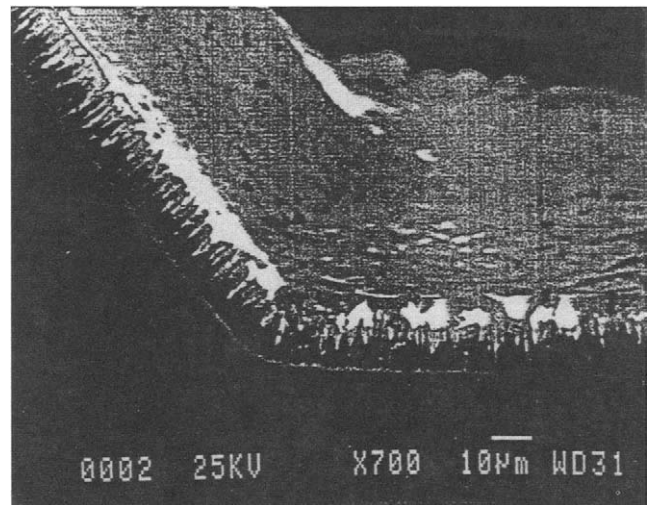


Fig. 9. Cross-sectional SEM image of a typical cracking pattern. Reprinted with permission after Ref. [16].

Pentane drying is the easiest to implement. Pentane has a very low surface tension (i.e., low  $\gamma$  values in Eq. (6)) and shows no chemical interaction with PS (unlike ethanol). Using pentane as rinser, it is possible to reduce strongly the capillary tension; but, because water and pentane are nonmiscible liquids, ethanol or methanol has to be used as an intermediate liquid. Using this drying technique, PS layers with porosity values up to 90% and thickness up to 5  $\mu\text{m}$  exhibit no cracking pattern after drying.

Supercritical drying [20] is based on the exploitation of the fact that when the pressure is raised the interface between the liquid and the gas phase becomes unstable, and when the pressure is larger than the critical pressure the gas–liquid interface disappears and a mixture of the two phases appears (supercritical fluid). This is the most efficient drying method. In such a technique, the HF solution is replaced by a suitable “liquid,” usually carbon dioxide, under high pressure [20]. The phase is then moved above the critical point ( $31^\circ\text{C}$ ) by raising the pressure and temperature, as schematically shown in Figure 11 path a–b, b–c [16]. Then the gas is removed by the supercritical liquid (Fig. 11 path c–d). This drying procedure allows production of layers with very high thickness and porosity values (up to 95%), improving the optical flatness and the homogeneity as well [24].

However, supercritical drying is expensive and complicated to implement so other drying methods are normally employed.

## 2.2. Structure of Porous Silicon

PS presents itself as quite uniform on a long length scale; on a microscopic scale, its structure is formed by silicon

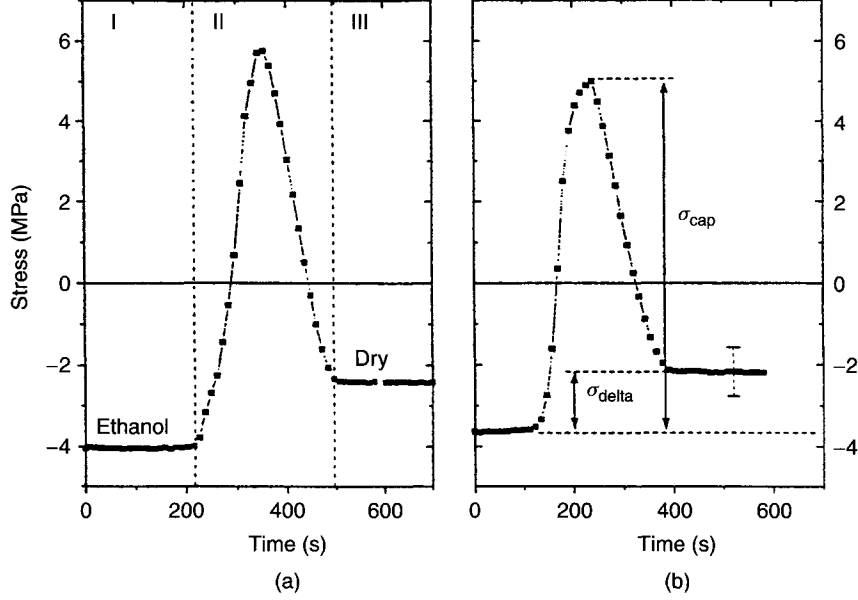


Fig. 10. Stress–time evolution during the drying process of PS: (a) and (b) refer respectively to two different cycles. Reprinted with permission after Ref. [23].

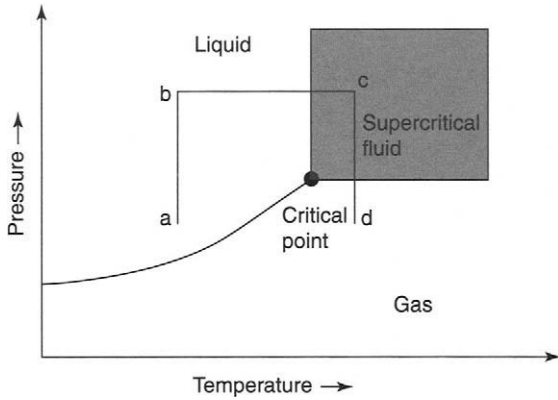


Fig. 11. Schematic phase diagram showing pressure–temperature paths used in supercritical drying. Reprinted with permission after Ref. [16].

nanocrystals or silicon filaments coated with an amorphous matrix. An ideal representation of a porous silicon layer is shown in Figure 12 [25]. The existence of both the crystalline and the amorphous parts is confirmed by various techniques such as X-ray diffraction [26], Raman spectroscopy [27], extended X-rays absorption fine structure (EXAFS) [28], and electron microscopy [29]. The coating matrix has been shown to be disordered [30, 31] and time dependent [32]. Moreover, the coating matrix can be changed by poststretching treatments.

### 2.2.1. Internal Surface

The large quantity of internal voids inside PS causes the presence of a very large inner surface (on the order of

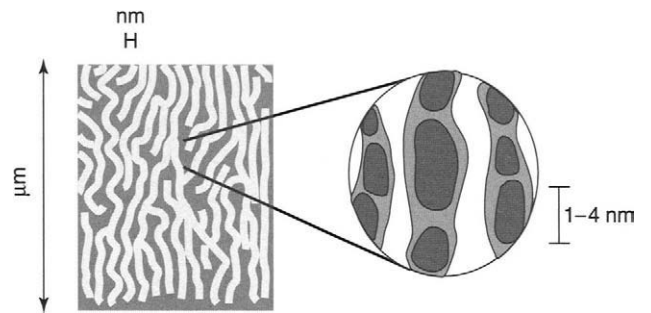


Fig. 12. Ideal representation of a porous silicon layer: (left) the etched array of voids in silicon; (right) an enlarged area of the PS layer, where the silicon nanocrystals are embedded in an amorphous matrix. Adapted from [25].

$500 \text{ m}^2 \text{ cm}^{-3}$ ) [32]. The large number of surface defects is mostly due to dangling bonds and acts as an efficient luminescence quencher [33, 34]. It follows that PS is a material that results from a “forest” of pores extending from the outer surface in depth along the direction determined by the current flow. The region among the pores is formed by interconnected Si nanocrystals that are arranged in accordance with highly constrained and filamentary structures.

### 2.2.2. Pore and Size Shape

A direct image of PS layers is given by transmission electron microscopy (TEM) [35]. Using this technique, the main properties studied are the morphology of the pore network and the crystallite dimensions [11, 20, 21, 29, 36–58].

During the 1980s, Beale et al. [11] studied PS layers formed using a wide range of anodization conditions and starting from different substrates. These studies were continued in the 1990s, focusing on luminescent and (heavily) oxidized materials [1]. It is important to note that the preparation techniques used for TEM samples have an impact on the final results. Chemical thinning transforms the porous material into a microcrystalline one, whereas ion milling originates an amorphization of the material, even if morphological information is still obtainable. Cleavage or scraping of fragments from the substrate appears to be a less destructive preparation procedure, and it is particularly suitable for highly porous materials.

The differences in morphology are evident for *p*-type and *n*-type material as shown in Figure 13 [8]. For *p*-type doped Si, both pore size and interpore spacing are very small, typically between 1 and 5 nm, and the pore network looks very homogeneous and interconnected. With increasing the concentration, the pore sizes and the interpore spacing increase, whereas the specific surface area decreases. The result is that the structure becomes anisotropic, with long voids running perpendicular to

the surface; this fact is less evident for *p*<sup>−</sup> than for *p*<sup>+</sup> material. In the latter case the anisotropy of the microstructure is very evident, as shown in Figure 13c for highly doped material. For *n*-type doped Si the situation is more complicated. Generally, pores in *n*-type doped Si are much larger than in *p*-type doped Si, and pore size and interpore spacing decrease, increasing the dopant concentrations. Lightly doped *n*-type substrates anodized in the dark lead to low porosity (1–10%), with pores in the micrometer range. Under illumination instead, higher values of porosity can be achieved, and mesopores are formed together with macropores. The final structure depends strongly on the anodization conditions. Although highly *n*- and *p*-type doped Si show similar structures (compare Fig. 13c and d), in *n*-type doped Si the pores tend to form randomly directed filaments and to “pipe,” forming large straight channels approaching the electropolishing regime (see Fig. 13b). Both the filaments and the channels propagate only in the  $\langle 1\ 0\ 0 \rangle$  directions, probably because the  $\langle 1\ 0\ 0 \rangle$  planes present the most sterically favored geometry for the chemical etch [8]. TEM specimens with porosities as high as

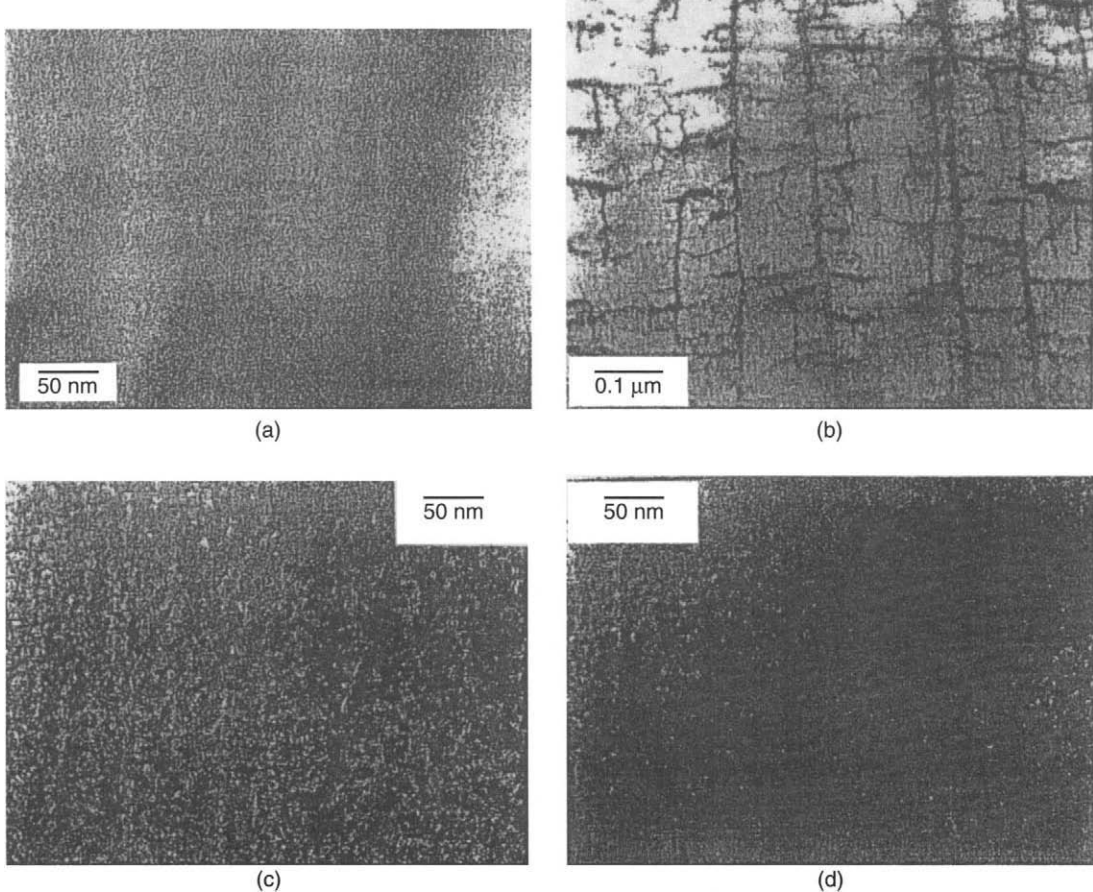


Fig. 13. Cross-sectional TEM images showing the basic differences in morphology among different types of samples: (a) *p*-type silicon; (b) *n*-type silicon; (c) *p*<sup>+</sup>-type silicon; (d) *n*<sup>+</sup>-type silicon. Reprinted with permission after Ref. [8].

80–85% have been prepared by direct cleavage [1, 29] or by scraping [51]. The TEM images [1] present narrow undulating Si columns with diameters less than 3 nm; nevertheless, the crystalline nature of the Si nanostructures is well assessed.

Transmission electron diffraction (TED) studies confirm these results. The TED patterns confirm both the crystalline character of PS and the difference in structure between the *p*-type and the *n*-type layers and the dependence on the level of doping and porosity. Besides, in the case of luminescent materials, the TED studies [29, 50] demonstrate the presence of silicon nanocrystallites. This also has been found for highly luminescent, 95% porosity supercritically dried *p*<sup>+</sup> material, where the TED pattern shows that the “concentration of randomly aligned crystallites has been dramatically reduced in contrast to silicon layer dried conventionally” [20].

### 2.2.3. Scanning Tunneling Microscopy, Atomic Force Microscopy

In addition to electron microscopy studies, a variety of scanning probe microscopy investigations can be found in the literature [59–73]. Atomic force microscopy (AFM) studies focus entirely on the nanoscale characterization of porous silicon films; thus, in most studies, AFM is applied together with other optical or morphological characterization techniques [62–69, 74]. AFM can prove the presence of silicon features with diameters of about 10 nm. The presence of 5-nm large topography features in the images of porous silicon has been claimed also [61, 68, 73]. Because of the geometry of tips commonly used, AFM does not allow the imaging of deep pores. It is, in fact, not possible to image nanometer-wide pores to depths that are comparable to their widths. As a result, AFM allows only the imaging of the top end of the pores, which is a disadvantage of this technique compared with electron microscopy.

In the case of scanning tunneling microscopy (STM), observations are limited by the high resistivity of the material. To circumvent this problem, one can use three different methods [72]: a thin film of the material can be prepared; it can then be deposited onto conductive surfaces; or even the surface of PS can be illuminated. This last technique (photoassisted STM) seems to be the most favorable. The PS surface consists of small (~2 nm) pillarlike structures closely interconnected. There are also holes, 3–5 nm in size. Smaller structures can be seen on the walls of some holes. The use of STM in the spectroscopic mode has also revealed the signature of the widening of the band gap resulting from quantum confinement [72, 75]. Moreover, it has been demonstrated that it is also possible to use the tunneling tip to stimulate local photon emission by electron injection [76–78].

### 2.2.4. Crystalline Nature of PS Skeleton

X-ray diffraction is the experimental method normally used to evaluate the degree of crystallinity. The X-ray diffraction setup allows a direct determination of the lattice parameter *a* of the PS layer. The value of *a* can be determined from differential measurements of the diffraction Bragg angle. Determination of the lattice parameter variation with respect to crystalline silicon is quite complicated [79, 80], probably as a consequence of the large pores that are present. *p*<sup>−</sup> samples reveal a greater lattice expansion. Bomchil et al. [42] reported  $\Delta a/a = 4 \times 10^{-3}$  and  $10^{-3}$  for *p*<sup>−</sup> and *p*<sup>+</sup> samples of 56 and 72% porosity, respectively. Barla et al. [81, 82] found a linear growth of the lattice parameter expansion for *p*<sup>+</sup>-PS going from 3 to  $8 \times 10^{-4}$ , increasing the porosity from 30 to 80%. The same behavior has been reported by Bellet and Dolino [83] even if the measured values were larger. The origin of this expansion is related to the hydrogen–silicon bonds at the inner surface of the PS layer. In fact, a correlation has been found between hydrogen desorption and strain during thermal annealing [84–86]. When hydrogen desorption takes place, a sharp contraction in the lattice parameter occurs. On the contrary, the formation of the oxide layer as a result of the aging or thermal or anodic oxidation originates a further increase of  $\Delta a/a$  [54, 85, 87–89]. In the last case a saturation value of the expansion coefficient at a constant value is reached. Whereas X-ray diffraction at wide angle gives important information on the lattice parameter and the stress, small-angle X-ray diffraction (SAXS) elucidates the size and morphology of the sample. With this method the anisotropic character of the *p*<sup>+</sup> microstructure has been reassessed [90]. Moreover, SAXS studies have confirmed that for luminescent PS the morphology is that of an interconnected network of Si quantum wires whose dimensions are on the order of 3–4 nm [46, 91].

### 2.2.5. N/SEXAFS and EXAFS [XEOL, TEY, PLY]

EXAFS is essentially a bulk technique [92]. However, techniques more appropriate to the study of surfaces have been developed, such as surface-EXAFS (SEXAFS) [93], which probes individual sites, and reflected EXFAS (REFLEXAFS), which uses the possibility of varying the angle of incidence of the X-rays. Of particular importance, in the case of samples that show photoluminescence (PL), is X-ray excitation of optical luminescence (XEOL), also called photoluminescence yield (PLY): a technique that combines an EXAFS measurement with the excitation of the PL [94].

In the case of porous silicon the EXAFS technique has been applied in several detection modes: transmission [95], total electron yield (TEY) [96–102], and PL yield (XEOL or PLY) [103–107]. In particular, TEY measurements have

been used as a direct measurement of the quantum confinement effect on the nanostructure of PS. Moreover, TEY and PLY, recorded at the same time for both porous silicon and siloxene [103], have demonstrated that the origin of PL in PS is different from that of siloxene. It is worthwhile to note that whereas TEY measures secondary electrons escaping from the first few hundreds of angstroms beneath the surface, PLY (XEOL) measures the emission of visible radiation.

Very recently a careful study on the sensitivity of the XEOL to the local structure of the luminescent Si sites has been performed by Dalba and coworkers [106–108]. X-ray absorption near edge structure (XANES) measurements were recorded in TEY and PLY (XEOL) mode at the Si K-edge of porous Si before and after washing it with HF to remove oxygen. EXAFS spectra were recorded in TEY and PLY (XEOL) modes of two different samples obtained from a  $3 \Omega \text{ cm}$  resistivity c-Si wafer with current densities of 60 and  $10 \text{ mA cm}^{-2}$ . From these spectra the following conclusions can be reached [106, 107]: the PL yield induced by X-rays in PS strongly depends on the sample preparation parameters (TEY and PLY XANES give different information; TEY-XANES is sensitive to both silicon-oxygen and silicon-silicon bonds, whereas PLY-XANES originates only from Si–Si bonds; finally, a well-defined crystalline order is clearly present in PS). Concerning the EXAFS results, the TEY data confirm the presence of crystalline structures on a scale of a few nanometers; however, whereas TEY-EXAFS gives average structural information on all Si sites, luminescent and nonluminescent, PLY-EXAFS selects the light-emitting Si sites.

The influence of the PS preparation parameters also is pointed out from the different conclusions about the structural nature of PS (dots or wires?) reached in two EXAFS studies by Schuppler et al. [96] and Zhang and Bayliss [101]. The first group, starting from the fits to their EXAFS data, rule out nanowires as the origin of PL for PS and suggest confined nanodots of particularly small dimensions on the order of  $\sim 0.7\text{--}2.5 \text{ nm}$ ; instead Zhang and Bayliss, studying freshly etched PS emitting in the red, yellow, and orange (PL peaks at 690, 580, and 520 nm, respectively), conclude that the structure of PS is formed by a network of wires, with average diameters of 2.2, 1.9, and 1.3 nm. These dimensions agree with the results from XAFS studies [95], TEM, and X-ray measurements. The difference in the two experiments can be traced to the very different resistance of the Si wafers used for PS preparation ( $>50 \Omega \text{ cm}$  for the Schuppler samples,  $3 \Omega \text{ cm}$  in the Zhang and Bayliss case).

### 2.2.6. Thermal Effects

Thermal conductivity is an important physical parameter in PS. Because of its porous structure, PS shows a low

thermal conductivity and microporous Si can be considered as a good thermal insulator. For electroluminescent devices based on PS it can be a serious limitation; this is because the quantum efficiency is still low and a sensible amount of heat has to be dissipated in the porous layer. On the other hand, this property can be used to form thermally isolated layers on Si.

Recent measurements of thermal properties [109] are strongly in disagreement, probably because of the different morphologies of the investigated samples (see Fig. 14 [110]).

The conductivity can be calculated by the analysis of thermal waves traveling through the sample. For PS formed on lightly *p*-type doped Si, the thermal conductivity is very low, even lower than the value for  $\text{SiO}_2$  ( $\simeq 1.4 \text{ W m}^{-1} \text{ K}^{-1}$ ). This is caused both by the granular structure that does not transport heat easily and by the presence of the pores that prevent heat

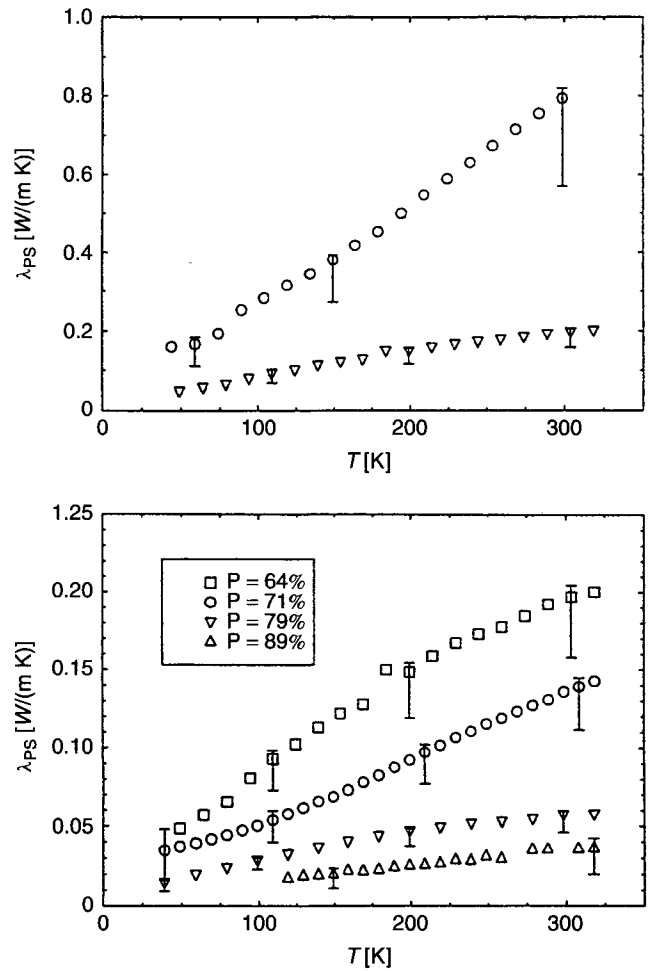


Fig. 14. (top) Thermal conductivity  $\lambda_{\text{PS}}$  for PS layers of thickness of about  $31 \mu\text{m}$  and for different porosities. (bottom) Thermal conductivity  $\lambda_{\text{PS}}$  for PS layers with different substrate:  $p^+$  (circles) and  $p^-$  (triangles) type doped silicon with PS porosity equal to 64%. Reprinted with permission after Ref. [110].

transfer among crystallites. When the material is partially oxidized, the thermal conductivity increases because oxygen is incorporated in the film; therefore, the porosity decreases and the transport increases.

PS formed on  $p^+$ -type doped Si shows a higher thermal conductivity, about one-half the bulk value ( $150 \text{ W m}^{-1} \text{ K}^{-1}$ ). In this case, PS is known to be mesoporous. It can be considered a sponge of Si with pores about 10 nm wide, so that continuous pathways of solid Si are present. The thermal conductivity for PS formed on  $p^+$ -type doped Si can be evaluated from the thermal conductivity of bulk Si through the porosity, whereas for the PS formed on lightly doped Si the data are critically dependent on the preparation conditions.

### 2.2.7. Elastic Effects

The elastic properties of PS, which are drastically different from those of bulk Si, are responsible for the peculiar characteristics of PS layers: its fragility or mechanical instability. In a solid material such as PS, the elastic modulus has to be considered at two different levels. At the crystallite level, the elastic modulus is determined by the stiffness of the atomic bonds, which does not differ from that of bulk Si. At the macroscopic level, Young's modulus is related to the porous structure of the solid. This macroscopic modulus is expected to be smaller than that of the bulk material and to decrease with increasing porosity. Young's modulus of PS can be determined by four different techniques: Brillouin scattering, X-ray diffraction, acoustic wave propagation, and nanoindentation [111]. The values obtained by the different methods do not differ very much, as reported in Figure 15.

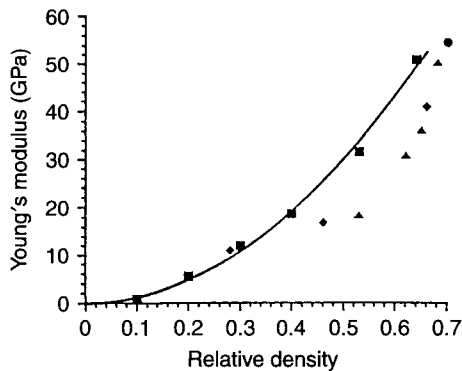


Fig. 15. Young's modulus values of  $p^+$ -type PS samples reported as a function of the relative density: X-ray measurements (filled diamond), acoustic wave propagation (filled triangle), nanoindentation technique (filled square), and Brillouin spectroscopy (filled circle). Reprinted with permission after Ref. [111].

PS formed on  $p^+$ -type doped Si has open pores, and for such open-cell structures Young's modulus  $Y_p$  is expected to vary according to [112]

$$Y_p = CY_B \rho^2 \quad (7)$$

where  $Y_p$  is Young's modulus of the sample,  $Y_B$  is the elastic modulus for the bulk Si,  $\rho$  is the relative density and  $C$  is a phenomenological constant on the order of unity. Figure 15 shows that the experimental determination [111, 110] is in good agreement with the parabolic function (nanoindentation data), giving  $CY_B = 120 \text{ GPa}$ , not too different from Young's modulus of bulk Si (162 GPa).

For PS formed on  $p$ -type doped Si, the very complicated pore morphology does not fulfill the model assumptions that led to Eq. (7). However, PS formed on  $p$ -type doped Si material appears to be less stiff than PS formed on  $p^+$ -type doped Si with the same porosity level.

Using a high-resolution X-ray double diffractometer it has been found [113] that the diffraction peak of a PS layer is almost as narrow as the peak of the Si substrate, but slightly shifted to a smaller diffraction angle [114], as observed in Figure 16. The angular distance between the two peaks is directly related to the lattice mismatch parameter. The related strain is strongly dependent on the porosity (Fig. 17), on the doping, and on the type of substrate and oxidation [115]. The strain increases with oxidation, which corresponds to the growth of a thin oxide layer on the internal surface of PS. For this reason the strain in PS increases with time [116], with heating in air [117], or with anodic oxidation [118]. Whereas heating in air pro-

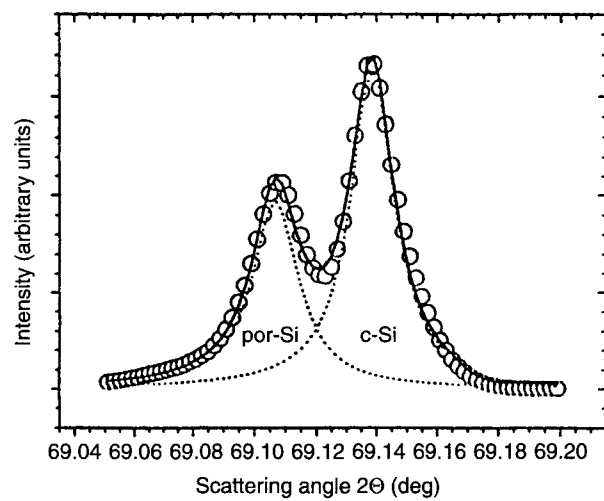


Fig. 16. Intensity distribution near the (0 0 4) Bragg reflection of a  $p^+$ -type sample: open circles represent the experimental data, which consist of two different contributions; the substrate peak (c-Si) and the expanded lattice of PS layer (por-Si). The solid line is the sum of the two contributions (dashed line). Reprinted with permission after Ref. [114].

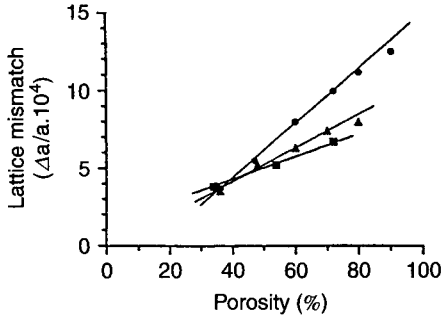


Fig. 17. The variation of lattice mismatch vs. porosity of  $p^+$ -type PS layer is reported in three different investigations. Reprinted with permission after Ref. [115].

duces a large oxidation strain, annealing performed in an inert environment or under vacuum produces a contraction due to H desorption [119].

The origin of strain is related to the large internal surface of PS. Probably the strain is due to the presence of  $\text{SiH}_x$  bonds on the crystallite surface, and the contraction under vacuum annealing during desorption of hydrogen supports this hypothesis. Another explanation could be that the oxide layer expands. However, there is little oxide in freshly etched PS, and it is hard to attribute the initial strain to oxide formation, although it is likely that the increase of strain with time is due to the growth of an oxide layer.

Hardness is defined as the resistance of a solid to plastic deformations [120] and can be measured with different techniques. The most widely used techniques are static indentation tests that give the hardness as the ratio of the applied force versus the area of indentation.

Figure 18 shows the variations of the hardness versus the porosity for  $p^+$ - and  $p^-$ -type PS [120]. The hardness of the samples with different substrates is comparable, which means that the morphology is not so important. For both types of PS the hardness decreases with increasing porosity. At low porosities the decrease in the hardness can be expressed as

$$H = H_0 \times (1 - P)^m \quad (8)$$

where  $m = 2/3$  and  $H_0$  is the hardness of bulk Si (solid line in Fig. 18). At high porosities the hardness drops at values lower than the previous ones, indicating changes in the structure of the samples.

#### 2.2.8. Raman Spectroscopy

Among the other optical investigation methods, Raman spectroscopy, and especially micro-Raman spectroscopy, can give indirect information on the microstructure of PS. Although in bulk Si the interaction of the optical phonons

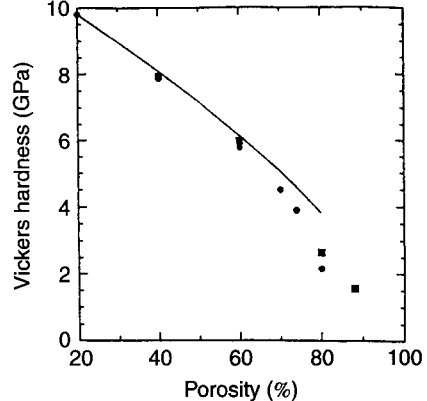


Fig. 18. Hardness vs. the porosity for PS films. The  $p^+$ -type samples are represented by filled circles, and  $p^-$ -type samples by filled squares. The applied load corresponds to  $0.49 N$ . The solid line represents the  $H_0(1 - P)^{2/3}$  term, where  $H_0$  is the hardness of crystalline silicon (11.5 GPa). Reprinted with permission after Ref. [120].

with incident photons is limited to the center of the Brillouin zone, the presence of nanocrystals in PS relaxes the  $\mathbf{k}$ -selection rule, with a broadening of the associated Raman peak [121].

The Raman spectra are analyzed in terms of specific contributions from amorphous and nanocrystalline Si. A Gaussian line centered at  $470 \text{ cm}^{-1}$  with a width of  $55 \text{ cm}^{-1}$  is used as a representative of the amorphous contribution. The Si nanocrystal contribution is described by using a phenomenological model based on the spatial confinement of phonons [122, 123]:

$$I(\omega) = \int_0^\infty I_L(\omega)P(L)dL. \quad (9)$$

$I(\omega)$  is the Raman spectrum,  $I_L(\omega)$  is the first-order Raman scattering from phonons confined within nanocrystals with size  $L$ , as calculated by Campbell and Fauchet [123], and  $P(L)$  is the crystallite size distribution, i.e., a Gaussian distribution with mean  $L_0$  and dispersion  $\sigma$ . The results of a fitting procedure are reported in [121]. The fitting parameters are  $L_0 = 6.5$  (4.5) nm and  $\sigma = 2.2$  (1.6) nm, and the relative weight of the amorphous to the crystalline part is  $\approx 10\%$  for the top (bottom) spectrum.

Sizes larger than those measured by EXAFS are reported by Raman analysis. A partial answer to this discrepancy is given by EXAFS measured in XEOL configurations in which the energy-resolved EXAFS signal is measured on the luminescence band [124]. The sizes of the Si nanocrystals that emit in the visible range are significantly smaller than the average sizes of Si nanocrystals in PS as measured by standard EXAFS or Raman scattering.

### 2.2.9. BET Measurements

Accurate determination of pore size distribution in mesoporous Si is usually performed by analysis of the adsorption isotherms of gases at low temperature [Brunauer-Emmett-Teller (BET) technique] [125]. The physical adsorption by a porous surface is increased relative to a smooth one because of capillary condensation into pores. This increase in the adsorption starts when the gas pressure is high enough to fill the smallest pores.

Figure 19 shows a typical adsorption isotherm for a heavily *p*-type doped PS layer [126]. The first part of the curve, at low relative pressures, corresponds to the adsorption from the porous surface and allows determination of the total surface area [127]. The sharp increase at higher relative pressures is related to capillary condensation of the gas into the pores. The final plateau indicates the complete filling of the pores, and the amount of liquid corresponding to the volume of the gas adsorbed allows the determination of porosity. The isotherm shows an hysteresis loop, because on lowering the pressure, some evaporation of the liquid from the pores occurs. There are different methods to obtain the pore size distribution from adsorption isotherms, but the most commonly employed is the Barrett-Joyner-Halenda (BJH) method [128], which is normally used for mesoporous Si: the shape of a typical adsorption isotherm is quite different from Figure 19,

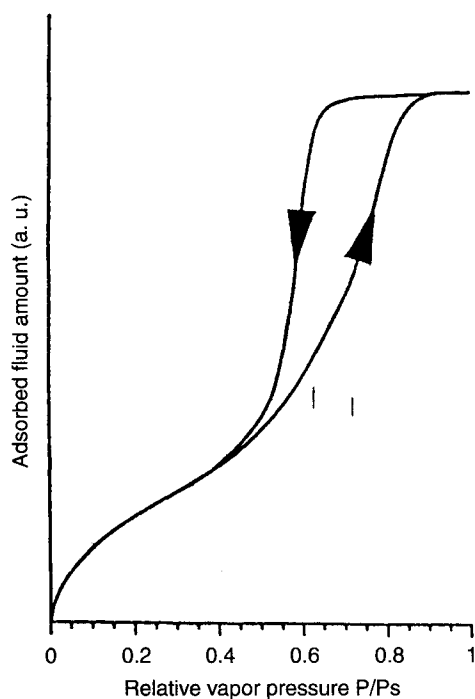


Fig. 19. Schematic representation of a nitrogen adsorption isotherm at 77 K for a PS layer formed on heavily doped *p*-type substrate. Reprinted with permission after Ref. [126].

because the rapid intake of gas happens at low relative pressures, with no hysteresis loop. Extracting accurate pore distribution from this type of adsorption isotherm is difficult and becomes even more complicated when micro-pores and mesopores coexist in the same sample.

## 2.3. Chemical Properties of Porous Silicon

### 2.3.1. Chemical Composition of Porous Silicon

As mentioned before, the internal surface of PS is very large. Values as high as  $1000 \text{ m}^2 \text{ cm}^{-3}$  can be measured [129] (see Fig. 20). Such a large surface contains an enormous quantity of impurities, coming from the electrolyte used for electrochemical etching, from the ambient air, and from the wafer itself. So it is important to know the chemical composition of PS because the optical and electrical properties depend on the impurity content and the surface passivation.

The original impurity that is always found in PS layers is hydrogen. Infrared (IR) absorption experiments have shown the presence of  $\text{Si}-\text{H}_x$  groups ( $x = 1, 2, 3$ ) on the internal PS surface during the etching process [30, 31, 130].

In Figure 21 a typical IR spectrum of a fresh PS sample is reported [131]. The IR frequencies commonly observed in PS and their attributions are reported in Table II. After the formation and the drying procedure, the  $\text{Si}-\text{H}_x$  groups are still present on the inner surface for weeks and even for months, as has been demonstrated using IR absorption and nuclear magnetic resonance. H desorption occurs during the annealing, and it has been shown [132] that hydrogen desorbs from  $\text{SiH}_3$  groups between 300 and 400 °C. Its desorption from  $\text{SiH}_2$  instead occurs at 400 °C and from  $\text{SiH}$  at around 500 °C.

The atomic ratio H/Si in PS has been determined using secondary ion mass spectrometry (SIMS) [133] and elastic recoil detection analysis (ERDA), and in freshly anodized

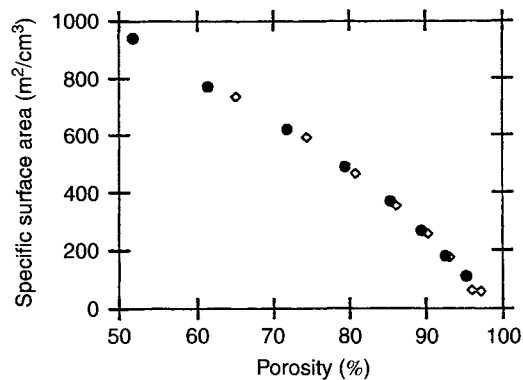


Fig. 20. Specific surface area as a function of the PS porosity. Data of PS with porosity of 51% (dot) and 65% (square). The layer thickness is equal to 1  $\mu\text{m}$ . Reprinted with permission after Ref. [129].

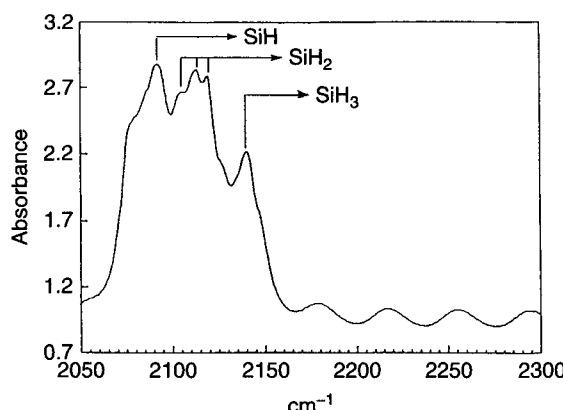


Fig. 21. IR absorption spectrum at the temperature of 8 K for a free-standing  $p^+$ -type PS in the Si-H stretch mode. The thickness is 89  $\mu\text{m}$  and the porosity 50%. The lines that correspond to O<sub>x</sub>—Si—H groups (around 2200–2250  $\text{cm}^{-1}$ ) are absent; note the presence of Si—O—Si groups around 1065  $\text{cm}^{-1}$ . The visible oscillations are interference fringes that originate at the PS—air interfaces. Adapted from [131].

samples it is as high as 0.1–0.6, depending on the porosity and surface area of the samples. This result means that the surface of freshly etched PS is almost totally covered by SiH<sub>x</sub> groups.

The second original impurity found in PS is fluorine. This was demonstrated using many experimental techniques (SIMS, ERDA, ENDOR). The form in which fluorine is present in PS is still under question. Desorption experiments [132] demonstrated that SiF<sub>3</sub> groups desorb at the same temperature as SiH<sub>3</sub>, indicating that SiF<sub>3</sub> groups are present on the pore walls. The presence of SiF and SiF<sub>2</sub> groups have been shown by IR spectroscopy [134]. The concentration seems to be higher in samples etched in aqueous HF solutions than in ethanoic HF solutions. The fluorine content decreases

with time, and it has been proposed that SiF bonds are progressively replaced by Si—OH bonds through hydrolysis reaction with water vapor in air. On the other hand, only HF and SiF<sub>6</sub><sup>2-</sup> were found using <sup>19</sup>F NMR [135]. According to these results, fluorine is thought to come only from residual electrolyte in the pores.

Other impurities are usually incorporated after the anodization process. Several techniques [30, 31, 133, 136, 137] have detected the presence of carbon. The carbon content can be as high as 10% in the aged samples. It can be excluded that the source of carbon is ethanol, because carbon is present in similar amounts also in samples anodized in water–HF solutions [136]. The source of carbon is the atmosphere, but the adsorbed molecules are not CO or CO<sub>2</sub>, because carbon and oxygen contents are not correlated. The carbon comes from hydrocarbon molecules present in the ambient air and often also in the residual gas in analysis vacuum chambers used for SIMS, IR, XPS, etc.

The most important nonoriginal impurity is oxygen and it is normally adsorbed in a few minutes after drying in ambient air. The amount of oxygen can be as high as 1% after 15 minutes of air exposure, as confirmed by electron paramagnetic resonance (EPR) [131], and increases to very high percentage values with aging. IR spectra performed a few hours after anodization of a PS layer have also shown the presence of Si—O—Si groups (mode at 1065  $\text{cm}^{-1}$  in the inset of Fig. 21). The IR absorption due to the O<sub>x</sub>—Si—H groups at 2200–2500  $\text{cm}^{-1}$  is not present in this sample; it means that the oxidation is only partial. A few days after anodization further oxidation takes place, through the formation both of Si—O—Si groups and of O—Si—H and O<sub>3</sub>—Si—H groups. The existence of such groups does not modify the hydrogen passivation, and the possible presence of water simply accelerates the oxidation process.

Table II Wavenumber Positions and Attributions of the Absorption Peaks Observed in Several PS Samples

Peak position ( $\text{cm}^{-1}$ )	Attribution	Peak position ( $\text{cm}^{-1}$ )	Attribution
3610	OH stretching in SiOH	1463	CH <sub>3</sub> asymmetrical deformation
3452	OH stretching in H <sub>2</sub> O	1230	SiCH <sub>3</sub> bending
2958	CH stretching in CH <sub>3</sub>	1056–1160	SiO stretching
2927	CH stretching in CH <sub>2</sub>		in O—SiO and C—SiO
2856	CH stretching in CH	979	SiH bending in Si <sub>2</sub> —H—SiH
2248	SiH stretching in O <sub>3</sub> —SiH	948	SiH bending in Si <sub>2</sub> —H—SiH
2197	SiH stretching in SiO <sub>2</sub> —SiH	906	SiH <sub>2</sub> scissor
2136	SiH stretching in Si <sub>2</sub> O—SiH	856	SiH <sub>2</sub> wagging
2116	SiH stretching in Si <sub>2</sub> H—SiH	827	SiO bending in O—Si—O
2087	SiH stretching in Si <sub>3</sub> —SiH	661	SiH wagging
1720	CO	624	SiH bending in Si <sub>3</sub> SiH

Source: Adapted from [30, 31].

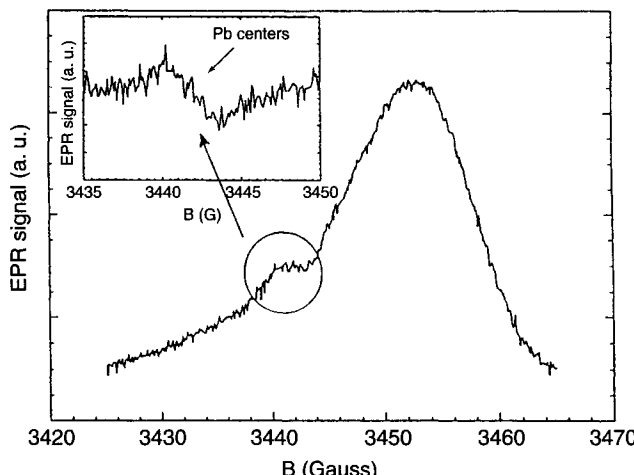


Fig. 22. Room-temperature EPR spectrum of a (1 0 0) 11- $\mu\text{m}$ -thick  $n^+$ -type PS sample. The magnetic field is in the (1 1 0) plane parallel to the [0 0 1] orientation: (inset) EPR spectrum of the Pb centers. The large signal due to free carriers was subtracted. Adapted from [131].

EPR measurements also emphasize the relevance of the Si-SiO<sub>x</sub> interface in PS. In Figure 22 the EPR spectrum of a fresh  $n^+$ -PS layer is reported. This shows two absorption lines [131]. The broad one is due to conduction electron spin resonance (CERS). EPR studies [138] on  $n^+$  freestanding PS layers have shown that the CERS signal is present only in the substrate, demonstrating that free carriers are absent in PS. The signal resulting from the dangling bonds appears clearly after subtraction of the signal corresponding to the free carriers. As shown by Pivac et al. [139], the dangling bonds are the most important paramagnetic defect at the Si-SiO<sub>2</sub> interface (Pb centers), and have a ·Si≡Si<sub>3</sub> structure. The other relevant paramagnetic center is the ·Si≡SO<sub>3</sub> defects ( $E'$  center). This center is formed especially in hydrogen-depleted oxide layers, as shown in the EPR spectra of Figure 23, recorded in different PS layers irradiated with  $\gamma$ -rays [139].

### 2.3.2. Degradation under Analysis

It is important to note that, for a material as fragile and chemically reactive as PS, chemical alteration under analysis is a critical parameter. Potential problems with sample degradation arise in electron microscopy and PL spectroscopy, but they are also present in a wide range of other techniques that require optical or electrical excitation or that make use of ion [29], electron [137], and X-ray beams [140].

The degradation effects of these techniques are summarized in Table III; quite often the structure of the sample under investigation is annealed or damaged to a point that the experimental data collected do not reflect the original nature and composition of the starting material. This aspect is especially important in the case of aged samples.

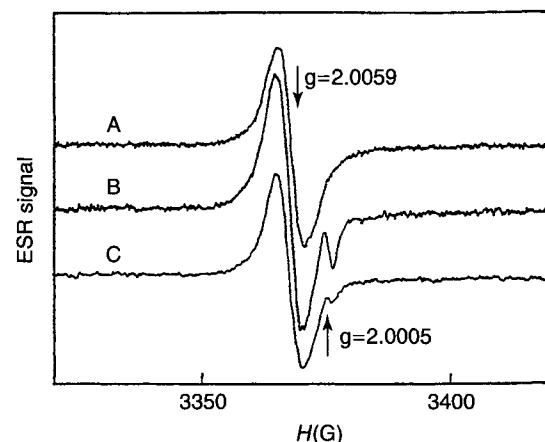


Fig. 23. EPR samples irradiated by 10-Mrad  $\gamma$ -rays from  $^{60}\text{Co}$  source (A), annealed at 450°C for 15 min in  $\text{N}_2$  before irradiation (B), exposed to molecular hydrogen at room temperature for 30 min after annealing and irradiation (C). Reprinted with permission after Ref. [139].

Table III Degradation Mechanism of PS Under Different Analysis Techniques

Excitation	Associated techniques	Degradation observed
Blue-UV photons	PL in air Micro-Raman	Photooxidation Thermal annealing
X-rays	XPS XEOL	H-desorption Amorphization
Electron beams	Auger CL, TEM	Hydrocarbon build-up Sintering and SiC formation
Ion beams	Ion milling for TEM Ion beam analysis	Amorphization H-desorption C and O adsorption

Source: Adapted from [145].

In this regard, effects resulting from analysis degradation can be interpreted as aging effects and, in some cases, can explain why the composition values reported by different groups in nominally similar layers are remarkably different. It has been demonstrated [141], for instance, that PS can efficiently gather water vapor and hydrocarbon in vacuum, especially under ion beam irradiation. In this way the concentration of O, C, and H can be altered during ion beam analysis itself, limiting the reliability of this technique, as conventionally applied.

### 2.3.3. Aging Problems

As stated previously, PS slowly reacts with the ambient air and consequently its chemical composition and

its properties evolve continuously with storage time. The ambient conditions and the time elapsed determine the oxidation level. When transferred and stored under high vacuum (HV) and in the dark, PS layers present a very low content of oxygen, undetectable by techniques such as XPS, Auger, and Fourier transform IR (FTIR). On the other hand, when no particular care is taken, oxygen can reach very high levels. Both optical and gravimetric techniques permit estimation of the oxide fraction; oxide content up to 50% has been observed [13].

A typical Auger spectrum of a freshly etched PS is reported in Figure 24 [142]. In the range observed, the Si-, Cl-, and C-related transitions are observed. Instead the peak related to O, which should lie around 510 eV, is not detected, indicating that the amount of native oxide, if present, is below the detection limit. Moreover, the lineshape of the Si-related transition is characteristic of hydrogenated Si, demonstrating that the Si dangling bonds are passivated by hydrogen and, eventually, C. After a few weeks in ambient atmosphere, the Auger spectrum of the same sample is quite different. The O-related transition is present around 510 eV (not shown) and the Si-related lineshape is characteristic of Si bonded in a  $\text{SiO}_x$  complex (inset of Fig. 24). A small fraction of the hydrogenated Si is still present (high energy peak in the Si-related transition).

### 2.3.4. Intentional Oxidation

A wide range of postanodization treatments of PS have been developed for different purposes. Complete conversion into silica was the first broad application of PS, for dielectric insulation or devices in microelectronics, but many oxidation treatments have been used since then as a means to improve the photostability of luminescent films

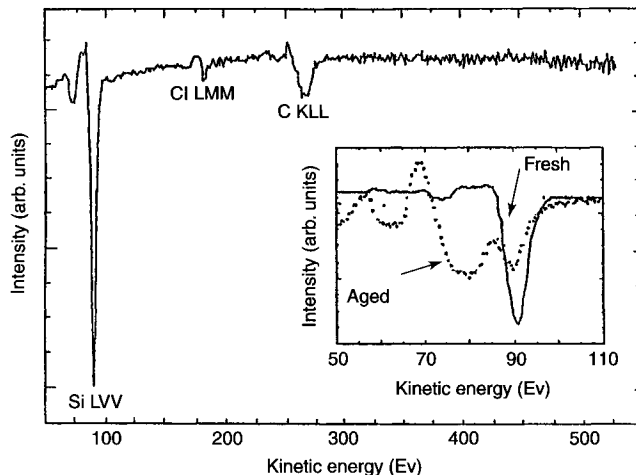


Fig. 24. Auger spectrum of a freshly etched PS sample: (inset) comparison between an aged (dotted line) and a freshly etched (solid line) sample. Reprinted with permission after Ref. [142].

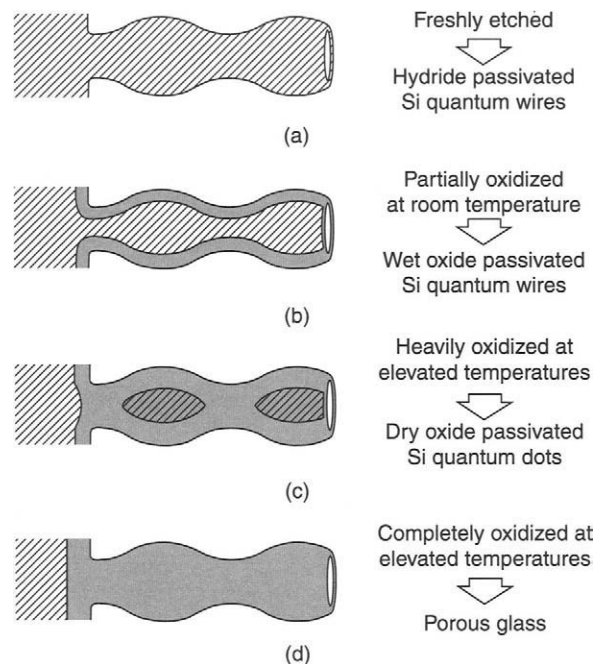


Fig. 25. Idealized schematic steps in the oxidation process of highly porous silicon. Reprinted with permission after Ref. [143].

(see Section 2.3.3). Figure 25 reports an idealized scheme of the oxidation process, starting from a freshly etched PS to a wholly oxidized porous glass [143]. Although in most cases the degree of oxidation has been revealed qualitatively, few data are available regarding the chemical composition of intentionally oxidized samples. In the anodic oxidation process, PS layers are oxidized selectively. Only those PS regions where the current flows are oxidized. Complete oxidation is not achieved, because electrical isolation of parts of the Si skeleton occurs, preventing further current flow [144]. In mesoporous samples of 65% porosity, formed on a  $p^-$ -type doped substrate, about 40% of the Si remains unoxidized at the end of the process, corresponding to about a monolayer of oxide coating. In the case of thermal oxidation, a stabilizing pretreatment at 300 °C, before to the high-temperature oxidation, is necessary to avoid pore coalescence. The content of oxygen at the end of the process varies with the substrate, oxidation temperature, and duration. In mesoporous material, formed on  $n^+$ -type doped substrates and oxidized at 1050 °C, more than 90% of the Si is oxidized within 30 s ([145] and references therein). However, heavily oxidized material is still susceptible to atmospheric “aging” and contamination, simply because the oxide matrix is still porous. Indeed, the water content of oxidized PS depends on the ambient humidity. Some other kinds of chemical oxidation with hydrogen peroxide, nitric acid [146], or boiling water [147] also have been reported.

### 2.3.5. Surface Chemistry

There are many and different capping layers that can be deposited onto the outer surface of PS. The deposition and the growth of metal and metal silicide layers is important for producing structures such as barrier layers, buried contacts, and Schottky devices. Thermally evaporated Al capping layers deposited onto PS are effective for the reduction of aging and for reducing C and O adsorption. Films sputtered with Al are reported to be more effective than thermally evaporated films in minimizing the ambient aging effects. The main drawback is that layers with sufficient thickness to prevent aging would also prevent transmission of visible light in PL or electroluminescence processes. So transparent capping layers such as indium thin oxide (ITO) or Si oxide are more suited for applications involving visible light.  $\text{SiO}_2$  layers can be deposited onto microporous Si by plasma-enhanced chemical vapor deposition (PECVD), but it has been shown that they are effective in preventing aging only for medium porosity PS [148]. PECVD is also used to deposit thin layers of  $\text{Si}_3\text{N}_4$  and  $\text{SiC}$  on photoluminescent PS, improving in this way its luminescence stability [149]. Other types of capping layers are deposited by molecular beam epitaxy (MBE), including Si, SiGe,  $\text{CoSi}_2$ , and GaAs. In most of these experiments it is clear that the quality of the deposited layer depends both on the porosity and on the doping of the underlying PS, and the best results are achieved with highly doped substrates with porosity up to 50%.

A possible alternative to metal and dielectric capping is offered by organic derivatization. The reason is that this process is expected to stop at the first monolayer and allows possible applications for sensors. In any case, the tendency of Si is to irreversibly form Si–O bonds, making oxidation a strong competitive reaction. To substitute H on the inner PS surface, various chemical groups have been used, including  $-\text{CH}_2\text{CH}_3$  [150],  $-\text{OCH}_3$  [151], triethylsiloxy and 3-thiophene methoxy [152] groups, and many others [153, 154]. However, the organic derivatization partially quenches luminescence [152, 155].

## 2.4. Optical Properties

### 2.4.1. Porous Silicon Band Gap

In bulk crystalline Si the term *band gap* means the energy gap between the maximum of the valence band and the minimum of the conduction band, and its value can be extracted from a simple transmission spectrum. In PS, in contrast to bulk crystalline Si, there exists a wide spread of band gaps, as demonstrated by the large and inhomogeneous broadening of its visible PL band. Experimental measurements allow us to extract an average value, but the comparison is still meaningful, because the intrasample

band gap variation is normally smaller than the intersample variations.

Different techniques can be used to obtain the experimental values of the PS band gap ([156] and references therein). The luminescence technique measures the recombination energy of carriers excited across the gap. The PL maxima are used for comparison, whereas the lineshapes of the luminescence display directly the intrasample variation of the band gap. Other techniques are correlated to the absorption across the gap, including transmission spectroscopy, photothermal deflection spectroscopy, PL excitation spectroscopy (PLE), and photoconductivity. It is worth mentioning that the characteristics of PS diodes can also give estimates of the band gap, but the values are critically sensitive to the validity of the model adopted. Electroluminescence measurements rely on the fact that the wavelength of the electroluminescence peak depends linearly on the applied bias. The difference between the positive and the negative bias that was required to obtain the same peak wavelength gives an estimate of the PS band gap. X-ray methods can also be employed. XAFS measures the energy required to eject electrons from PS, from which the band gap value can be deduced. However, this technique is surface sensitive and leads to a systematic error resulting from charge effects.

The PL peak positions can vary from the near IR, close to the value of the bulk Si gap, to the blue, with a spread of about 2.0 eV. Normally the PL peaks lie about 0.2 eV below the values of the band gap as estimated by other methods.

### 2.4.2. Refractive Index

For any application of a material in optics or optoelectronics it is essential to know its refractive index. A very simple method of evaluating the refractive index for a filmlike material is to measure the interference fringes, resulting from multiple reflections, to obtain the optical thickness (see Fig. 26) [2]. The position of the interference maxima satisfies

$$2nd \left( \frac{1}{\lambda_r} - \frac{1}{\lambda_{r+1}} \right) = 0 \quad (10)$$

where  $n$  is the refractive index,  $d$  is the layer thickness, and  $\lambda_r$  is the wavelength of the  $r$ th reflectance maximum. If the layer thickness is known independently the refractive index is simply the ratio between the optical path  $nd$  and the layer thickness. This method can only be applied if the interference fringes are visible and if the layer is thin. If the material possesses a large dispersion, other methods should be employed. A more complete evaluation requires simulation of experimental spectra. Usually reflectance or transmittance spectra are simulated

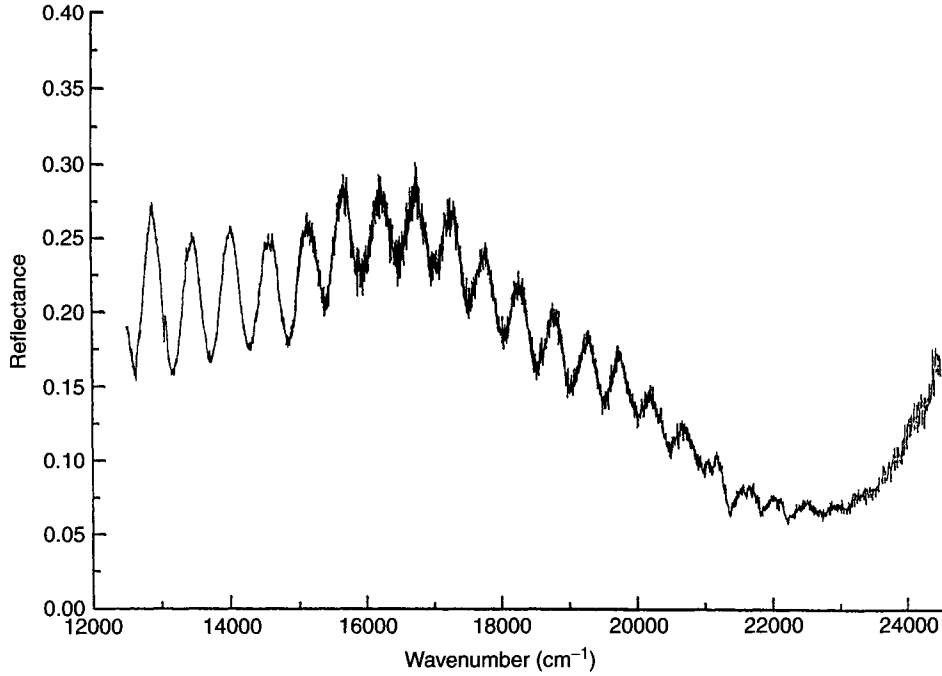


Fig. 26. Normal-incidence reflectance spectrum of a 75% porosity sample 6.8  $\mu\text{m}$  thick. Reprinted with permission after Ref. [2].

using a dielectric function model whose parameters, including the layer thickness, are adjusted to fit the measured data [157]. Since reliable models are available, this method is usually successful and permits the final structure to be designed to obtain the desired dielectric properties. The square root of the dielectric function resulting from the fit is the refractive index of the PS layer. The simulation approach requires sharp interfaces, and the sharpness often depends on the type and the quality of the substrate. Usually the required sharpness is achieved more easily with *p*-type substrates.

The refractive index of PS is expected to be lower than that of bulk Si and decreases with increasing porosity, because PS is basically a mixture of air and Si. However, the averaging of the dielectric functions of the individual components is not trivial, but depends on the microtopology of the material. The application of different effective medium theory leads to different formulas [158–160]. For example, the widely used Bruggeman [159] formula leads to the symmetric expression

$$f \frac{\varepsilon - \varepsilon_{\text{eff}}}{\varepsilon + 2\varepsilon_{\text{eff}}} + (1 - f) \frac{\varepsilon_M - \varepsilon_{\text{eff}}}{\varepsilon_M + 2\varepsilon_{\text{eff}}} = 0 \quad (11)$$

where  $f$  describes the volumetric fraction,  $\varepsilon$  and  $\varepsilon_M$  are the dielectric functions of Si and the embedding medium (air), and  $\varepsilon_{\text{eff}}$  is the effective dielectric function for PS. However, at least for microporous Si, the pore wall material cannot be considered as bulk Si, and different optical constants should be used.

The experimental refractive index as a function of porosity and current density for two different substrate doping levels is reported in Figure 27 [161]. It is worth noting the following:

- as the current density is increased (i.e., as the porosity is increased), the refractive index of the PS layer tends to that of air, in agreement with the simple arguments given previously;
- for the same porosity the same refractive index is found, which shows that Eq. (11) is a good approximation;

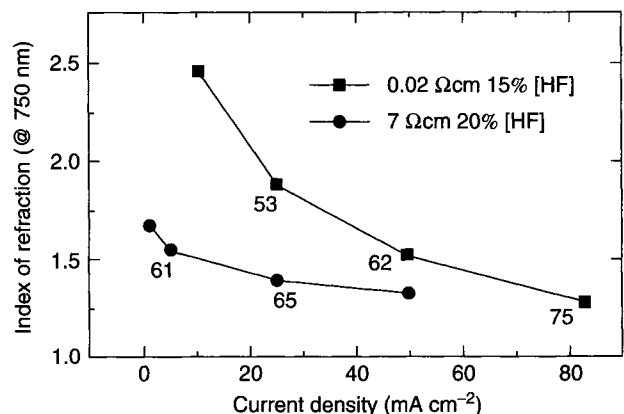


Fig. 27. Refractive index as a function of current density and porosity for two different substrate doping levels. Adapted from [161].

- large variations in the refractive index are possible by varying the current density, that is, the porosity;
- PS formed on heavily doped substrates shows larger refractive index variations than PS formed in lightly doped substrates.

The refractive index is also sensitive to the aging or treatments the PS samples have suffered. In particular, it decreases during oxidation because of the lower refractive index of Si oxide compared with that of Si. Thus, for applications and for device design, it is important to know how the refractive index changes with time or to avoid oxidation.

## 2.5. Luminescence in Porous Silicon

PS-based structures luminesce efficiently in the near IR (0.8 eV), in the whole visible range, and in the near ultraviolet (UV) [162] (Fig. 28). This broad range of emission energies arises from a number of clearly distinct luminescent bands. We can characterize the PS luminescence basically with three different bands:

- the blue band, centered around 2.3–2.6 eV (F band);
- the visible band, centered between 1.4 and 2.2 eV, with a full width at half-maximum (FWHM) of  $\simeq 0.3$  eV (S band);
- the IR band, centered typically at 0.8 eV (IR band).

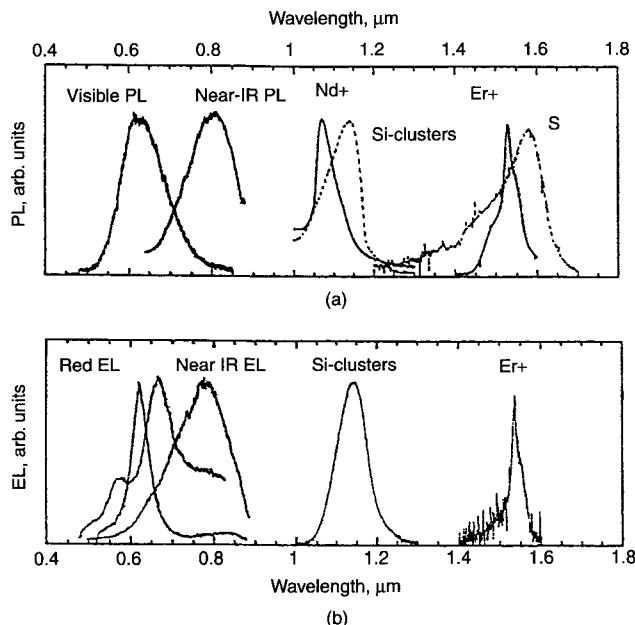


Fig. 28. Room-temperature PL and electroluminescence spectra for various PS structures which have been oxidized or implanted with some selected impurities. Reprinted with permission after Ref. [162].

Table IV PS Luminescence Bands

Spectral range	Peak wavelength	Label	PL	EL
UV	~350 nm	UV band	Yes	No
Blue-green	~470 nm	F band	Yes	No
Blue-red	400–800 nm	S band	Yes	Yes
Near IR	1100–1500 nm	IR band	Yes	No

Source: Adapted from [1].

We follow for the PS luminescence bands the nomenclature listed in Table IV [1].

### 2.5.1. S Band

The properties of the S band have been studied and the S band certainly has the most technological relevance because it can be electrically excited. Its main spectral features are summarized in Table V.

The S band can be tuned from close to the bulk silicon band gap through the whole visible range. In Figure 29 the room-temperature luminescence spectra of PS samples with different porosities are shown [163]. It is worth noting that, whereas the PL efficiency is high under blue or UV excitation, in the range from red to yellow the emission is rather low [163]. The S-band large spectral width is due to inhomogeneous broadening, and its spectral position depends on porosity. It is important to note that not only the spectral position but also the relative intensity of the S-band changes with porosity (Fig. 30) [164]. It was found that the S-band efficiency is not proportional to the inner surface area but that there exists a “threshold” porosity that has to be exceeded to achieve efficient luminescence [1].

Table V Some Spectral Characteristics of the S Band

Property	Typical values	Comments
Peak wavelength	1100–400 nm	At 300 K
PL efficiency	$\geq 5\%$	At 300 K and for external quantum efficiency
FWHM	0.3 eV	At 300 K (8 meV in porous silicon microcavities)
PL decay times	$\simeq 10 \mu s$	Strongly dependent on wavelengths temperature and aging condition
Polarizability ratio	$P \leq 0.2$	
Fine structure under resonant excitation	Phonon replica at 56 and 19 meV	Heavily aged PS Energies typical of Si phonons

Source: Adapted from [145].

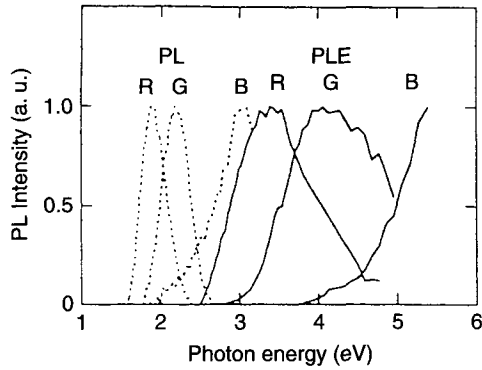


Fig. 29. The red (R), green (G), and blue (B) PL spectra tuned by postanodization illumination (dashed curve) and the corresponding excitation spectra (PLE). Adapted from [163].

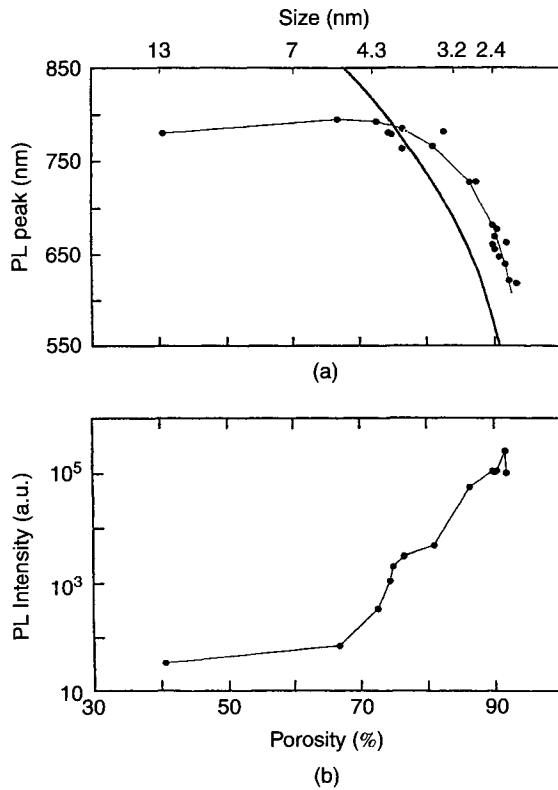


Fig. 30. Plot of the PL peak wavelength and the intensity versus the sample porosity. The thick line is obtained from first-principle calculations. Reprinted with permission after Ref. [164].

Postanodization chemical etching in HF, corresponding to a porosity increase, results in a strong rise in the PL efficiency and in a blueshift of the visible band [165]. The external quantum efficiency can be obtained with values higher than 0.1%, from high-porosity PS layers of all types. But the efficiency normally decreases in the order  $n^-$ ,  $p^-$ ,  $n^+$ ,  $p^+$ .

### 2.5.2. F Band

The F band, so called because of its fast nanosecond decay time, has been the subject of several studies [166, 167]. Some spectral peculiarities of this band are reported in Table VI. This band is observed only in oxidized PS, and it probably originates from contaminated or defective Si oxide [166].

### 2.5.3. IR Band

The IR band presents itself very weakly at room temperature and becomes much stronger at low temperatures [168]. In Figure 31 it is shown how its

Table VI Some Spectral Characteristics of the F Band

Property	Typical values	Comments
Peak wavelength	480 nm	UV excitation at 300 K
PL efficiency	$\geq 0.1\%$	UV excitation at 300 K
FWHM	0.4 eV	UV excitation at 300 K
PL decay times	1 ns	Independent of wavelength and excitation conditions

Source: Adapted from [145].

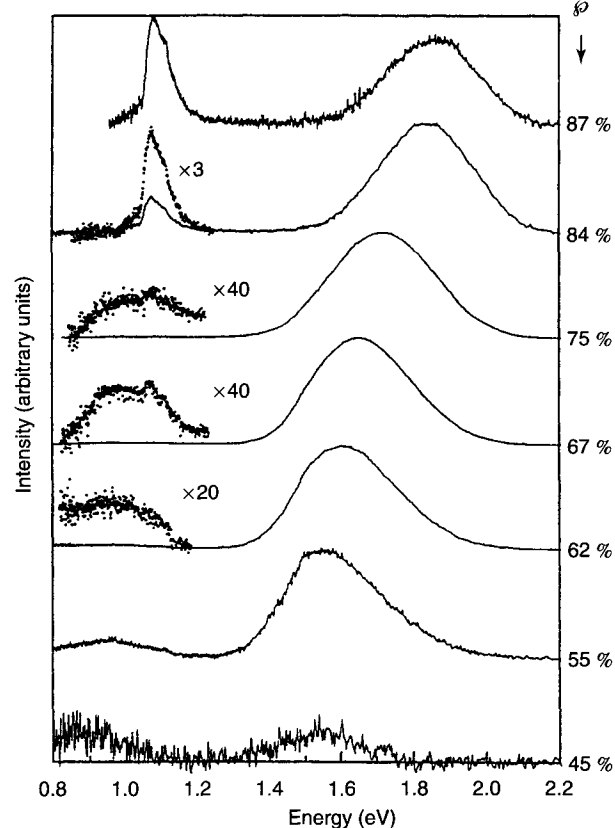


Fig. 31. Room-temperature luminescence spectra of PS samples with different porosities after aging for six months. The excitation energy is 2.541 eV and the power density is  $1.6 \text{ W cm}^{-2}$ . Reprinted with permission after Ref. [2].

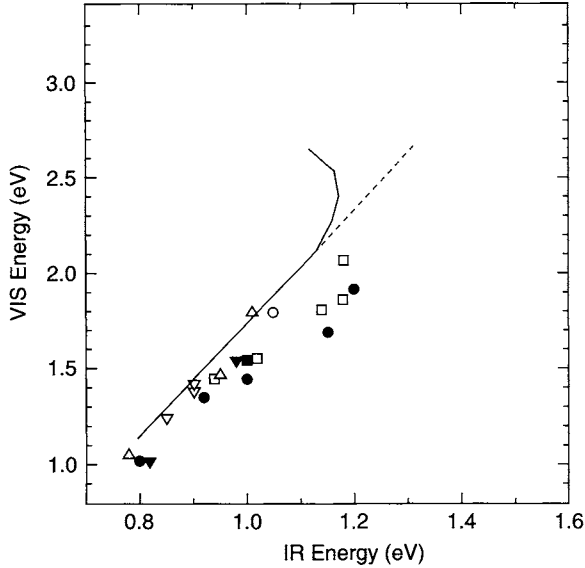


Fig. 32. Plot of the energy position of the S band (named VIS) versus the energy position of the IR band as measured by various authors. The lines are theoretical calculations. Adapted from [169].

peak position scales with the porosity [2]. In addition, its intensity seems to decrease in aged samples. The energy of the IR band follows the energy of the S band according to the 1/3 rule (see Fig. 32) [169]. The origin of the IR band seems to be related to dangling bonds.

#### 2.5.4. Recombination Dynamics

The analysis of the time decay of the visible band gives interesting information. The decay is nonexponential (see Fig. 33 [25]) and is fitted by a stretched exponential function [170, 171]:

$$I_{PL}(t) = I_0 \exp\left(-\frac{t}{\tau}\right)^\beta \quad (12)$$

where  $I_{PL}(t)$  is the luminescence intensity,  $\tau$  is the luminescence lifetime, and  $\beta \leq 1$  is a dispersion exponent. This kind of decay is typical of disordered systems and results from a diffusive motion of the excited carriers [172].

By least squares fits of the experimental data, the dependence of  $\tau$  and  $\beta$  on a large variety of excitation and sample parameters has been measured [17]. The temperature dependence of  $\tau$  has been successfully fitted by the model of an exchange split exciton state confined in a quantum dot [173], where  $\tau$  is determined by the thermal balance of the occupation between the high-energy dipole-allowed singlet state and the low-energy dipole-prohibited triplet state [2].

The time-resolved luminescence results are explained considering that the excitons, before the recombination

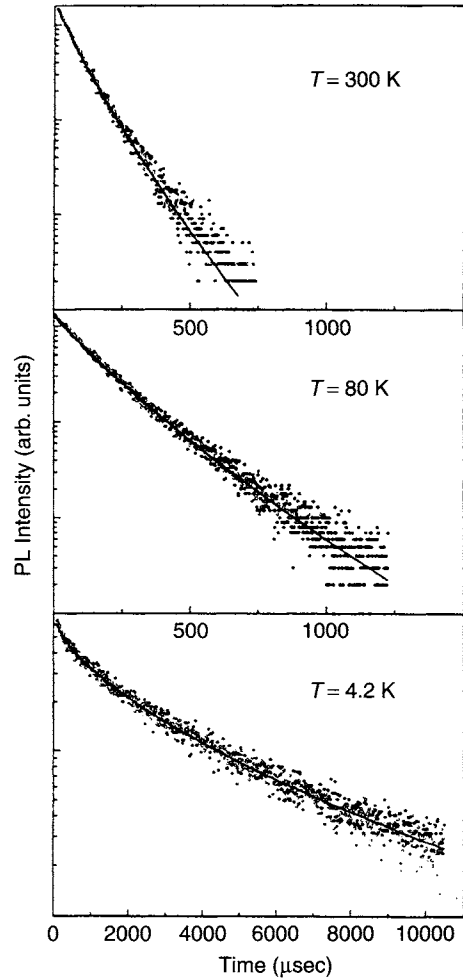


Fig. 33. Time decay of the luminescence of a 60% porosity sample at three temperatures and for an excitation energy of 2.541 eV and observation energy of 1.860 eV. The lines through the data are least squares fit with stretched exponential decays. Adapted from [25].

process, move through the nanocrystal skeleton: recombination is determined both by the on-site recombination process and by exciton diffusion [172]. The exciton diffusion is modeled by the trap-controlled hopping mechanism, which is based on the existence both of a dispersion of nanocrystal energies and of waiting probabilities for hopping from one nanocrystal to another. In this way, the nanocrystals with a low hopping probability and energy act as temporary traps limiting the diffusion [2]. The temperature has a very strong effect on the diffusion. It happens that at low temperatures the role of the temporary traps is very large and leads to a linear increase in  $\beta$  with the temperature, similar to what happens when the diffusion is due to a multitrapping mechanism [170]. At high temperatures, on the other hand, the temporary traps are thermally emptied and the geometrical arrangement limits

the diffusion. In this situation, the diffusion is due to the pure hopping mechanism.

Variations in the porosity also influence the recombination dynamics. As long as the nanocrystals are isolated, the  $\tau$  and  $\beta$  parameters are independent of the sample porosity and depend on the observation energy alone, that is, on the single nanocrystal energy. When the nanocrystals are connected, as in low-porosity samples, the role of diffusion increases and the  $\tau$  and  $\beta$  parameters turn out to be porosity dependent.

### 2.5.5. Aging Effects

Aging effects make an important contribution to the PS luminescence. First, a blueshift in the S band arises from simply storing PS in ambient air at room temperature, as shown in Figure 34 [143]. However, the effect of aging on PS luminescence seems to be contradictory. Even though blueshifts are normally observed with aging, PL efficiencies drop in some cases [133] and rise in others [174]. However, such effects can be explained in terms of both surface passivation phenomena and carrier confinement [1].

The anodic oxidation can dramatically raise the PL efficiency in medium-porosity PS [175], giving an estimated external quantum efficiency (EQE) in the range 1–10%, whereas thermal oxidation at 400–700 °C usually leads to a strong loss of PL efficiency [176]. However, after oxidation at higher temperatures, PS is still luminescent [177]. The quenching of the emission at lower temperature is due to the poor electronic quality of the

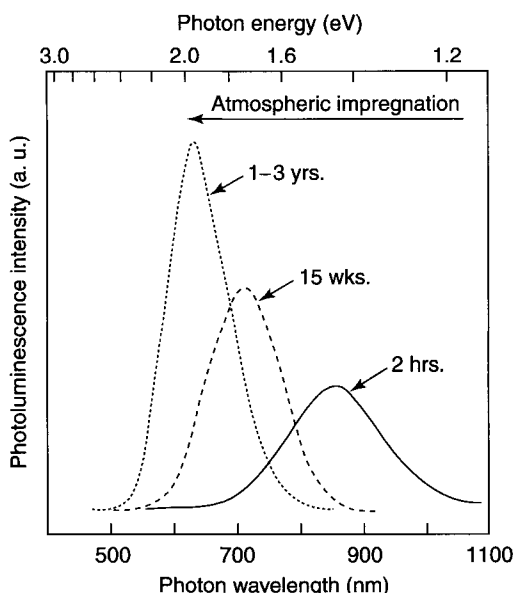


Fig. 34. PL spectra from a PS layer with 77% porosity and thickness 11.6  $\mu\text{m}$  for different aging times. Reprinted with permission after Ref. [143].

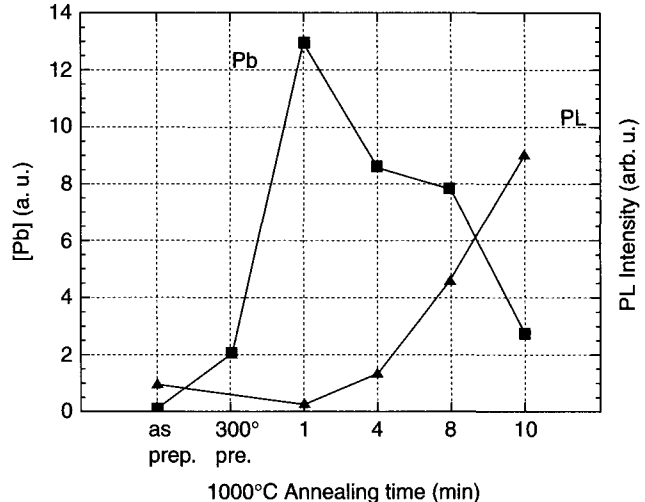


Fig. 35. Dangling bond ( $P_b$ ) concentration and luminescence intensity versus the annealing time at a temperature of 1000 °C in oxygen. Adapted from [178].

Si–SiO<sub>2</sub> interface, as evidenced by electron spin resonance (ESR) spectroscopy [177]. It is worth noting that a clear anticorrelation between dangling bond density and luminescence intensity has been measured (Fig. 35) [178], showing that the oxidation can improve the luminescence as a consequence of increased passivation.

Another important aspect is that the PS luminescence undergoes a significant degradation under normal photoexcitation conditions. It seems that photothermal, photochemical, photoelectric, and photostructural effects are involved in this degradation. The photochemical effects, during illumination in an oxidizing ambient (air), result mainly in a photoenhanced oxidation, which decreases the PL efficiency [179]. This kind of PL degradation is irreversible and can be recovered only partially with an immersion in HF. The photochemical effects can be minimized by illuminating the material under HV atmosphere or in inert atmosphere. Because the PL output is dramatically quenched by raising the temperature, it is possible that photothermal effects are important under strong illumination. Finally, there is also evidence of photostructural effects where light generates or removes competing non-radiative centers, affecting PL efficiency [176, 180].

## 3. DIELECTRIC MULTILAYERS

It is well known that when a light beam is reflected by various dielectric interfaces, an effect of multiple interferences occurs. On this simple principle is based the functioning of dielectric multilayers. A simple scheme of multiple interferences is shown in Figure 36 [2]. Here a single film is compared with a stack of thin films (multilayer). At each interface between two materials, with

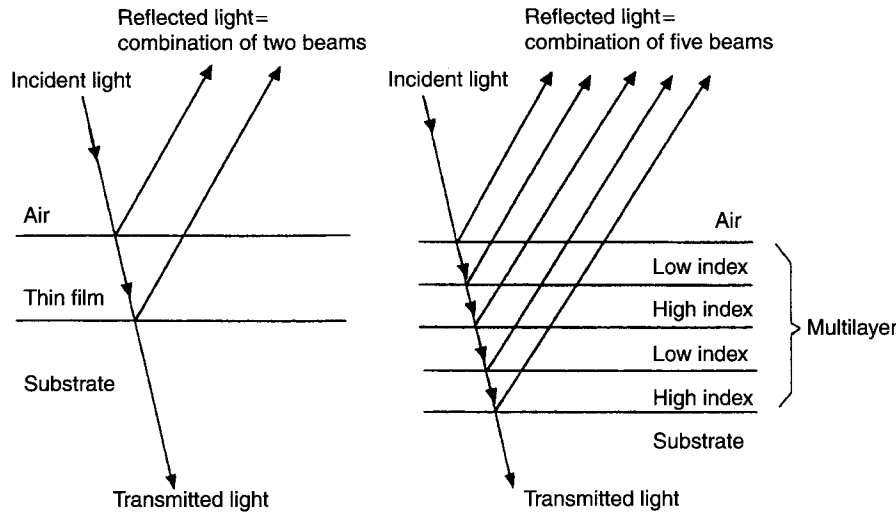


Fig. 36. Reflection and transmission of light by (left) a single thin film and (right) a multilayer. Reprinted with permission after Ref. [2].

different refractive indexes, a reflection occurs. In the case of a single-layer film, the reflected beam is the result of the interference of the two beams reflected at the air–film and film–substrate interfaces. In the case of the multilayer film, the reflected beam is the result of the interference of the multiple beams reflected at each of the different interfaces. By choosing appropriately the thicknesses and the values of the refractive indexes of the various layers, it is possible to generate different reflectivity spectra. The final result is the possibility of realizing constructive and destructive interferences at different wavelengths. To study the case of Bragg reflectors and Fabry-Perot filters, it is worth seeing in detail the interference in the case of a thin slab.

### 3.1. Thin Slab

Let us consider first the simple case of two parallel, partially reflecting surfaces, as shown in Figure 36. Let us define for a thin slab the following quantities:  $R$  the reflectance,  $T$  the transmittance,  $I_0$  the intensity of the primary ray,  $d$  the thin slab thickness,  $\theta$  the angle between any internally reflected ray and the surface normal, and  $n$  the refractive index of the slab material. We can write the phase difference between two successive reflected rays in the following way:

$$\delta = \frac{4\pi}{\lambda} nd \cos \theta \quad (13)$$

where  $\lambda$  is the vacuum ( $\simeq$ air) wavelength. The total phase difference between two successive beams, taking into account that for one reflection the phase change  $\delta_r$ , is equal to

$$\Delta = \delta + \delta_r \quad (14)$$

After some calculations we can express the total reflected ( $I_R$ ) or transmitted ( $I_T$ ) intensity that results from the multiple interference of the rays:

$$I_T = I_0 \frac{T^2}{|1 - R e^{i\Delta}|^2} \quad (15)$$

$$= I_0 \frac{T^2}{1 - R^2} \frac{1}{1 + F \sin^2(\Delta/2)} \quad (16)$$

The last term is known as the Airy function, and an example of this function is shown in Figure 37 [2]. The quantity

$$F = \frac{4R}{(1-R)^2} \quad (17)$$

is called the coefficient of finesse and is a measure of the sharpness of the interference fringes.

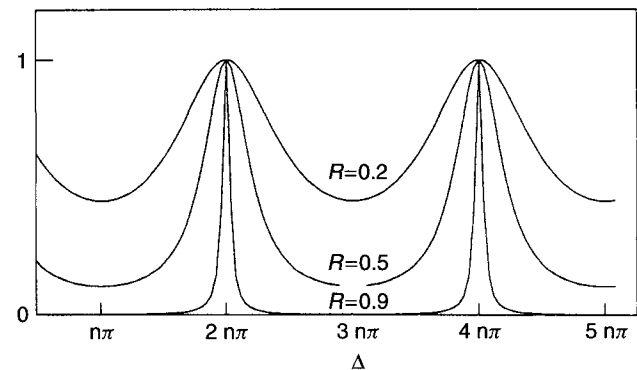


Fig. 37. Plot of the Airy function for three different values of the reflectivity  $R$  as a function of the phase angle  $\Delta$ . Reprinted with permission after Ref. [2].

The condition for a fringe maximum is  $\Delta/2 = m\pi$ , where  $m$  is an integer and is known as the order of interference. It is equal to the equivalent path difference, measured in wavelengths, between two successive beams.

It is possible to extend this formula to the case in which the two surfaces of the thin slab are not identical [181].

In the absence of absorption  $I_R = I_0 - I_T$ . When absorption is present, instead,  $I_R = I_0 - (I_A + I_T)$ , where  $I_A$  is defined as the absorbed intensity.

### 3.2. Bragg Reflectors

Let us now generalize the case of multiple reflections from a thin slab to the case of a multilayer film [2]. In the following we will use the matrix approach to describe the interferences due to the multiple reflected and transmitted beams that come from the different interfaces present in the structure.

For simplicity, we will consider first the simple case of a single dielectric layer of index  $n_1$  and thickness  $d$  inserted between two infinite media with different indexes  $n_0$  and  $n_T$ . Let the incident light be normal to the surface, and let the amplitude of the electric field of the incident beam be  $E_0$ , that of the reflected beam be  $E_R$ , and that of the transmitted beam be  $E_T$ . We can write all in a matrix form

$$\begin{bmatrix} 1 \\ n_0 \end{bmatrix} + \begin{bmatrix} 1 \\ -n_0 \end{bmatrix} \frac{E_R}{E_0} = \begin{bmatrix} \cos kd & -i/n_1 \sin kd \\ -in_1 \sin kd & \cos kd \end{bmatrix} \times \begin{bmatrix} 1 \\ n_T \end{bmatrix} \frac{E_T}{E_0} \quad (18)$$

where  $k = 2\pi n_1 / \lambda$ . If we introduce the reflection and transmission coefficients  $r$  and  $t$ , Eq. (18) is simplified to

$$\begin{bmatrix} 1 \\ n_0 \end{bmatrix} + \begin{bmatrix} 1 \\ -n_0 \end{bmatrix} r = M \begin{bmatrix} 1 \\ n_T \end{bmatrix} t \quad (19)$$

where  $M$  is a matrix known as the transfer matrix. This matrix relates the reflected and transmitted beams.

Let us consider now the case of  $N$  layers, each layer with a refractive index  $n_i$  and thickness  $d_i$ . Using the transfer matrix of each layer  $M_i$ , we can write

$$\begin{bmatrix} 1 \\ n_0 \end{bmatrix} + \begin{bmatrix} 1 \\ -n_0 \end{bmatrix} r = M_1 M_2 \cdots M_N \begin{bmatrix} 1 \\ n_T \end{bmatrix} t \quad (20)$$

$$= M \begin{bmatrix} 1 \\ n_T \end{bmatrix} t \quad (21)$$

By defining the elements of the overall transfer matrix  $M$

$$M = \begin{bmatrix} A & B \\ C & D \end{bmatrix} \quad (22)$$

we can solve Eq. (20) for  $r$  and  $t$  in terms of the following components:

$$r = \frac{An_0 + Bn_T n_0 - C - Dn_T}{An_0 + Bn_T n_0 + C + Dn_T}, \quad (23)$$

$$t = \frac{2n_0}{An_0 + Bn_T n_0 + C + Dn_T}. \quad (24)$$

The reflectance  $R$  and transmittance  $T$  are then given by  $R = |r|^2$  and  $T = |t|^2$ , respectively. Now if we want to obtain a high-reflectance multilayer film, we can use a stack of alternate layers of high index  $n_H$  and low index  $n_L$ . The thickness of each layer has to be equal to  $1/4$  wavelength. In this case, the transfer matrices all will be of the same form and the product of two adjacent ones will be

$$\begin{bmatrix} 0 & -i/n_L \\ -in_L & 0 \end{bmatrix} \begin{bmatrix} 0 & -i/n_H \\ -in_H & 0 \end{bmatrix} = \begin{bmatrix} -n_H/n_L & 0 \\ 0 & -n_L/n_H \end{bmatrix} \quad (25)$$

If the stack consists of  $2N$  layers, then the transfer matrix of the complete multilayer film is

$$M = \begin{bmatrix} (-n_H/n_L)^N & 0 \\ 0 & (-n_L/n_H)^N \end{bmatrix} \quad (26)$$

If we assume for simplicity that  $n_0$  and  $n_T$  are both unity, then

$$R = \left[ \frac{(n_H/n_L)^{2N} - 1}{(n_H/n_L)^{2N} + 1} \right]^2 \quad (27)$$

For large  $N$  the reflectance will approach unity.

This particular stack of  $\lambda/4$  layers is called a dielectric Bragg mirror or reflector and its particular characteristic is to have a high reflectivity, in a given spectral region, centered on the wavelength  $\lambda$ . The reason for this is that all the beams, which are reflected by the multiple interfaces, have the same phase when they reach the top interface. Thus they interfere constructively. For other wavelengths the interference is no longer constructive and the reflectivity consequently drops.

It is worth emphasizing the following considerations, which follow directly from Eq. (27):

1. keeping  $N$  fixed, the reflectivity increases as the ratio  $n_H/n_L$  increases;
2. keeping  $n_H/n_L$  fixed,  $R$  increases with increasing  $N$ .

Some examples of the reflectance spectra of various DBR obtained by varying, respectively,  $N$  or  $n_H/n_L$  are shown in Figures 38 and 39. In these simulations we have considered no absorption,  $n_{\text{air}} = 1$  and  $n_T = n_{\text{Si}} = 4.1$ . The spectra are not symmetric around the central wavelength because of the fact that the symmetry is given

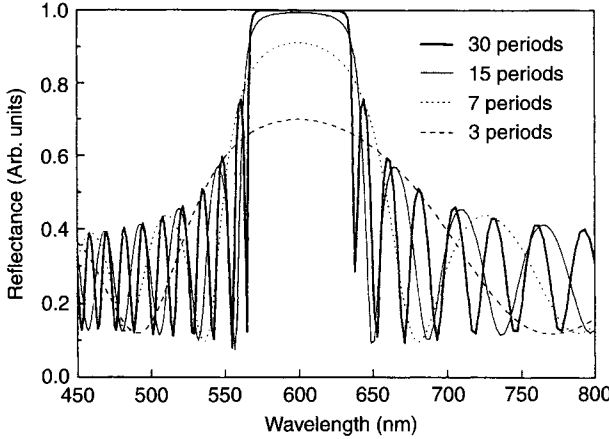


Fig. 38. Simulation of the reflectance spectra of DBR formed by a different number of periods. The high and low refractive indexes have the values 1.5 and 1.27, which correspond to typical PS porosities. Reprinted with permission after Ref. [2].

when the scale is in wavenumber and not in wavelength. Summarizing, we can conclude the following from these simulations:

1. by increasing  $N$ ,  $R$  increases;
2. by increasing  $N$ , the high-reflectivity region, also called the stop band, enlarges;
3. by increasing  $N$ , the stop band becomes sharper;
4. by increasing  $N$ , the value of  $R$  in the stop band increases with respect to the value of  $R$  in the side-lobes;
5. by increasing  $n_H/n_L$  the stop band enlarges and sharpens;

6. by increasing  $n_H/n_L$  the overall reflectance value increase, that is, both in the stop band and in the side-lobes.

### 3.3. Fabry-Perot Interference Filters

By using two parallel mirrors separated by a spacer, it is possible to construct a particular class of interferometers called Fabry-Perot (FP) interference filters [181]. These filters have a very narrow passband and are based on the multiple reflections from two parallel mirrors. It follows that we can apply Eq. (16), and the transmittance of the filter is given by the Airy function (Fig. 37). For  $\lambda = mnd$ , where  $n$  and  $d$  are the refractive index and thickness, respectively, of the region between the two mirrors, maxima in the transmittance (FP resonances) are observed. The resolution of the filter is given by its finesse  $F$  (see Eq. (17)). A relation between the width  $\Delta\lambda$  of the FP resonance at  $\lambda$  with the FP finesse, exists:

$$\frac{\Delta\lambda}{\lambda} = mF \quad (28)$$

where  $m$  is the order of the resonance.

Dielectric multilayers constitute a particular class of FP filters. Dielectric FP filters usually work at low interference order. The idea is to use two DBRs separated by a spacer formed by a dielectric material with a different refractive index of the DBR. In this way the spacer should be  $\lambda$  or  $\lambda/2$  thick if one wants to work at the second or at the first interference order (see Eq. (13)). Figure 40 shows the scheme of a FP filter based on dielectric films [2].

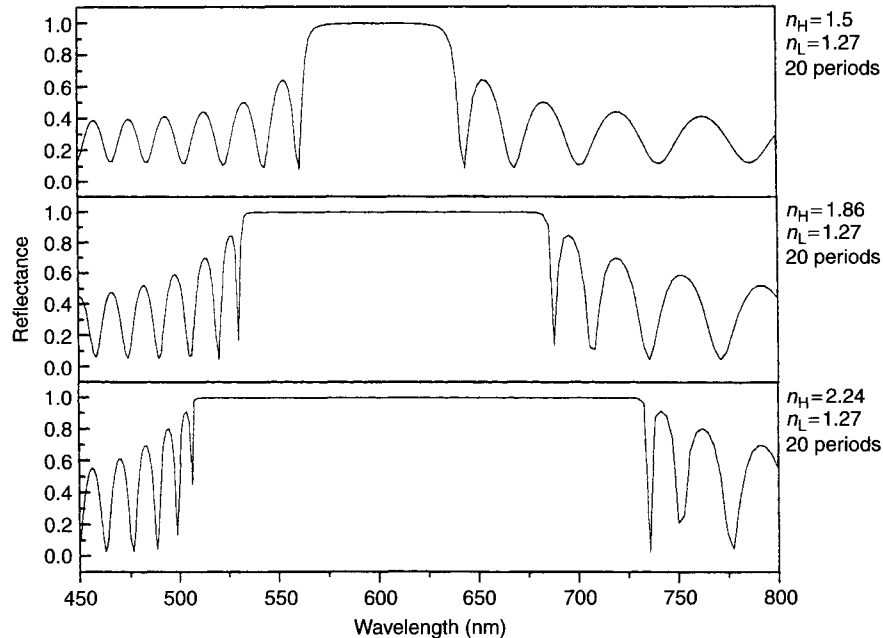


Fig. 39. Simulation of the reflectance spectra of DBR formed by a different ratio between the high and low refractive index. Reprinted with permission after Ref. [2].

Let H or L be the  $\lambda/4$ -thick layer of high or low refractive index; then a periodic repetition of HL layers forms the DBR. The structure of a FP filter could be HL $\cdots$ HL-HL-LH $\cdots$ LH or HL $\cdots$ HL-LL-HL $\cdots$ HL, where the underlining emphasizes the spacer or central layer  $2 \times \lambda/4$  thick [2].

Some simulations of the reflectance spectra of FP filters are reported in Figures 41 and 42. Some considerations are as follows [2]:

1. To obtain a good finesse value it is necessary to have a DBR with high reflectivity (large period number or high dielectric mismatch).
2. The finesse is increased by increasing the period number. However, by increasing the reflectivity, the transmittance of the FP decreases. A trade-off is necessary between high finesse and high transmittance.
3. The transmittance peak is not zero as expected from the theory. This is due to the fact that the structure simulated

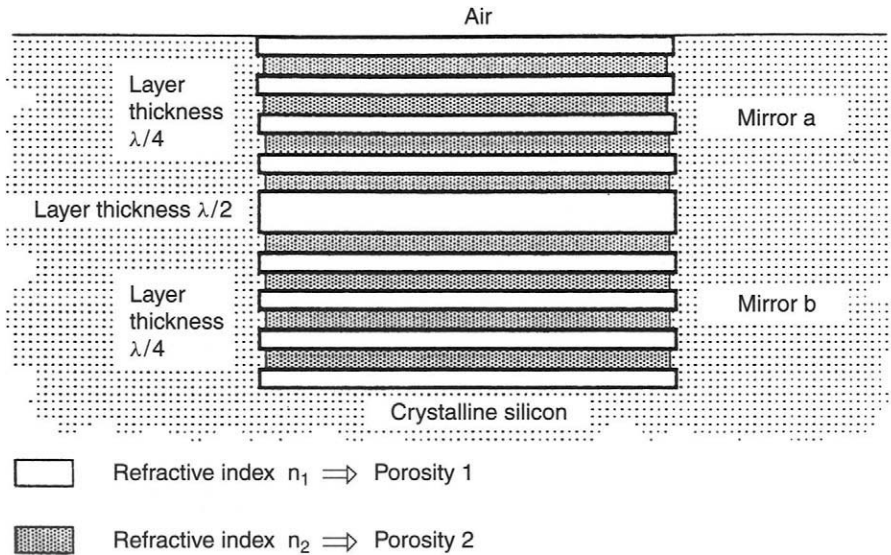


Fig. 40. Simple diagram of the structure of FP formed by PS. Reprinted with permission after Ref. [2].

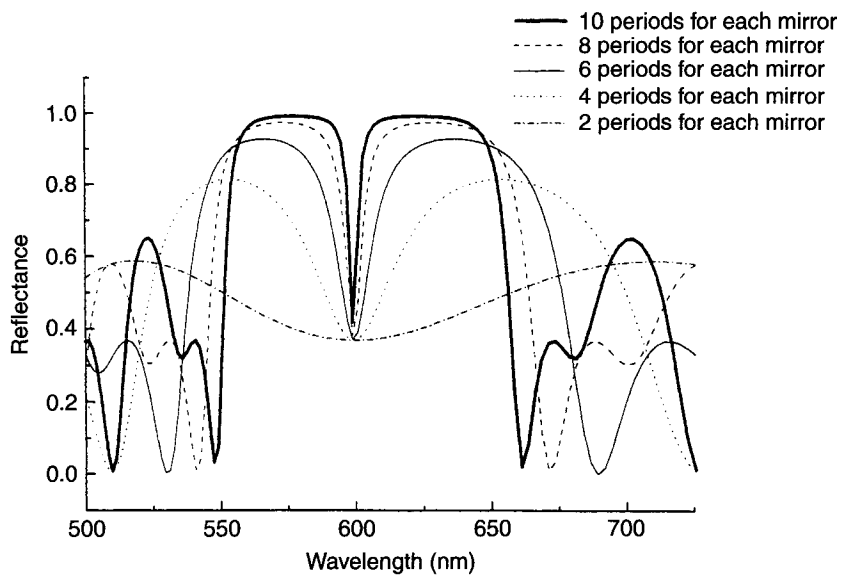


Fig. 41. Simulations of the reflectance spectra for various FP formed by a different number of periods in the DBR. Lower and higher refractive index value are, respectively, 1.27 and 1.5. The FP is symmetric. Reprinted with permission after Ref. [2].

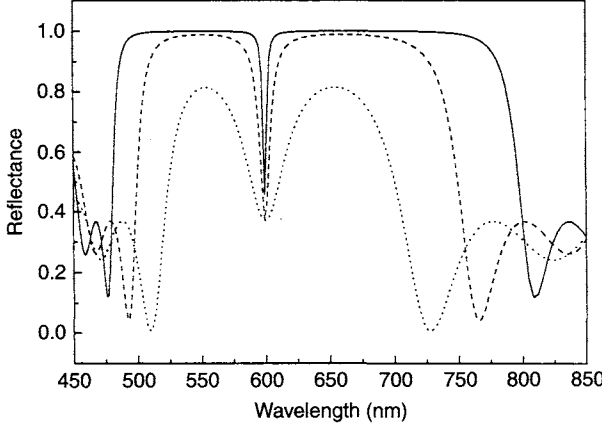


Fig. 42. Simulation of the reflectance spectra for FP formed by different ratios between high and low refractive indexes of the DBR. The low refractive index value is 1.27 for all the curves. Instead the high refractive index value is 2.24 (solid line), 1.86 (dashed line), and 1.5 (dotted line). The DBR are formed by four periods. Reprinted with permission after Ref. [2].

is not symmetric but asymmetric (on one side there is the air, on the other side there is the Si). To correct this problem one has to use two DBRs with different reflectivities.

#### 4. SEMICONDUCTOR MICROCAVITIES

The spontaneous emission rate  $R_{sp}(\hbar\omega)$  of a semiconductor is given by the product of the electronic matrix element and the photon mode density; more precisely,

$$R_{sp}(\hbar\omega) = (2\pi/\hbar) \sum_{f,i} |\mathcal{H}_{if}|^2 G(\hbar\omega) P_i (1 - P_f) \delta \times (E_{fi} - \hbar\omega) \quad (29)$$

where the sum is over all the initial ( $i$ ) and ( $f$ ) final states separated by an energy  $\hbar\omega$ ;  $|\mathcal{H}_{if}|^2$  describes the interaction Hamiltonian between the initial and final electronic states,  $G(\hbar\omega)$  is the photon mode density, and  $P_i$  and  $(1 - P_f)$  are the probability that the initial state is occupied and the final state is empty, respectively. During the last few years a great deal of research work has been performed to modify the emission rate by reducing the dimensionality of the electronic system (see Fig. 43) [182]. Electrons have been confined in quantum wells, quantum wires, and quantum dots. The electronic density of states has changed accordingly. As a result, the broad emission features of three-dimensional electronic systems, which result from the coupling of two continua of electronic and photonic states, have narrowed, as a result of the change in the density of states of the electronic systems. Linewidths as narrow as some micro-electron-volts have been observed for recombinations in quantum dots.

A different approach proposes acting on the photon mode density (see Fig. 43) by enhancing or inhibiting it. This is an important part of the relatively new field called cavity quantum electrodynamics [183, 184]. By decreasing the volume available to the photon modes, that is, by confining the photons into an optical (micro)cavity (i.e., a quasi-two-dimensional system), into an optical fiber (one-dimensional systems), or into photon boxes (zero-dimensional systems), sharper and sharper emission features are obtained (see Fig. 43). It is worth saying here which are the main proposed applications of such structures:

- microlasers (e.g., vertical cavity surface emitting lasers (VCSELs) [185];
- wavelength tunable resonant cavity light emitting diodes (RCLEDs) [186];

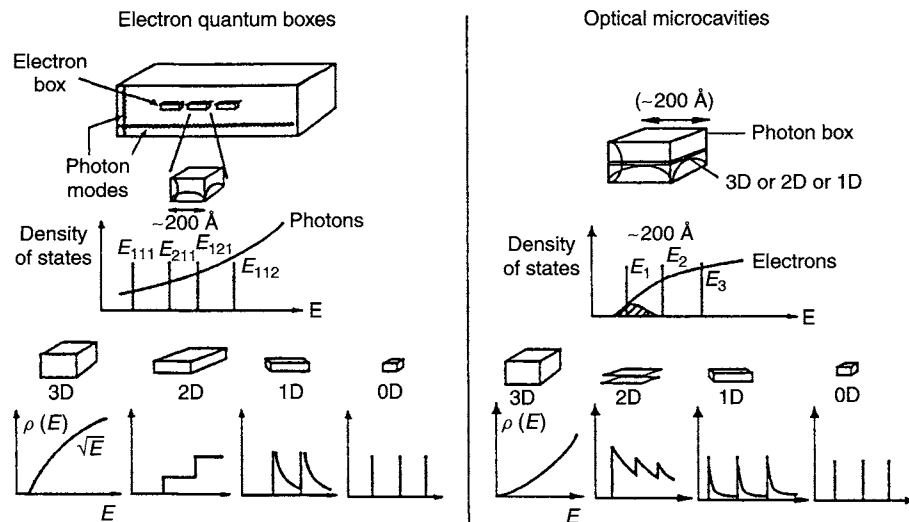


Fig. 43. Schematic diagram of the effects of quantization on the electronic density of states (left) and photon density mode (right). Reprinted with permission after Ref. [182].

- second harmonic generators with enhanced efficiencies [187];
- superradiant light-emitting diodes (LEDs) [187];

It is worth saying that photon confinement structures also are achieved via photonic band gap materials. We concentrate our attention here only on microcavities; for an introduction to the former, the reader is referred to [188]. Light confinement in a planar microcavity is based on the amplitude buildup of the photon mode because of multiple in-phase reflections that occur on localized mirrors. [185]. The allowed photon states correspond to the resonances of these FP-like systems. In analogy with electronic systems, one can consider allowed photon states (the resonances) for which light transmission through the FP is allowed; that is, photon states exist in the cavity, and inhibited photon states (the wavelength region corresponding to the DBR stop band) for which light transmission through the FP filter is not allowed and all the light is back-reflected. All this applies to normal-incidence light. For light propagating in the cavity plane, such an argument does not apply and the photons are free to propagate into the plane. The situation in the intermediate region of incidence angle is different: the Bragg reflectors behave as ideal mirrors (in the stop-band wavelength region) only within a certain incidence-angle range. For a given Bragg reflector we can define a “Bragg angle”  $\theta_{\text{Bragg}}$ , which depends on the refractive indexes and thicknesses of the layers composing the mirror, such that, when the angle of incidence  $\theta_{\text{inc}}$  is

$$\theta_{\text{inc}} < \theta_{\text{Bragg}} \quad (30)$$

the reflectivity approaches the value 1 and when

$$\theta_{\text{inc}} > \theta_{\text{Bragg}} \quad (31)$$

it rapidly drops (with weak oscillations) to zero. It must be said that this picture also depends on the polarization of the incident light. The dependence of the reflectivity of a Bragg reflector on the incidence angle is visualized in Figure 13 of [185].

#### 4.1. Weak Coupling Mode

When the coupling between the photons and the electronic excitations is weak (for a quantitative description see [185]), it is possible to treat the “photonic” and “electronic” parts of Eq. (29) as separate and independent systems.

Let us consider a planar Fabry-Perot cavity with mirror transmittivity  $T$  and reflectivity  $R$ ; the mirrors are spaced  $d$  apart, leading to a vertically propagating mode with wavelength  $\lambda = nd$ . The mode amplitude in the cavity region is  $4/(1 - R)$ , whereas that of perpendicular nonresonant modes (at different  $\lambda$ ) is suppressed by a factor  $(1 - R)$  [189]. The same happens when one considers modes at a given wavelength but at different angle  $\phi$ , for which the resonant mode wavelength would be  $\lambda_c(\cos \phi)^{-1}$ . The same suppression factor  $(1 - R)$  would be obtained for nonresonant modes, that is, at angles different from the normal. The unique feature of microcavities is therefore to concentrate the field intensity into the resonant mode as much as it is suppressed in other modes, with a more or less constant lifetime.

The factor of merit describing the control of spontaneous emission into a desired mode is called the spontaneous emission factor  $\beta$ :

$$\beta = \frac{\text{spontaneous emission in the desired mode}}{\text{spontaneous emission in all the modes}} \quad (32)$$

To bring  $\beta$  to unity, one has to deal with the recombination into the other competing modes (see Fig. 44) [189]:

- into leaky waveguide modes of the DBR—the Bragg mirrors are efficient up to a critical angle  $\theta_{\text{Bragg}} = (n_2 - n_1)/n$ , where  $n_1$ ,  $n_2$ , and  $n$  are the refractive indexes of the two materials and their average, respectively; beyond  $\theta_{\text{Bragg}}$ , the Bragg mirror acts as a homogeneous dielectric medium with average index  $n$ , as already said;
- into guided modes, which are particularly important when the spacer layer has a higher refractive index than the average of the DBR;
- into oblique modes, whenever the emission spectrum is broader than the cavity linewidth—emissions into modes at wavelengths different than the cavity wavelength are redistributed into cones of monochromatic light; in this way, even if the emission spectrum is narrow, the  $\beta$  factor is reduced because of an imperfect coupling into the cavity mode.

Multiple reflections in a microcavity select an escape cone that is much smaller than the angle  $2\pi$  of a Lambertian source. This builds up the light emission in a given direction, leading to directionality. Another useful effect is that of spectral narrowing as a result of the spectral width of the allowed mode.

#### 4.2. Strong Coupling Mode

Modification of the spontaneous emission rate, resulting from the aforementioned weak coupling between photons and electronic excitations, is not the only effect of photon confinement. In fact, if the coupling between the electronic excitation and the photon mode is strong enough, a resonant transfer of excitation between the two states (Rabi oscillations) settles in and dominates the weak coupling. A great deal of work, both experimental and theoretical, has been devoted to describing and realizing the strong

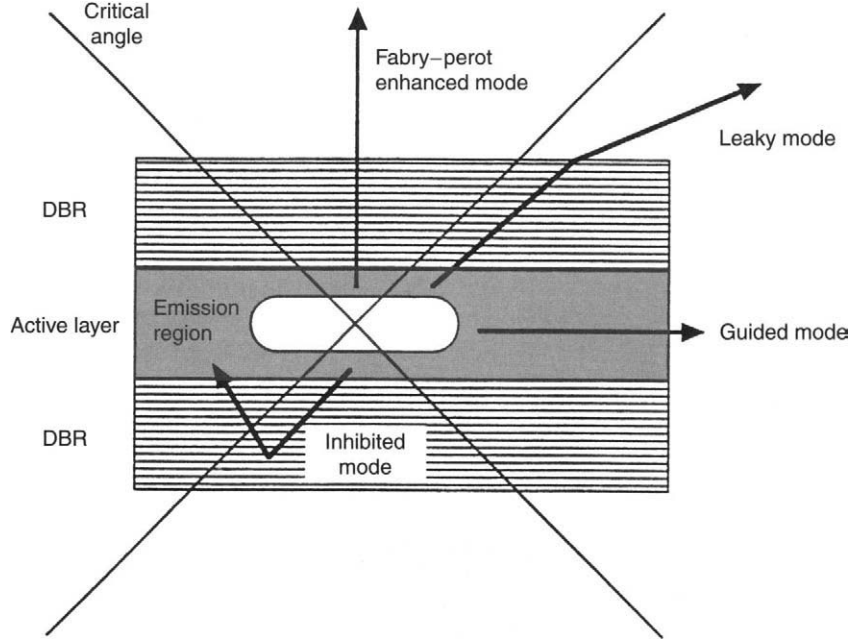


Fig. 44. Outline of the various competing modes in a microcavity. Reprinted with permission after Ref. [2].

coupling case, in particular for the possibility of exploiting it in novel, enhanced-performance, nonlinear optical devices. However, a review of this is far beyond the aim of this chapter. The interested reader is referred to [190].

## 5. POROUS SILICON MULTILAYERS

The ideas discussed for dielectric microcavities also can be applied to porous silicon; in this way PSMs are obtained.

When the wavelength of the incident light is much larger than the typical nanocrystal size, it is possible to use the effective medium approximation in modeling the dielectric response of PS. A problem is the choice of the appropriate effective medium, that is, of the mean between the various components that form PS. A valid approximation for spherical particles is the Maxwell-Garnett approximation, which yields an effective dielectric constant  $\epsilon_{\text{eff}}$  [157]

$$\frac{\epsilon_{\text{eff}} - \epsilon_M}{\epsilon_{\text{eff}} + 2\epsilon_M} = f \frac{\epsilon - \epsilon_M}{\epsilon + 2\epsilon_M} \quad (33)$$

where  $f$  is a free parameter describing the volumetric fraction,  $\epsilon$  is the dielectric function of the spherical particles (silicon), and  $\epsilon_M$  is the dielectric function of the embedding medium (the air). An extension of this approximation is given by the symmetric expression of

the Bruggeman equation [157]

$$f \frac{\epsilon - \epsilon_{\text{eff}}}{\epsilon + 2\epsilon_{\text{eff}}} + (1 - f) \frac{\epsilon_M - \epsilon_{\text{eff}}}{\epsilon_M + 2\epsilon_{\text{eff}}} = 0 \quad (34)$$

From Eq. (34) and by assuming that  $\epsilon_M \simeq 1$ ,  $n_{\text{eff}}^2 \simeq \epsilon_{\text{eff}}$ , that is, the PS film would have a negligible absorption coefficient (at the considered wavelength), one can obtain the volumetric fraction  $f$

$$f = \frac{(1 - n_{\text{eff}}^2)(n^2 + n_{\text{eff}}^2)}{3n_{\text{eff}}^2(1 - n^2)} \quad (35)$$

Figure [45] shows a comparison of the porosity deduced by a gravimetric method with that deduced by this formula, where  $n$  is experimentally determined. The linear fit has a slope of  $1.1 \pm 0.1$  and an intercept of  $0 \pm 5$ .

The main technique for measuring the refractive index of PS is the use of spectroscopic ellipsometry [191]. However, for multilayered samples, the etching parameter dependence of the refractive index has been widely deduced by measurement of the reflectivity of the samples. One approach, mainly used by Theiß and coworkers [157], is based on the least squares fit of the reflectance spectrum with a model of the dielectric function, such as that of Eq. (35). Another approach, used by us, relies measurements of the interference fringes from the multilayered PS structure under study. This method has the advantage of being fast and easy. Figure 46 shows the normal incidence reflectance spectrum of  $p^+$ -type doped silicon wafers and the deduced refractive index,

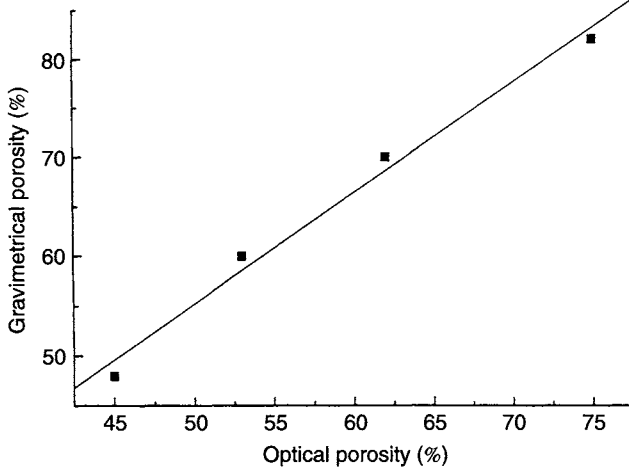


Fig. 45. Comparison of the porosity as deduced by gravimetric measurements with the one deduced by optical measurements. Reprinted with permission after Ref. [2].

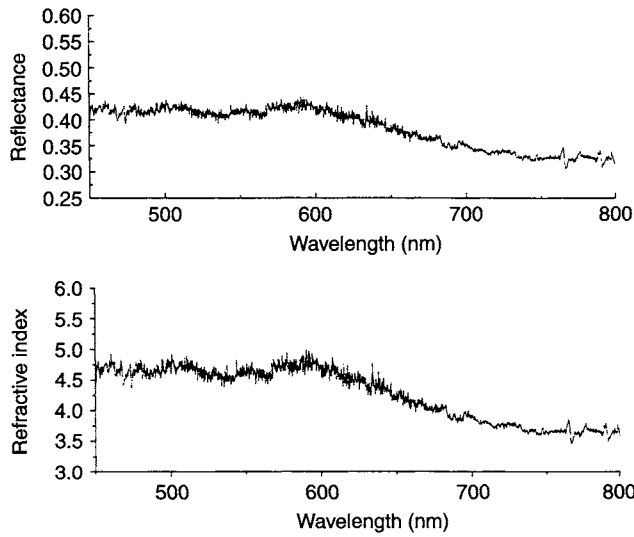


Fig. 46. Normal incidence reflectance spectrum of a Si wafer (top) and the deduced refractive index (bottom). Reprinted with permission after Ref. [2].

where

$$n_{\text{Si}} = \frac{1 + \sqrt{R}}{1 - \sqrt{R}} \quad (36)$$

Figure 47 shows the reflectance spectrum of a 75% porosity PS film, 6.8  $\mu\text{m}$  thick. The spectrum is characterized by the multiple interference fringes caused by the air-PS and PS-Si interfaces. By assuming that the PS film has parallel surfaces and that the refractive index is a smooth function of the wavelength, it is possible to deduce from the wavelength position of adjacent reflectance maxima

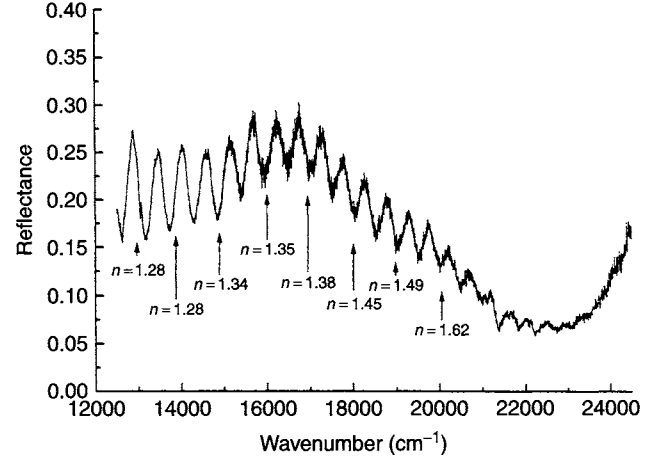


Fig. 47. Normal incidence reflectance spectrum of a 75% porosity sample with a thickness of 6.8  $\mu\text{m}$ . The arrows indicate the fringe position and the refractive index value as deduced with Eq. (38). Reprinted with permission after Ref. [2].

or minima the value of the refractive index [181],

$$2nd \left( \frac{1}{\lambda_r} - \frac{1}{\lambda_{r+1}} \right) = 0 \quad (37)$$

where  $d$  is the porous layer thickness and  $\lambda_r$  is the wavelength of the  $r$ th reflectance maximum or minimum. By solving for  $n$ ,

$$n = \frac{1}{2d} \left( \frac{1}{\lambda_r} - \frac{1}{\lambda_{r+1}} \right)^{-1} \quad (38)$$

An error of 5%, on the refractive index so determined, can be roughly estimated. This procedure has been followed for various porosities and the results are reported in Figure 48. It is observed that the  $n$  values are lower than

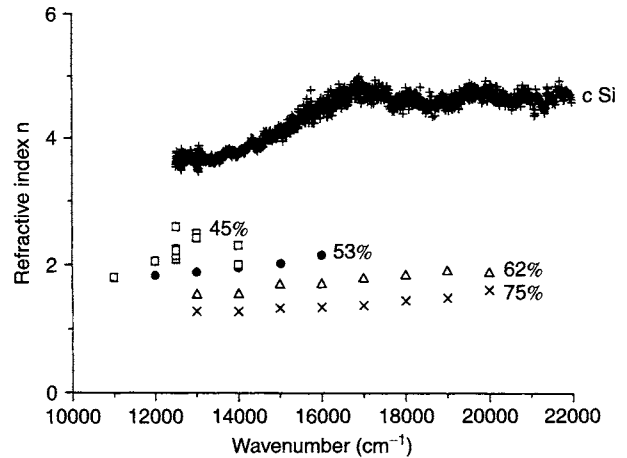


Fig. 48. Plot of the refractive index versus the wavelength for different porosity samples obtained via Eq. (38). Reprinted with permission after Ref. [2].

those of Si and that increasing the porosity decreases  $n$ ; this is comprehensible, because when the porosity increases it means that the percentage of voids in the PS structure increases and the total refractive index, which will have an intermediate value between Si and air, will approximate even more its value to that of air (roughly 1).

### 5.1. Producing Porous Silicon Multilayers

Two main ways of producing PS multilayers have been proposed [192]: by periodically varying the etching parameters (such as, e.g., the current density or the light power on the surface of Si under etch) or by using periodically doped substrates and maintaining constant the various etching parameters. In the following we discuss the first approach, because it is more easily accomplished and it has been the one employed by us [19, 187, 193–195].

This approach is based on the following statements:

- the etching process is self-limited (once a porous layer is formed, the electrochemical etching of this layer stops);

- the etching occurs mainly in correspondence to the pore tips;
- the porosity depends only on the current density once the other etching parameters are kept fixed;
- the refractive index of PS,  $n$ , depends on its porosity.

Hence, by varying the current density during the etching process, it is possible to vary the porosity in the etching direction only at the etch front (Fig. 49 [196]). In this way, the current-versus-time profile is transferred to the porosity-versus-depth profile, that is, the  $n$ -versus-depth profile (see Fig. 50).

The choice of the substrate doping and of the HF concentration has to be made carefully to obtain the maximum variation of the porosity, that is, of  $n$ , within a given range of current density. Various substrate dopings have been used, and variations of porosities have ranged between 25 and 75% for  $0.01 \Omega \text{ cm}$  and between 55 and 75% for  $0.2 \Omega \text{ cm}$  [194]. For porosities higher than 75% a “peeling off” of the porous silicon layer was observed. Figure 51 shows the effective refractive index, measured by ellipsometry, as a function of the current density for

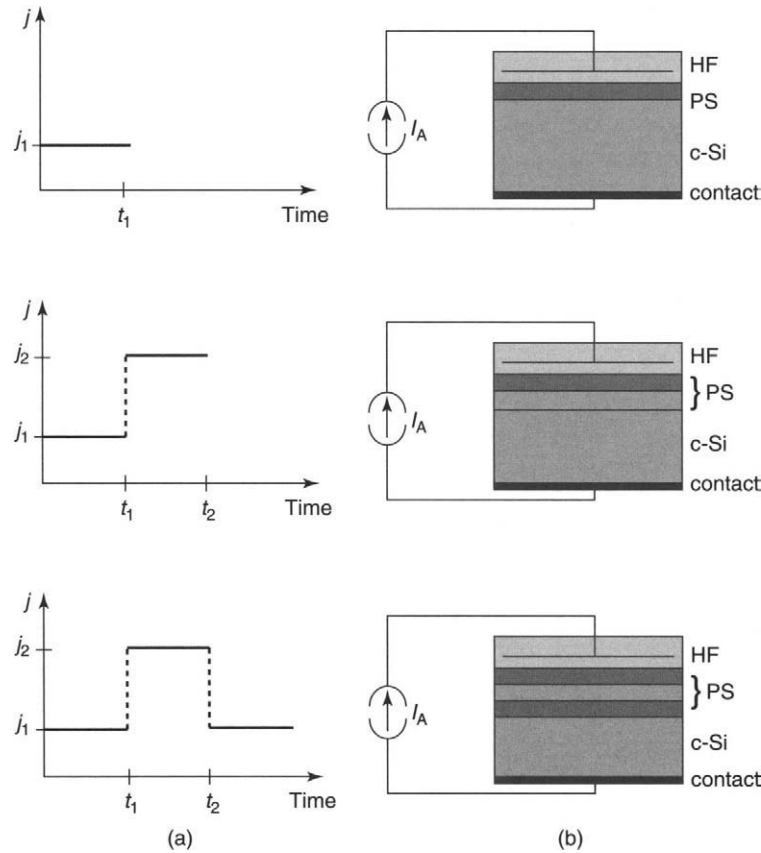


Fig. 49. Schematic sketch of the formation principle of a PS multilayer structure: (left) time dependence of the current density; (right) actual layer sequence. Adapted from [196].

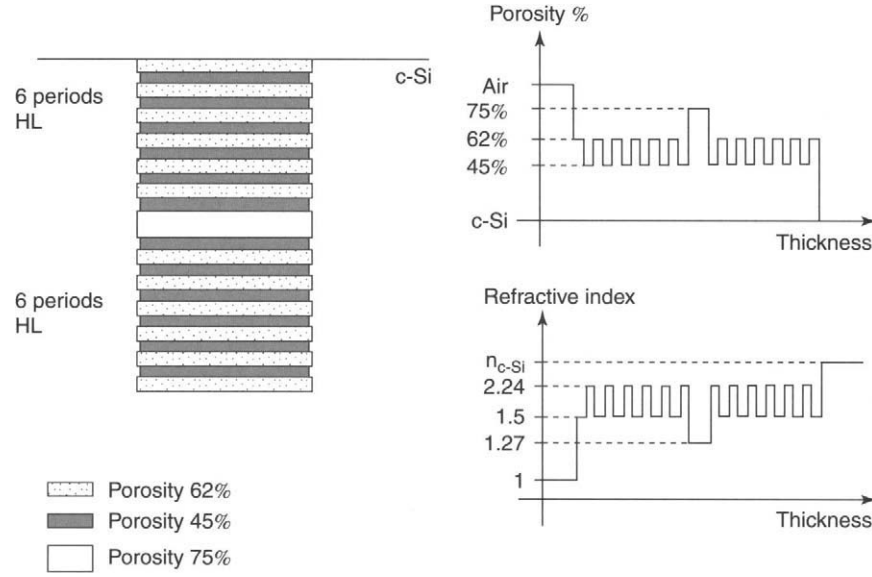


Fig. 50. Diagram of FP structure (left) and of the corresponding porosity and refractive index sequence, respectively (right). Reprinted with permission after Ref. [2].

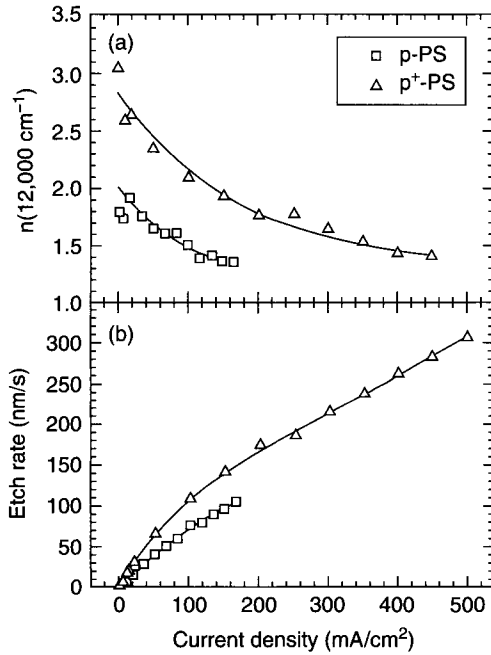


Fig. 51. Effective refractive index at  $12,000 \text{ cm}^{-1}$  (a) and etch rate (b) plotted as a function of the anodization current density for two substrate doping levels. Reprinted with permission after Ref. [197].

two substrate dopings [197]. Larger variations in  $n$ , for the heavily doped substrates, were measured. Figures 52 and 53 show porosity versus current density and etch rate versus current density for  $p$ -type doped substrates ( $0.01 \Omega \text{ cm}$ ) and for three different HF concentrations:

10%, 15, and 20% [19, 198]. Some comments are worthwhile:

- the porosity is a linear function of the current density, for a given [HF], in a restricted interval of current densities;
- increasing the [HF] and keeping current density fixed, the porosity of the resulting layer decreases;
- the relatively larger porosity variation is obtained for  $[\text{HF}] = 15\%$ , by varying the current; indeed, porosities between 42 and 83% were obtained by increasing the current density between 1 and  $200 \text{ mA cm}^{-2}$ . For similar current variations, the porosity changed only between 71

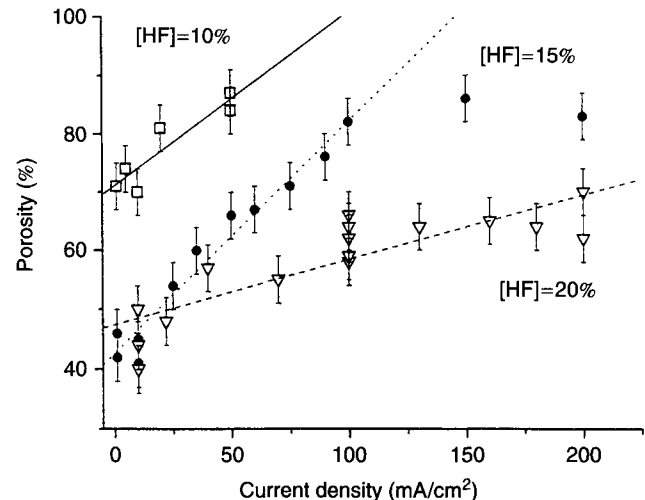


Fig. 52. Porosity dependence on the current density for various volumetric HF concentrations ( $[\text{HF}]$ ). The resistivity of the substrate is  $0.01 \Omega \text{ cm}$ . Reprinted with permission after Ref. [2].

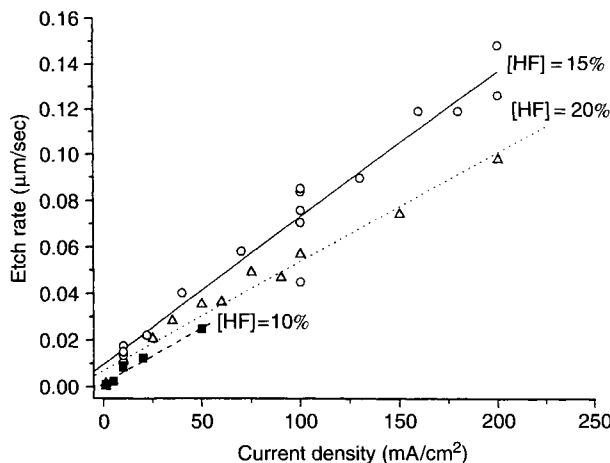


Fig. 53. Etch rate versus etch current density for various volumetric HF concentrations and for a substrate resistivity of  $0.01 \Omega \text{ cm}$ . Reprinted with permission after Ref. [2].

and 87% for  $[\text{HF}] = 10\%$  and between 45 and 70% for  $[\text{HF}] = 20\%$ ;

- the etch rate is a linear function of the current densities;
- the etch rate depends slightly on  $[\text{HF}]$ .

The refractive index and etching rate values obtained for a single layer are modified in the presence of a multilayer structure. Some explanations of this have been proposed in the literature: current focusing and defocusing [199] or porosity gradients at the interface [194]. To solve this problem,  $n$  and the etch rate  $V$  of a given porosity film in the presence of a multilayer structure could be measured by growing Fabry-Perot filters and looking at the angle dependence of the wavelength of the transmittance maximum  $\lambda_c$ , which is given by [181]

$$\lambda_c = 2n_c d_c \left[ 1 - \left( \frac{\sin \phi}{n_c} \right)^2 \right]^{1/2} \quad (39)$$

where  $n_c$  and  $d_c$  refer to the central layer, and  $\phi$  is the angle with respect to the normal to the surface of the sample. From least squares fits of the experimental data with Eq. (39), both  $n_c \times d_c$  and  $n_c$  can be determined separately and, hence, by knowing the etching time, it is possible to obtain  $V$ . Such an experiment has been performed and it was found that the  $n_c$  and  $V$  values are systematically lower than the values determined for a thick film of the same porosity, that is, obtained with the same current [198]. For example, for a 53% porosity layer on a  $0.01 \Omega \text{ cm}$  substrate,  $n = 1.64$  at 714 nm and  $V = 0.018 \mu\text{m s}^{-1}$  were measured, whereas for a thick film  $n = 1.95$  at 714 nm and  $V = 0.021 \mu\text{m s}^{-1}$  were measured. These results (i.e., lower  $n$  and  $V$  in multilayers than in thick monolayer samples) have been systematically observed. However, the characterization of

several different porosity films by using this method is very time-consuming, and what is important for the modeling of FP filters and DBRs is the product  $n_c \times d_c$ . Consequently, one can use  $n_c$  as determined on thick samples and modify  $V$  according to the results of FP resonance wavelength measurements at normal incidence, where  $\lambda_c = 2 \times n_c \times d_c$ . The results of such determinations are given in Table VII.

At first glance, PS multilayers are different from PS single layers because of their bright and colorful appearance. In addition, quantitative reflectance measurements show very high values of the reflectance maxima and narrow FP resonances [198].

More detailed characterizations of the interfaces have been carried out with transmission electron microscopy. Figure 54 shows a TEM image of a PS multilayer [194]. The low-porosity layers appear darker in the image because of the high density of the material. The interfaces between layers of different porosity are sharp on a nanometric scale. Moreover, the lateral roughness on a scale of several hundred nanometers is very low for the

Table VII Porosity  $P$ , Current Density  $J$ , Etch Rate, and Refractive Index  $n$ ;  $P$  Is Measured by Gravimetric Techniques and  $n$  Is Given at 600 nm

$P$ %	$J$ (mA cm <sup>-2</sup> )	Etch rate		$n$
		Thick sample ( $\mu\text{m s}^{-1}$ )	Multilayer sample ( $\mu\text{m s}^{-1}$ )	
53	25.0	0.021	0.015	2.24
62	49.7	0.035	0.021	1.74
75	82.8	0.055	0.040	1.37

Source: Adapted from [2].

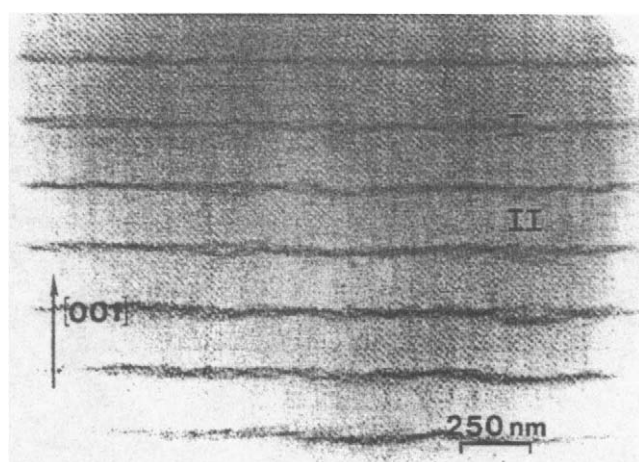


Fig. 54. Transmission electron microscopy cross section of a PS multilayer formed on a  $p$ -type doped substrate ( $0.2 \Omega \text{ cm}$ ): (layers I) 64% porosity and 20 nm thickness; (layers II) 84% porosity and 200 nm thickness. Reprinted with permission after Ref. [194].

topmost interface and increases slowly with depth. This roughness is expected to be due to the inhomogeneity in the substrate and accumulates more and more during the propagation of the etching front [196]. Indeed, it is absent in epitaxial layers, which have a higher crystalline quality [200].

Gravimetric measurements on single layer and porosity multilayers are often in disagreement, revealing a lower mean porosity in the multilayer structures than in the single layer structures [194]. This is thought to be due to porosity gradients. The porosity gradient at the interface might be due to recharging effects of capacities in the etching cell [194]. Figure 55 shows the experimental diffraction pattern of a 10-period PS multilayer [86]. As can be seen, a number of satellite peaks are detected, revealing high-quality multilayer structures. No progressive broadening of the satellite peaks is observed, which indicates a good lateral stability of the mean period. Some observed splitting on the large-angle side of the satellite peak reflects some slight variation in the depth of the multilayer period. The satellite intensity also decreases with higher satellite order as a result of graduated interfaces that come from the porosity gradient mentioned previously.

It has been demonstrated that a variation of the sample resistivity can lead to porosity variations [201]. Hence, a periodic modulation in depth of the dopant concentration in a Si wafer causes a periodic variation in the porosity once PS has been etched. In [192, 194, 202] this kind of approach has been used. By CVD, 10 and 5 periods of 75 nm (150 nm) thick *p*-type doped silicon layers at free-carrier concentration levels of  $1 \times 10^{17} \text{ cm}^{-3}$  ( $1 \times 10^{19} \text{ cm}^{-3}$ ) were grown. The etching has been carried out in the dark with a constant current density of  $50 \text{ mA cm}^{-2}$ . Some very sharp interfaces were observed (see Fig. 56 [202]) with a three-layer structure as a result

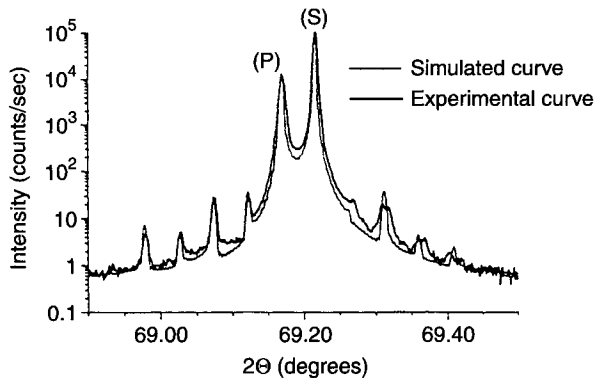


Fig. 55. Experimental and simulated  $\theta - 2\theta$  diffraction patterns, plotted on a semilogarithmic scale, around the (0 0 4) reflection of a PS multilayer composed of 10 periods of a 36% porosity and 112-nm thickness layer and 60% porosity and 73-nm thickness layer. (P) and (S) are the Bragg peaks of the PS multilayer and of the substrate, respectively. Adapted from [86].

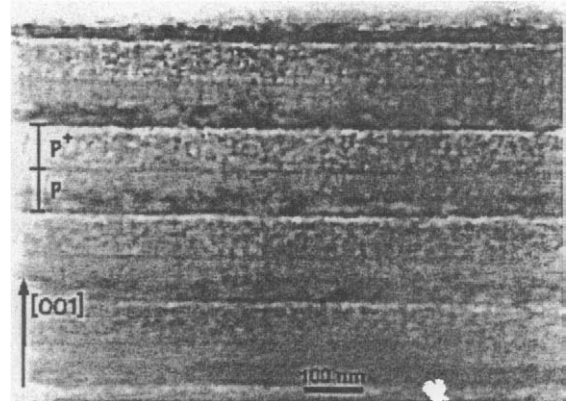


Fig. 56. Transmission electron microscopy cross section of a porosity multilayer obtained on a periodically doped substrate. Reprinted with permission after Ref. [202].

of the anisotropy of the etch caused by the etching selectivity on the doping level [200].

## 5.2. Bragg Reflectors

Some examples of reflectivity curves for PS-based distributed Bragg reflectors are reported in Figures 57 and 58.

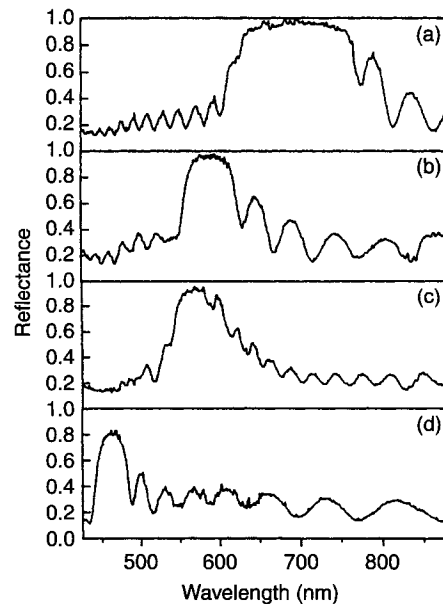


Fig. 57. Normal incidence reflectance spectra of various DBR at room temperature: (a) DBR centered at wavelength  $\lambda = 670 \text{ nm}$  and made by 15 repetitions of two layers of 62 and 75% porosity, respectively; (b) DBR centered at  $\lambda = 590 \text{ nm}$  and made by 15 repetitions of 62 and 75% porosity layers; (c) DBR with the same structure as that of panel (b) but with a larger number of repetitions, 30; (d) DBR centered at  $\lambda = 465 \text{ nm}$  and made by 15 repetitions of 62 and 75% porosity layers. Reprinted with permission after Ref. [198].

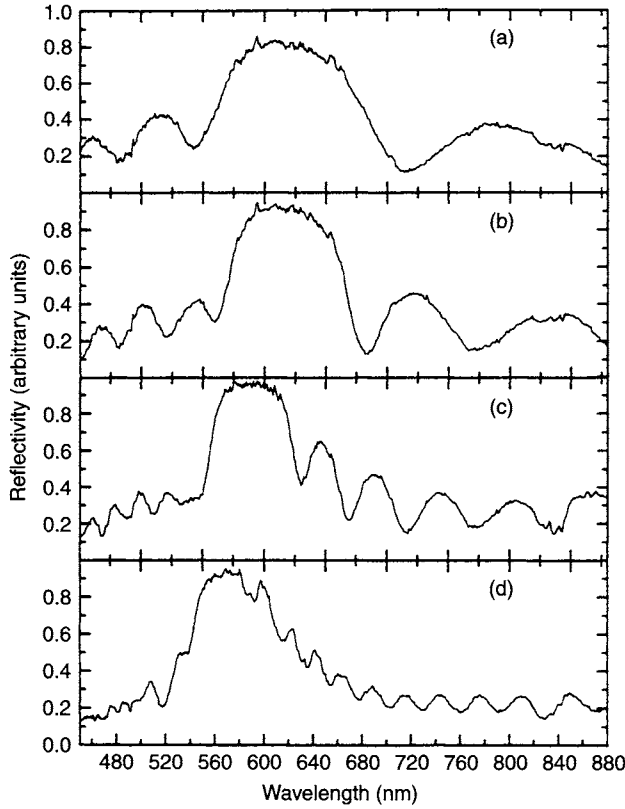


Fig. 58. Normal incidence reflectance spectra of various DBRs at room temperature. The DBR differ only in the number of periods. All are centered at  $\lambda = 590$  nm and made by different repetitions (5 (a), 8 (b), 15 (c), 30 (d)) of 62 and 75% porosity layers. Reprinted with permission after Ref. [2].

The effect of the variation of  $\lambda_c$ , the central wavelength of the DBR, is shown in Figure 57 [198]. The reflectance maximum increases from 0.8 to 0.95–0.97 when increasing  $\lambda$ . The best results are reached for DBRs centered at long wavelengths (i.e., in the near infrared). This is due to an increased absorbance of the PS layers at shorter wavelength (i.e., lower than 550–600 nm), an effect that was not taken into account in the first modelization of the structure. The width of the high reflectance region (namely, the stop-band region) is determined by the refractive index difference between the high refractive index ( $n_H$ ) layer (H) and the low refractive index ( $n_L$ ) layer (L). Higher is the difference and larger is the width. An example is also shown in Figure 57, where the ratio at  $\lambda$  of the refractive indexes changes from 1.19 (d) to 1.27 (b) and to 1.52 (a). Also, in agreement with the theory, the value of the reflectance in the stop band increases as the refractive indexes ratio increases [181].

The number of periodic repetitions of the LH (where, as usual, L stands for low refractive index layer and H for high refractive index layer) stacks in the DBR should be optimized with respect to the beneficial effect of an

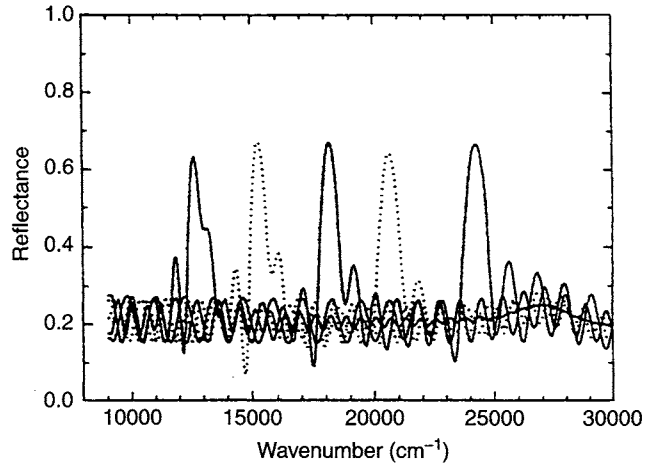


Fig. 59. Reflectance spectra of various DBRs that after formation were thermally oxidized in dry  $O_2$  at  $950^\circ C$  for 5 min. Reprinted with permission after Ref. [197].

increased reflectance, for a large number of repetitions, and the detrimental effects of a depth inhomogeneity in the porosity for the first layers because of the effect of a long residence in the electrolyte [193]. This is clearly shown in Figure 58, where only the repetition number of periods is changed. The maximum reflectivity is increasing from 0.8 for 5 periods (a) to 0.93 for 8 periods (b), to 0.97 for 15 periods (c) to 0.95 for 30 periods (d). A good compromise is reached for a number of repetitions of about 15. Also, the reflectance of the side bands decreases, increasing the number of periods, in agreement with the theoretical expectation value [181].

Figure 59 shows the reflectance of several oxidized DBRs over the visible range [197]. No absorption effect is measured (in the sense that the reflectivity maximum is the same for all the layers). This is due to the use of a complete oxidation of all the PS layers, which diminishes the absorption in the visible. Oxidation is accomplished after 5 min thermal processing (namely, rapid thermal oxidation (RTO)) at  $950^\circ C$ . The stop band is narrower and the reflectivity maxima are lower than in non oxidized samples because of the lower refractive index of  $SiO_2$  (the oxide that forms in the RTO process) with respect to that of Si, which decreases the absolute value of the ratio  $n_H/n_L$ .

### 5.3. Random Bragg Reflectors

Crystalline disorder modifies the band structure of electronic systems. In particular, amorphous Si has a wider energy gap than crystalline Si. By considering the analogy between electronic states and photon modes, one can expect that a randomization of the DBR structure (in the sense of its internal periodical order) will modify its reflectance spectrum. Random Bragg reflectors have

been obtained [3] by keeping constant the thickness ( $d_L$ ) and the porosity of the L layers and by changing the thicknesses ( $d_H^L$ ) but not the porosity of the H layers. The various  $d_H^L$  were generated randomly such that their histogram tends for large numbers to a Gaussian distribution centered around a mean value  $\langle d_H \rangle$  and with a standard deviation  $\sigma$ . Clearly  $\langle d_H \rangle \times n_H = d_L \times n_L = \lambda/4$ .

Figure 60 shows the effect of an increasing  $\sigma$  on the reflectance spectra of random DBRs centered at the same  $\lambda = 800$  nm. For  $\sigma = 0$ , the typical reflectance of a DBR is observed. The stop band is 200 nm wide and the maximum reflectivity is  $\approx 95\%$ . The effect of increasing  $\sigma$  is to broaden the stop band without a diminution of the absolute value of the reflectivity. For  $\sigma = 30$  nm, the stop band starts at about 650 nm and extends to more than 900 nm, the upper limit of the detection of the experimental set-up used.

Figure 61 shows the influence on the reflectance spectra of the  $d_H^L$  distribution in the actual sequence used in

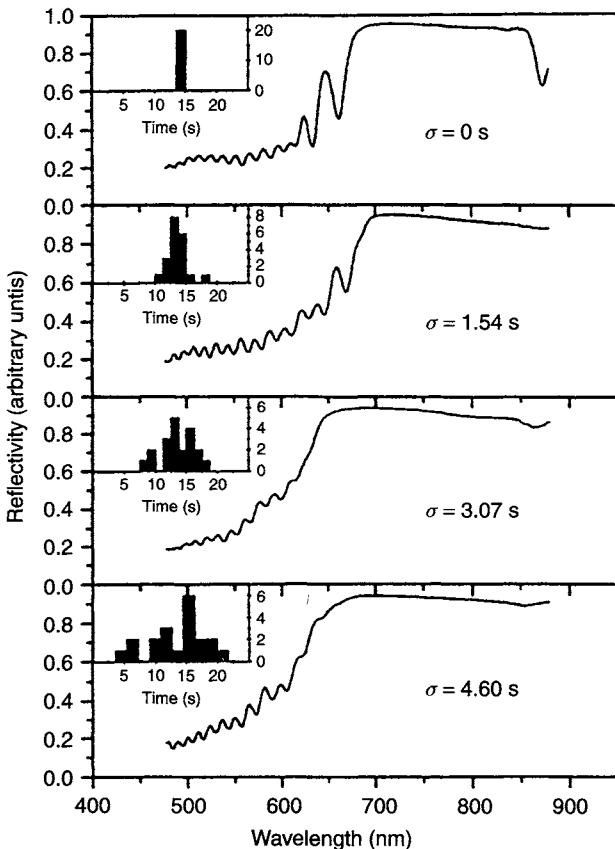


Fig. 60. Room-temperature reflectance spectra of random DBRs centered at  $\lambda = 800$  nm. The insets show the histogram of the times used to etch the various low porosity layers that form the DBR. The different spectra correspond to different standard deviations  $\sigma$  of the Gaussian distribution according to which the times are dispersed. Reprinted with permission after Ref. [3].

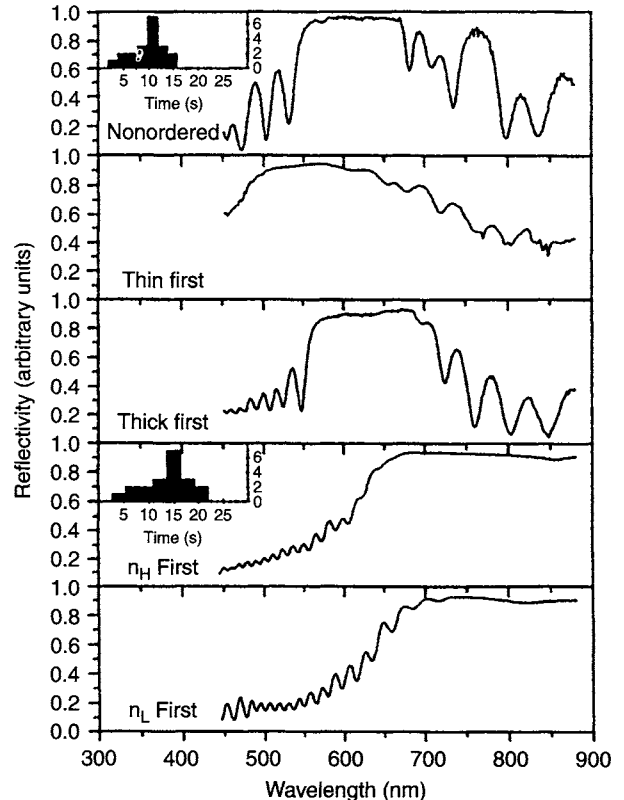


Fig. 61. Room-temperature reflectance spectra of random DBRs centered at  $\lambda = 570$  nm (first three spectra starting from the top) and at  $\lambda = 800$  nm (last two spectra). The insets show the histogram of the times used to etch the various low porosity layers. The first three spectra correspond to different orderings of the same layer distribution: random ordering (top spectrum), increasing thickness ordering (second spectrum), and decreasing thickness ordering (third spectrum). The other two spectra correspond to an increasing thickness sequence (which is different from the one used in the first three spectra) where the first layer on the air side was a high refractive index layer (fourth spectrum) or a low refractive index layer (fifth spectrum). Reprinted with permission after Ref. [3].

forming the DBR [3]. All the samples have the same layer sequence. The top panel reports the spectra when the layer thicknesses are randomly settled. The second and third panels refer to the case of an ordered sequence of the layer thicknesses: the second to the case of an increasing ordering (the thinnest layer is the first on the air side) and the third to the decreasing ordering (the thickest one is the first on the air side). These three Bragg reflectors are centered at the same  $\lambda = 570$  nm; that is, the Gaussian distribution of the H thickness is centered at  $\langle d_H \rangle = 63.8$  nm, with  $\sigma = 21$  nm, and has the same random distribution. The principle of operation of a  $\lambda/4$  stack is such that a period HL corresponds to an  $m \times \pi$  phase difference between rays reflected by neighboring layers, where  $m$  is an integer. The presence of different thicknesses enlarges the  $\lambda$  values for which constructive interference occurs (stop band). This explains the effect of

the ordering. However, when a thin layer, which yields a constructive interference condition for short wavelengths, occurs at the end of the sequence, that is, some 10  $\mu\text{m}$  away from the surface, most of the light of that wavelength already has been absorbed by the other layers. This explains why, to observe reflection at short wavelengths in a random DBR, the thinnest layer has to be placed on the air side.

The last two reflectance spectra in Figure 61 refer to the following HL ordering: the fourth panel refers to the sequence air–HLHL... ( $\times 20$ )...HLHL–substrate; the bottom panel refers to air–LHLH... ( $\times 20$ )...LHLH–substrate. The stop band is almost equal in the two cases, whereas the reflectance maximum is higher when a high refractive index layer directly faces the air than when the low refractive index layer is used: 95 to 93%. This could be explained by the larger refractive index mismatch at the air side in the first case than in the second.

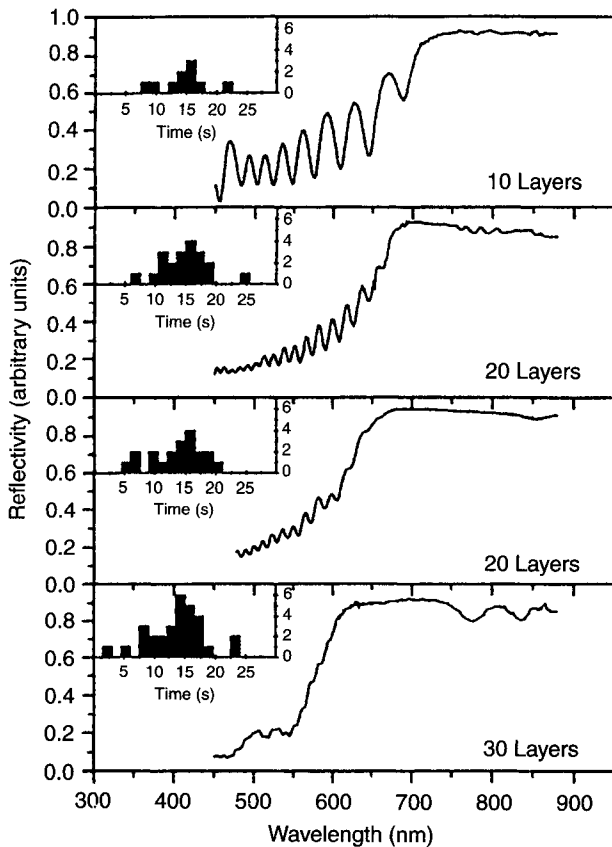


Fig. 62. Room-temperature reflectance spectra of random DBRs centered at  $\lambda = 800$  nm for various numbers of random layers (i.e., periods) indicated. The insets show the histogram of the times used to etch the various low porosity layers. For the case of 20 layers, 2 different DBR with different random sequences are presented. Reprinted with permission after Ref. [3].

Figure 62 shows the effect of increasing the number of periods in the DBR [3]. Even with 10 random layers, that is, 10 HL periods, a good disorder description is reached (compare with the reflectance of the periodic DBR shown in Figure 60, top spectrum). Moreover, by increasing the number of layers the random distribution better approximates a Gaussian (i.e., is “more random”) and the stop band broadens. The maximum number of periods used was 30 layers. The reflectance of the corresponding DBR is shown in the bottom panel of Figure 62. A degradation of the characteristics of this DBR is observed with a lower reflectance maximum and the appearance of reflectance minima in the stop band. This last effect has been observed already for “normal” Bragg reflectors and discussed previously.

It is worth observing that the properties of the random DBR are not very dependent on the actual distribution of the thicknesses used. In fact, as can be observed in the second and third panels of Figure 62, the use of two different choices of random thicknesses does not change the reflectance spectrum. Only some minor differences can be observed and explained by the particular thicknesses used in the DBR growth. For example, the DBR whose reflectivity is reported in the second panel has a lower number of thin layers than the DBR whose reflectivity is reported in the third panel. Hence, the reflectance of the first DBR shows a stop band that starts at a longer wavelength than that of the second DBR.

#### 5.4. Fabry-Perot Filters

Some examples of PS–FP filters are reported in Figure 63 [198]. These consist of a  $\lambda/2$  thick central layer sandwiched between two equal DBRs with six or eight repetitions of the  $\lambda/4$  thick LH stacks: the structure is the same as in the case of the microcavity. The only difference is the porosity of the central layer; in the PS–FP it is the same as one of the layers employed to grow the Bragg reflectors, whereas in the PSM the central layer has a porosity (and then a refractive index) different from both the porosities of the alternated layers constituting the DBR. Decreasing the number of repetitions from eight to six does not influence markedly the reflectance of the stop bands, whereas it increases the transmittance in the FP mode (see Table VIII).

The filtering effect of these FP filters on the emission band of PS has been demonstrated and is shown in Figure 64 [198]. A comparison between the room-temperature photoluminescence spectra of a 5  $\mu\text{m}$ -thick 75% porosity PS sample and those of samples constituted by a FP filter on top of a thick (a few micro meters) 75% porosity PS layer has been performed. The wide emission band of PS is strongly narrowed by the action of the FP filter. In addition, by tuning the FP wavelength

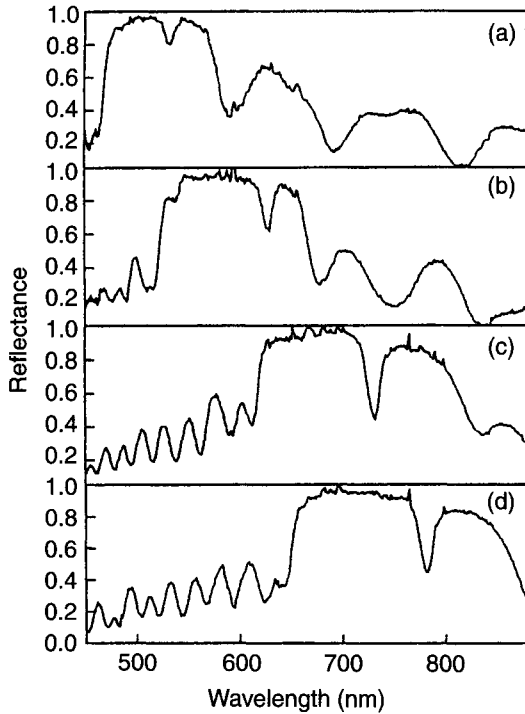


Fig. 63. Room-temperature normal incidence reflectance spectra of various FP filters whose characteristics are reported in Table VIII. All the FP filters have a symmetric structure made by two DBRs separated by a  $\lambda/2$ -thick central layer of 75% porosity.  $\lambda$  is the wavelength of the FP transmittance wavelength. (a) FP with  $\lambda = 533$  nm and with DBR formed by eight repetitions of two  $\lambda/4$ -thick layers of 62 and 75% porosity, respectively; (b) FP with  $\lambda = 629$  nm and with DBR formed by eight repetitions of 62 and 75% porosity  $\lambda/4$  layers; (c) FP with  $\lambda = 731$  nm and with DBR formed by six repetitions of 62 and 75% porosity  $\lambda/4$  layers; (d) FP with  $\lambda = 782$  nm and with DBR formed by six repetitions of 62 and 75% porosity  $\lambda/4$  layers. Reprinted with permission after Ref. [198].

Table VIII Parameters for the Various Fabry–Perot Filters Shown in Figure 63.  $\lambda$  Is the FP Wavelength,  $\Delta\lambda$  the Width of the Transmittance Peak, and  $T_{\max}$  Its Value;  $n_H/n_L$  Is the Ratio between the Refractive Indexes of the Low and High Porosity Layers in the Bragg Reflectors Whose Number of Repetitions is Indicated in the Last Column

Sample	$\lambda$ (nm)	$\Delta\lambda$ (nm)	Finesse	$T_{\max}$	$n_H/n_L$	# repetitions
902	533	13	41	0.20	1.7	8
904	629	16	45	0.37	1.60	8
908	731	16	45	0.56	1.50	6
906	782	18	46	0.55	1.43	6

Source: Adapted from [2].

$\lambda$ , it is possible to select the emission wavelength of the structure. This is the basis for the subsequent work on the PSM.

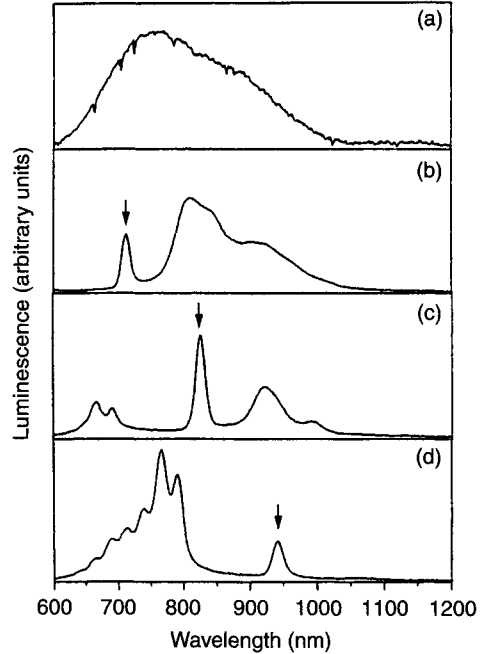


Fig. 64. Room-temperature normal incidence PL spectra of PS samples: (a) 5- $\mu\text{m}$ -thick 75% porosity sample; (b) a sample constituted by FP centered at 710 nm on top of a 5- $\mu\text{m}$  thick 75% porous layer; the FP finesse is 46; (c) FP centered at 828 nm and with a finesse of 49 on top of a 2- $\mu\text{m}$ -thick 75% porous layer; (d) FP centered at 941 nm and with a finesse of 47 on top of a 2- $\mu\text{m}$ -thick 75% porous layer. The arrows indicate the FP  $\lambda$ . All the FP have the same structure, formed by two equal DBR separated by a  $\lambda/2$ -thick and 53% porosity central layer. The DBR are made by six repetitions of two  $\lambda/4$ -thick layers of 53 and 75% porosity, respectively. The FP finesse has been determined by independent reflectance measurements. Reprinted with permission after Ref. [198].

## 5.5. Random Fabry-Perot Filters

Figure 65 shows the effects of the use of random DBRs in the previously described FP structure [3]. These filters have the following sequence: air–LH...( $\times 6$ )...LH– $\underline{S}$ –HL...( $\times 6$ )...HL–substrate, where  $\underline{S}$  is the central layer of thickness  $\lambda$ . The distribution of the random layers in the two DBRs is symmetric around the  $\underline{S}$  layer. The various spectra correspond to various levels of randomness governed by the standard deviation of the Gaussian distribution  $\sigma$  of thicknesses already described. The top reflectance shows the typical characteristic shape of a FP filter. The effect of the use of random DBR is to slightly decrease the transmittivity at the wavelength of the FP mode that passes from 46% to 44% for the random FP, whereas the stop band increases from 184 to 192 nm in the random FP, but such small effects could be also attributed to uncontrolled variations in the production parameters.

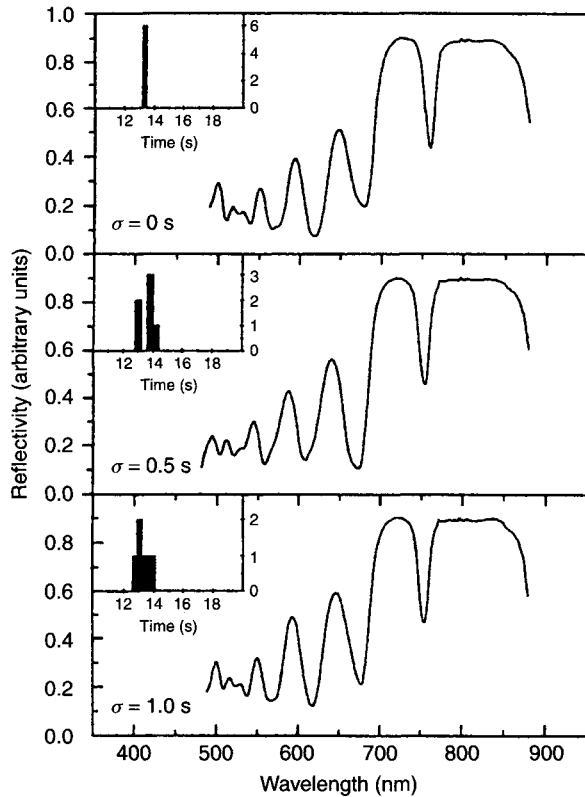


Fig. 65. Room-temperature reflectance of FP filters formed by using random DBR: (inset) histogram of the times used to etch the various low porosity layers in the two DBR. Reprinted with permission after Ref. [3].

Figure 66 shows the luminescence spectra of various random FP [3]. By measuring the luminescence one measures principally the transmittivity of the FP filter [203]. The top panel in Figure 66 demonstrates the relative insensitivity to the actual set of random numbers used for the random FP properties. The central panel shows the effect of increasing  $\sigma$  on the luminescence linewidth around the FP resonance, which is an indication of the finesse of the FP filter. The linewidth decreases significantly by increasing the degree of randomness into the DBR. In addition, the baseline is also reduced and this fact points to a slightly large reflectance for the random DBR. The bottom panel compares different random FP filters obtained by increasing the number of the periods. It has been found that the linewidth is reduced from 25 nm for 4 periods to 2 nm for 10 periods.

The record linewidth is shown in Figure 67 [3]. A photoluminescence linewidth value as narrow as 2 nm can be measured. This should be compared with 130 nm, the typical linewidth of the luminescence band of PS of characteristics similar to those measured here. For this random FP filter a finesse as high as 200 is obtained. Note also the nearly complete absence of luminescence for wavelengths different from the resonant wavelength.

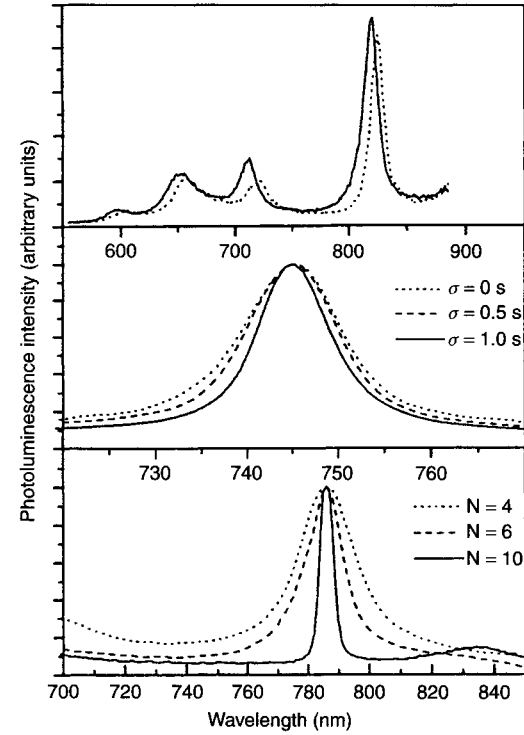


Fig. 66. Room-temperature luminescence spectra of various random FP filters: (top) two samples equal except for the actual random number sequence; (center) luminescence of the same three samples whose reflectance is shown in Figure 65; (bottom) luminescence of three samples for increasing number of periods ( $N$ ) in the DBR. The luminescence spectra are horizontally shifted by small amounts (less than 10 nm) allow to the wavelength of the maximum to coincide. The various luminescence spectra are normalized to their maximum and have intensities that are not comparable among them except for those of the top panel. Reprinted with permission after Ref. [3].

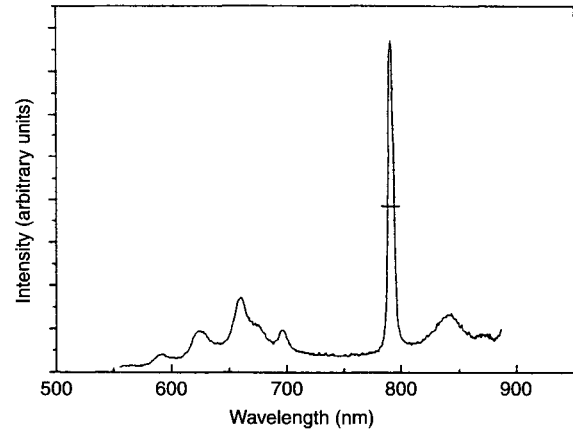


Fig. 67. Room-temperature luminescence spectrum of a random FP filter. Reprinted with permission after Ref. [3].

A different approach to random FP filters is that of the Rugate filters [197]. Rugate filters are obtained by a continuous variation of the refractive index with depth

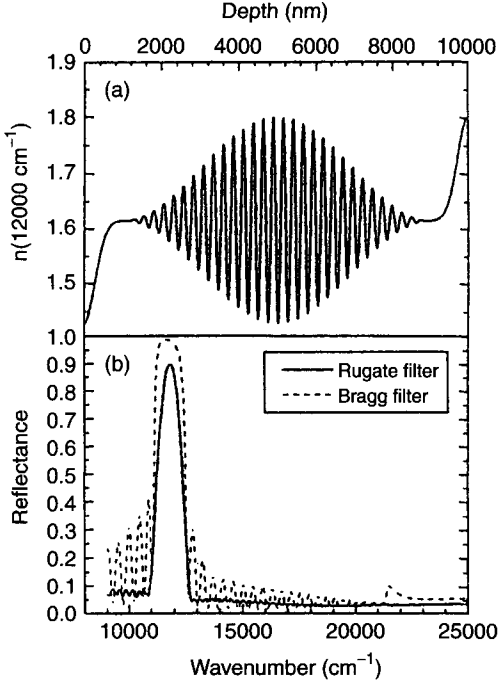


Fig. 68. Depth profile of the refractive index (a) and the reflectance spectrum (b) of a Rugate filter formed on a *p*-type doped substrate. For comparison the reflectance spectrum of a DBR is shown. Reprinted with permission after Ref. [197].

and allow us to obtain reflectance profiles with very low sidebands. A sinusoidal profile of the refractive index is usually employed [204]. A careful characterization of the  $n$  versus- $J$  relationship is clearly necessary. In this way it is then possible to modulate the refractive index value with depth in the way shown in Figure 68a. As a result, the reflectance shown in Figure 68b is obtained. As expected, the sidebands are practically absent.

## 6. POROUS SILICON MICROCAVITIES

A planar optical microcavity can be realized by using a FP structure surrounding the central PS layer. In this way an all-PS microcavity is obtained. The top and bottom DBRs act as photon confiners, whereas the central layer (also named the spacer) acts as the optically active medium. It is in this layer that the coupling of the excitonic transitions with the photon modes should be modified (inhibited or enhanced). It is worth underlining an important difference between III and V microcavities such as those reviewed in [185] and PSMs: the first have the emission line of the active layer in itself (without the cavity effects) that is narrower than the FP transmission peak, in PSMs the emission of “bulk” PS is much wider than the reflectivity FP dip. This point makes PSMs more interesting the

because they allow testing of a new situation in the field of microcavities.

PSMs differ in some fundamental aspects from similar optical microcavities realized with GaAs and AlGaAs multilayers [185]. In fact, in PSMs:

- the coupling between the photon mode and the exciton mode is weak mainly because of the very broad emission band of PS and the fact that the DBRs do not confine perfectly the light but they are partially penetrated by the confined photon mode;
- the emission takes place in the whole central layer;
- the emission band of PS is wider than the stop band of the DBR;
- the emission of the central PS layer and of the PS-based DBR overlap spectrally.

Two different kinds of PSM have been reported in the literature. One is based on the use of PS to fabricate the whole PSM [187, 205]. The other uses a mixed approach: the bottom mirror is a PS-DBR whereas the top mirror is a thin metal (e.g., gold) layer [206]. In the following, we review mainly the properties of all PS microcavities.

### 6.1. Physical Properties

Figure 69 [199] shows the room-temperature PL spectra of a PSM with resonance at  $\lambda_c$  (solid line), of a  $\lambda_c$ -thick PS 75% porosity reference layer (dotted line), and of a reference DBR composed of 12 periods of alternating 62

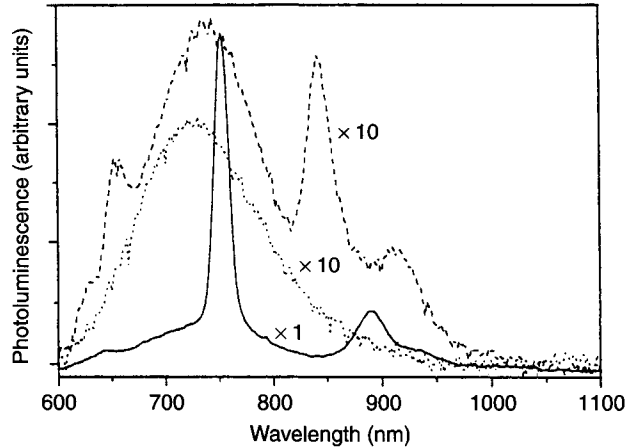


Fig. 69. Room-temperature PL spectra of a  $\lambda$ -thick PSM (solid line), of a  $\lambda$ -thick porous silicon reference layer (dotted line), and of a sample composed of 12 periods of  $\lambda/4$ -thick porous silicon layers with alternating porosities of 62 and 45% (dashed line). The PL spectra were collected along the axis normal to the sample surface. To compare the various PL lineshapes the emission of the Bragg reflector and of the reference sample has been multiplied by a factor of 10. Reprinted with permission after Ref. [199].

and 45% porosity layers (dashed line) [199]. The emission was collected around a the direction normal to the sample surface. The influence of the change in the photon mode density on the spontaneous emission spectrum can be appreciated by comparing the lineshape of the PSM with that of the reference PS. For  $\lambda \simeq \lambda_c \simeq 750$  nm, a sharp peak is observed that is 14 times more intense than the luminescence (this value can go up to 20) at the same  $\lambda_c$ , for the reference sample. For  $\lambda \neq 750$  nm but within the stop band of the DBR, the luminescence of the PSM is approximately the same as that of the reference mirror. For  $\lambda \simeq 900$  nm, a secondary peak is observed because of the escape of a leaky waveguide mode confined in the waveguide-like structure formed in the plane between the mirrors of the microcavity [207]. These leaky waveguide modes can be strongly enhanced by a suitable choice of the PSM parameters (see, e.g., Fig. 64). The overall integrated emission intensity of the PSM is increased by a factor of 4 with respect to that of the reference. The microcavity has an important role in this former intensity increase but another beneficial effect is expected by the top Bragg reflector, which acts as a protective layer for the active optical layer. A reduction of the surface recombination velocity and of the effect of atmosphere impregnation can be expected. In addition, by simply choosing the appropriate width of the PSM active layer and DBR it is possible to select the emission wavelength of the PSM taking advantage of the broad spectral emission of the PS active layer (see Fig. 64). Concerning the PL of the DBR (dashed line), although it is centered on the same spectral region as the standard PS  $\lambda$ -thick layer (dotted line), it cannot give rise to both the narrowing and the enhancement observed for the PSM emission. The shape of the PL of the DBR is linked to the stop-band reflectivity spectrum that rules the reflectivity properties of the reflector itself [2].

An important aspect of the optical emission tests on the possibility of controlling the radiation pattern and obtaining a strong angular confinement of the output emission. In the case of semiconductor microcavities, this is a well-known result related to the anisotropic density of photon states controlling the emission radiative decay [185, 208].

In addition, emission at angles far from the normal experiences a further decrease in the coupling between the excitons and the cavity mode because of the shift of the cavity-mode resonance wavelength [209].

This effect is observed in the dependence of the PL intensity as a function of the emission angle  $\phi$  (see the definition in Fig. 70) [199]. These results are shown in Figures 71 and 72. In Figure 71, two main effects can be observed [2]:

- the shift of the resonance peak with  $\phi$  (see Eq. (39));
- the decrease of its intensity.

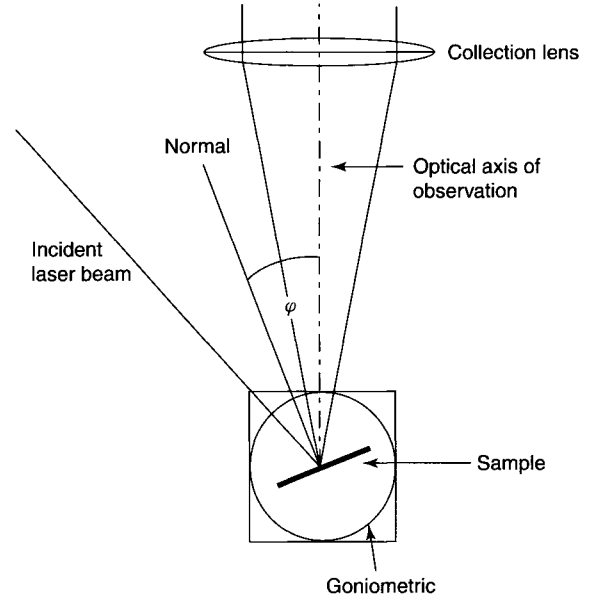


Fig. 70. Experimental arrangement for the collection of the PSM luminescence. Reprinted with permission after Ref. [2].

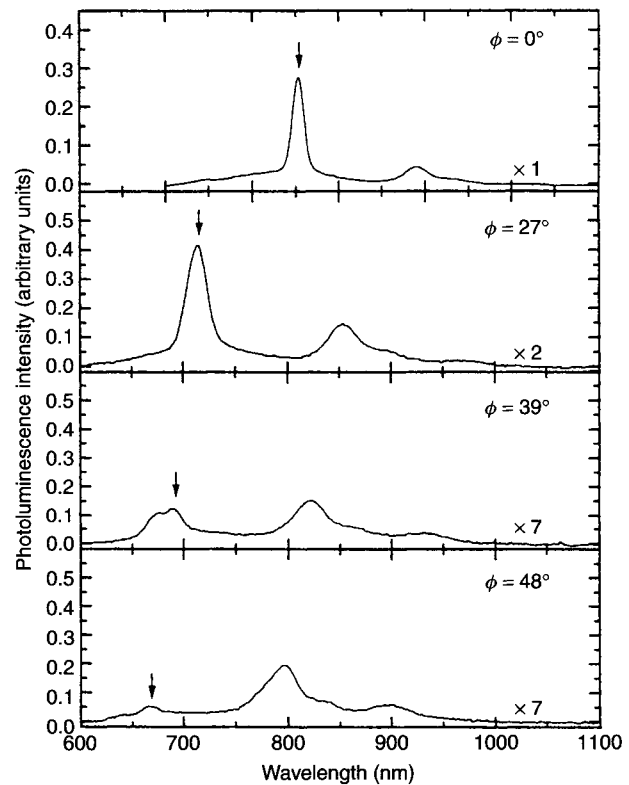


Fig. 71. Room-temperature luminescence spectra of the  $\lambda$ -thick PSM as a function of the observation angle. The sensitivity factors are reported. Reprinted with permission after Ref. [2].

This is well quantified in Figure 72 where the  $\phi$  dependence of the resonance peak intensity is reported [199]. A very similar result is obtained if one plots the total

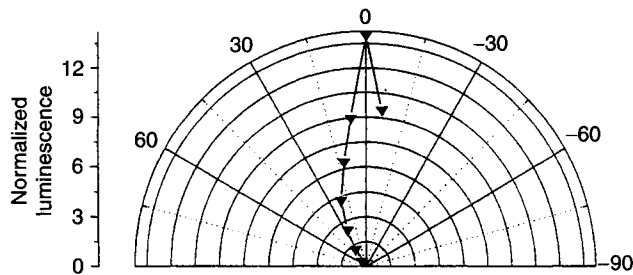


Fig. 72. Room-temperature radiation pattern corresponding to the  $\lambda$ -thick PSM. The reported values were obtained normalizing the observed intensities to the corresponding excitation intensities and the PL intensities of the  $\lambda$ -thick porous silicon reference layer. Reprinted with permission after Ref. [199].

PL intensity as a function of  $\phi$ . As a result, the emission intensity of the PSM is concentrated in a cone of about  $30^\circ$  around the normal. The effect observed in Figure 72 is due to the anisotropic photon mode density resulting from the confinement in the microcavity.

Figure 73 shows the PL emission spectra at 30 K and at room temperature for both a  $\lambda$  (solid lines) and a  $\lambda/2$  (dotted lines) microcavity [203]. The inset

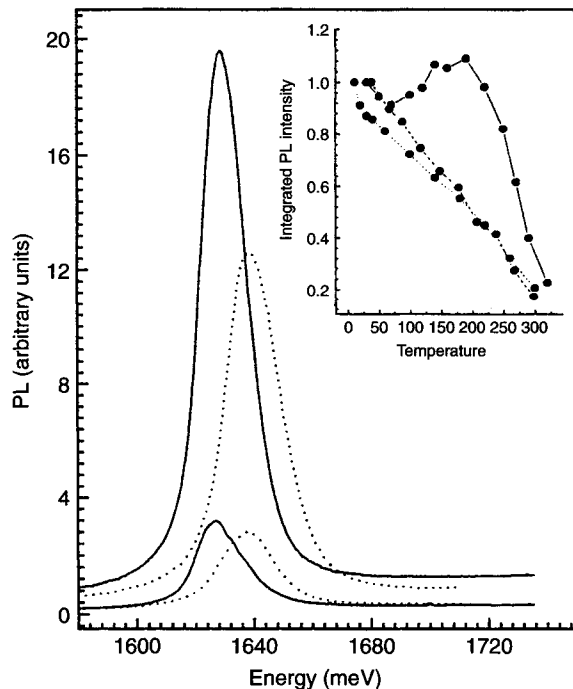


Fig. 73. Photoluminescence spectra of the  $\lambda$  (solid lines) and  $\lambda/2$  (dotted lines) PSMs at 30 K and at room temperature (the stronger emissions correspond to 30 K). The inset shows the temperature dependence of the PL integrated emission of the  $\lambda$  (dashed line) and  $\lambda/2$  (dotted line) microcavities and of a reference PS  $\lambda$ -thick sample (solid line) normalized to the corresponding lowest temperature PL integrated spectra. Reprinted with permission after Ref. [203].

shows the temperature dependence of the normalized integrated emission intensity of both microcavities and, as a reference, that corresponding to the PS  $\lambda$ -thick layer. A small red shift (as few milli-electron-volts) of the PL peak is observed as the temperature increases owing to variations in the refractive indexes and layer thickness. No significant dependence of the FWHM on the temperature can be revealed, confirming that the linewidth is determined only by the microcavity finesse. The stronger emission of the  $\lambda$ -PSM is related to the larger active layer thickness, although the normalized integrated emissions of the two microcavities become equal with increasing the temperature, as the hopping-mediated and thermally activated non-radiative processes [17] compensate for the thicker active layer of the  $\lambda$ -cavity.

Microcavity effects are also revealed by the temperature dependence of the integrated PL intensity (inset of Fig. 73). A sensibly different behavior between PS and PSMs is observed. In the reference sample, as in the usual PS samples [210], the integrated PL emission behavior is explained with the help of concurrent measurements of the PL lifetime and it is thought to be the result of two opposite processes [173]: thermally activated promotion of excitons from the low-energy dipole-prohibited exciton triplet state to the high-energy dipole-allowed exciton singlet state, which increases the PL intensity and dominates at low temperatures, and the thermally activated nonradiative recombination, which decreases the PL intensity and dominates at higher temperatures. These trends are strongly modified by the presence of the cavity embedded in the PS. The temperature dependence of the PL intensity of PSMs has been investigated in detail in [211] and is presented in more detail in Section 6.5, where a tentative explanation of the observed effects is proposed.

The results presented so far have been obtained with PSMs formed on heavily doped substrates. However, low-doped substrates yield PS with higher luminescence efficiency. Thus it is interesting to know whether improvement in the spontaneous emission properties is found also in PSMs formed on low doped substrates. This work has been performed in [205, 212]. That characterization has shown that in the case of  $p^-$  substrates (6–9  $\Omega$  cm typically) the etching rate is generally slower ( $3\text{--}35\text{ nm s}^{-1}$ ) and it is very hard to get low porosity values. Using a solution of 20% HF in water and ethanol, it was possible to obtain porosities in the range 60–85%, which correspond to refractive index values between 1.7 and 1.3 at 750 nm (see Fig. 27 [212]).

As remarked previously, working with multilayers instead of single layers has an important advantage for the mechanical stability. It is extremely difficult to obtain high porosity layers (the most luminescent) of considerable thickness. Alternating low and high porosity layers allows production of thick multilayers, making

the whole structure more robust, while the emission efficiency is not reduced and can be, on the contrary, further improved by careful design of the cavity [2]. This is even more important for  $p^-$  doped substrates, where the highest porosity single layers do not have the necessary mechanical stability to ensure the high optical quality required for reliable and precise measurements. In multilayer structures these highly porous layers are sandwiched between layers of lower porosity, and their optical properties turn out to be more homogeneous and reproducible. Nevertheless, the drying process, which is a very important step for obtaining porosity layers, has been shown to be critical also for multilayers structures. Concerning their performance, PSMs have been obtained with linewidth of 6 nm [212], finesse up to 66, external quantum efficiency of about 15% and luminescence enhancement of  $\simeq 20$  [205].

## 6.2. Aging Effects in Porous Silicon Microcavities

Aging effects in PSMs are related to the changes in PS itself. They involve variations in the luminescence intensity and variations caused by changes in the refractive index. Both effects are closely related to oxidation.

For PS, the oxidation increases the luminescence quantum efficiency. The large increase in emission intensity is accompanied by a blueshift of the maximum of the broad emission band. For this reason, it is interesting to know how this enhancement of the emission intensity depends on time and to what extent it is preserved in the case of PSM.

To understand the role played by single optical parameters in the time evolution of PSMs, the variation of the refractive index has been investigated for some reference layers over a period of six months. These variations are reported in Figure 27 [212]. It should be noted that for every value of the anodization current density (i.e., for every value of the porosity), the value of the refractive index decreases with time. This is not so surprising, because after partial oxidation, PS is no longer a mixture of air and silicon, but a mixture of air, silicon, and silicon dioxide, and the refractive index of silicon dioxide, about 1.46 in the red region of the spectrum, is much lower than that of silicon. The oxidation process itself seems to be more efficient in the high porosity layers because of the larger internal surface and the lower content of silicon. As a consequence, the relative variation of the refractive index is larger for the higher porosity layers. All these properties of PS single layers are extremely important to understanding the evolution of PSM optical properties with time.

The changes in the PL intensity and lineshape for a typical  $p^-$  PSM over a period of six months are reported in Figure 74. It is worth noticing how the whole structure

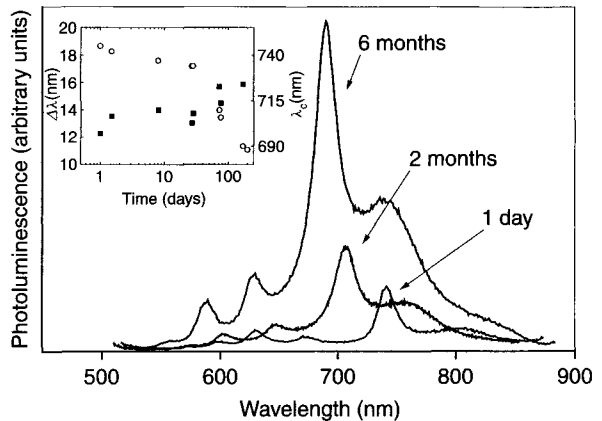


Fig. 74. Evolution of the PL spectrum over a period of six months for a  $p^-$  PSM with six periods for each mirror. The central peak slightly broadens, while the rise in intensity is more than one order of magnitude. The inset shows  $\Delta\lambda$  (filled square) and the central wavelength ( $\lambda_c$ , open circle) as a function of time for the same PSM. Reprinted with permission after Ref. [212].

of the cavity is not degraded, but simply shifted toward higher energies, while the emission intensity increases about one order of magnitude. The conservation of the cavity structure is even more apparent if we compare the reflectivity spectrum of the freshly etched PSM with the spectrum measured after six months [212]. Both spectra are reported in Figure 75. The central dip coincides with  $\lambda_c$ , and it undergoes a relevant blueshift. The maximum of the reflectivity is lowered only a few percent, while the whole stop band shifts about 50 nm, retaining its own features. The observed blueshift is caused by the refractive index changes in the PS layers of both the central cavity and the mirrors. As the value of  $n_c$  lowers with time,  $\lambda_c$  moves toward higher energies, as

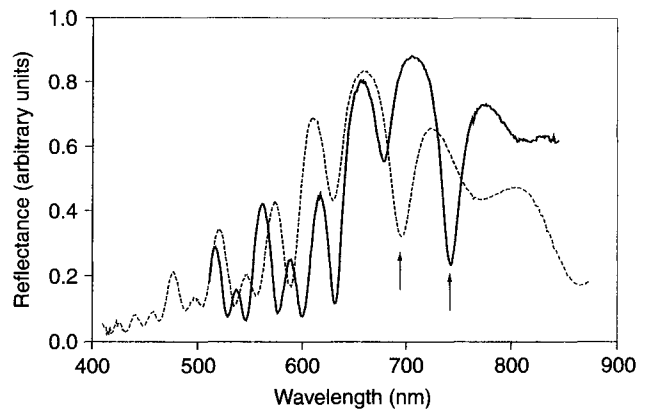


Fig. 75. Reflectivity spectra of the same PSM shown in Figure 74: (solid line) freshly etched; (dashed line) six months old. The arrows indicate the cavity wavelength. The PSM spectrum maintains its original features, but shifts to higher energies. Reprinted with permission after Ref. [212].

reported in Figure 75, but maintains its central position within the stop band of the PSM because the mirrors also oxidize [212]. The stop band of the mirrors shifts to higher energies because the refractive indexes of the PS layers decrease.

Because all the refractive indexes lower with time, approaching the value of 1, one can expect the stop-band to become narrower and narrower as the PSM ages. However, this has not been observed. As we have shown in Figure 27, the lower the refractive index, the larger the relative change with aging.

Nevertheless, the whole process is not ideal, and the degradation in the quality of the PSM is then observed [212]. As can be seen in Figure 74, the enhancement of the emission intensity is accompanied by a slow decrease of the ratio of central wavelength luminescence to background emission and by an increase of the intensity of the side bands. This slow degradation affects the  $\Delta\lambda$  of the central peak, which enlarges slightly with time. In Figure 76, we compare the PL of a freshly prepared PSM and an aged PSM with that of a reference layer of the same thickness and porosity as the cavity layer, which aged in the same way as the PSM. The relative enhancement in the emission remains approximately the same, while the whole increase of the PL intensity related to aging is more than one order of magnitude and occurs both for PS and the PSM.

We also performed simulations to obtain some insight on the aging process mechanism. We found that, whereas the blueshift in the whole structure of the cavity is basically due to variation of the refractive indexes, the degradation in the quality of the PSM is not due to the oxidation process itself, but to the fact that this

process is not homogeneous in depth. A homogeneous oxidation does not degrade the cavity, but, on the contrary, improves its optical properties because the difference in the refractive indexes increases with oxidation. The slow degradation in the reflectance properties and the slight increase in  $\Delta\lambda_c$  can be reproduced assuming a variation of refractive indexes with depth, as reported in Figure 75 [212]. The layers that face the surface oxidize before the other layers. As observed for random PSMs [3], the progressive oxidation is important to maintaining coherence between the multiple reflections at the various interfaces. This explains the relatively good performances of aged PSMs. To confirm this idea, we measured the cavity blue shifts for PSMs aged in the same way but with different numbers of periods in the mirrors. We found that after six months the relative blueshift is 7.3% with 6 periods, 7.1% with 8 periods, and 3.0% with 10 periods. These values are always lower than those estimated using the values of refractive index for freshly etched PS and aged PS (10.5%; see Figure 75) [212]. As a result of the very high specific internal surface of PS, the layers forming the microcavity undergo a process dependent on the time of storage in air, which results in the formation of a native oxide layer on the inner pore surface. This in turn could change the refractive index of PS and, consequently, the reflectance spectrum of the PS multilayer.

A comparison between "as-prepared" and oxidized PS multilayers has been performed in [200]. FP filters were formed on  $0.2 \Omega \text{ cm}$   $p$  doped wafers. The oxidation was performed in dry  $O_2$  at  $300^\circ\text{C}$  for different times.

Finally key role in the aging is played by the substrate resistivity.  $p^+$  doped samples, as those shown in Figure 63 [198], presented a shift of only some nanometers after one year of aging.

### 6.3. Simulation of the Optical Properties of Porous Silicon Microcavities

To clarify the optical behavior of the PSM, the reflectivity and absorption spectra were calculated in [203, 213] using a transfer-matrix approach (see Section 3.2) and assuming the exciton quantum confinement in Si nanocrystals [172]. The first step is evaluation of the first-order susceptibility given by

$$\chi(\omega) = \int_0^\infty P(\omega_o) \bar{\chi}(\omega, \omega_o) d\omega_o,$$

where  $P(\omega_o)$  is the distribution of oscillators (excitons) as a function of frequency. The susceptibility of a single exciton  $\bar{\chi}(\omega, \omega_o)$ , is given by

$$\bar{\chi}(\omega, \omega_o) = \frac{f \omega_o^2}{\omega_o^2 - \omega^2 - i\Gamma\omega},$$

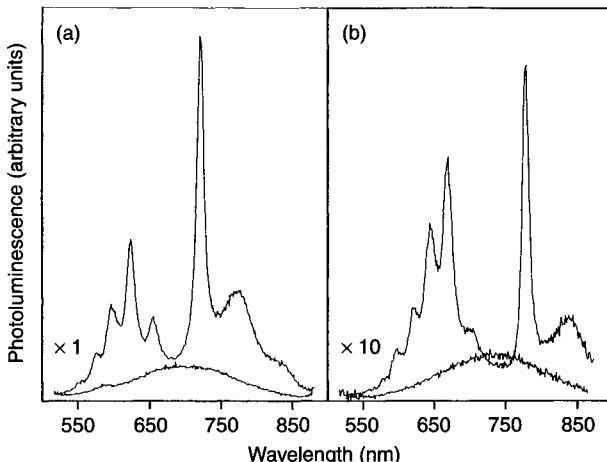


Fig. 76. Photoluminescence spectra of a typical PSM with eight periods for each mirror and a reference PS layer: (right) freshly etched PSM; the FWHM of the central peak is 9 nm; (left) the same PSM after six months. The FWHM is 10 nm (Gaussian fit). Reprinted with permission after Ref. [212].

where  $f$  is the oscillator strength, and  $\Gamma$  is the thermal broadening factor that is assumed to depend linearly on the temperature.

A Gaussian size distribution for the Si nanocrystals centered at  $d_c = 34.6 \text{ \AA}$  and having a width  $\sigma_d = 1.3 \text{ \AA}$  has been considered [172]. The emission energy  $E_i$  is then related to the corresponding size  $d_i$  through the power-law relation  $E_i = E_c(d_c/d_i)^n$  with  $n \approx 1.4$  [214], where  $E_c$  is the transition energy corresponding to a Si nanocrystal of size  $d_c$ . Within these assumptions  $P(\omega_o)$  is given by

$$P(\omega_o) \propto \frac{1}{\sigma_d} \frac{1}{\omega_o^{1+1/n}} \exp \left[ - \left( (d_c^2/2\sigma_d^2) \left( \frac{\omega_c}{\omega_o} \right)^{1/n} - 1 \right)^2 \right]$$

It is centered at  $\omega_c = E_c/\hbar$  and has a FWHM of 320 meV. The PS dielectric constant is then computed as  $\varepsilon = \varepsilon_b + 4\pi\chi(\omega)$ , where  $\varepsilon_b$  is the background dielectric constant of the layer.

The transfer matrix  $M$  for the whole PSM is then obtained by multiplying together the transfer matrices  $m$  of every single layer. For the  $j$ th layer

$$m_j = \begin{bmatrix} \cos \left( \frac{\omega}{c} n_j l_j \right) & -\frac{i}{n_j} \sin \left( \frac{\omega}{c} n_j l_j \right) \\ -in_j \sin \left( \frac{\omega}{c} n_j l_j \right) & \cos \left( \frac{\omega}{c} n_j l_j \right) \end{bmatrix} \quad (43)$$

where  $n_j = \sqrt{\varepsilon}$ ,  $l_j$  is the width of the  $j$ th layer, and  $c$  is the velocity of light.

From this, the reflectivity  $R = |r|^2$  and the transmittivity  $T = n_{\text{sub}}|t|^2$  are calculated, where  $n_{\text{sub}}$  is the index of refraction of the  $p$  doped silicon substrate, and  $r$  and  $t$  can be calculated using

$$\begin{aligned} r &= \frac{M_{12} + n_{\text{sub}}M_{22} - M_{11} - n_{\text{sub}}M_{12}}{M_{21} + n_{\text{sub}}M_{22} + M_{11} + n_{\text{sub}}M_{12}} t \\ &= \frac{2}{M_{11} + n_{\text{sub}}M_{12} + M_{21} + n_{\text{sub}}M_{22}} \end{aligned} \quad (44)$$

The absorption  $A$  is then calculated in the usual way as  $A = 1 - R - T$ .

The results are shown in Figure 77 [203]. The theoretical spectra exhibit the same behavior as the experimental spectra (Fig. 69 [199]). This result was expected in view of the nearly symmetric lineshapes of the PS luminescence spectra at low and room temperature. A broadening factor  $\Gamma$  for excitons pertaining to each single Si nanocrystal is included in the linear susceptibility to take into account the scattering and dephasing processes.

In [203], the detailed lineshape fitting procedure was not performed and the calculated spectra of Figure 77 have been obtained with  $\Gamma = 30 \text{ meV}$  and  $4\pi f = 1 \cdot 10^{-4}$ . The  $\Gamma$  value is not critical, and “reasonable” deviations from the reported values do not lead to strong modifications on the calculated spectra. The assumed value has

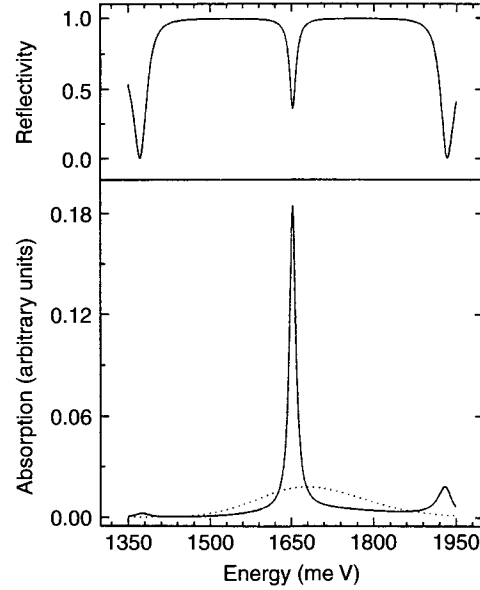


Fig. 77. Calculated reflectivity spectra (upper panel) and absorption spectra (lower panel) for a  $\lambda$  PSM. Also shown are the calculated absorption spectra (dotted line) for a  $\lambda$  PS layer without any reflectors. The best match with the experimental results (Fig. 73) has been obtained with a broadening factor  $\Gamma = 30 \text{ meV}$  and with an oscillator strength  $4\pi f = 1 \times 10^{-4}$ . Reprinted with permission after Ref. [203].

been chosen to be on the order of the thermal energy. For the  $f$  value, it was found that the stronger oscillator strengths result in a saturation of the absorption at the cavity resonance yielding a calculated reflectance spectrum that deviates significantly from the experimental one.

#### 6.4. Time-Resolved Spectroscopy in Porous Silicon Microcavities

To verify whether the increase of the spontaneous emission intensity is reflected in a decrease of the time decay of luminescence and then in an enhancement of spontaneous emission rate, time-resolved measurements have been carried out on PSMs [215]. Some characteristics of the samples studied are reported in Table IX. The evolution of the luminescence spectra with respect to the time delay from the excitation pulse is shown in Figure 78 [2]. The following facts are observed:

- the peak at  $\lambda_c = 730 \text{ nm}$  does not move as a function of the delay;
- the decay of the side-band luminescence is faster than that of the  $\lambda_c$  peak.

This last point is a surprising result. Because of the microcavity effect on the photon mode density  $G(\hbar\omega)$ , one

Table IX Growth Parameters and Reflectivity Data of the Various PS Microcavities

Name <sup>a</sup>	Slab order <sup>b</sup>	$n_H^c$	$n_L^c$	$n_0^c$	$\lambda$ (nm)	$\Delta\lambda^d$ (nm)	$T_{\max}$ (abs. units)	$R_{\max}^e$ (abs. units)	Stop band <sup>f</sup> (nm)	Age <sup>g</sup>
PSM $\lambda$	LH $\times$ 6 + C + HL $\times$ 6	2.45	1.53	1.28	731	17	$\simeq 0.40$	$\simeq 0.95$	$\simeq 200$	1 year
PSM $\lambda/2$	LH $\times$ 6 + C + HL $\times$ 6	2.45	1.53	1.28	730	14	$\simeq 0.45$	$\simeq 0.95$	$\simeq 200$	1 year
PSM 75%	HL $\times$ 6 + C + LH $\times$ 6	2.1	1.63	1.30	692	10	$\simeq 0.40$	$\simeq 0.95$	$\simeq 130$	10 days
PSM 62%	HL $\times$ 6.5 + C + HL $\times$ 6.5	2.42	1.52	1.52	741	9	$\simeq 0.60$	$\simeq 0.95$	$\simeq 150$	10 days
PSM 45%	HL $\times$ 6 + C + LH $\times$ 6	2.1	1.63	2.2	692	9	$\simeq 0.60$	$\simeq 0.95$	$\simeq 150$	10 days

Source: Adapted from [2].

<sup>a</sup>The name of the sample also contains information about the thickness of the central layer for the first two rows and refers to the porosity of the central layer, which was  $\lambda/2$  thick, for the last three rows.

<sup>b</sup>Sequences of the periodic stacking of high refractive index (H, 62% porosity) and low refractive index (L, 45% porosity) layers; C stands for the central layer.

<sup>c</sup> $n_H$ ,  $n_L$ , and  $n_0$  refer to the refractive index values for the high refractive index layer, the low refractive index layer, and the central layer, respectively, measured on thick samples at  $\lambda$  (which is given in the next column and refers to the microcavity resonance).

<sup>d</sup>Measured FWHM of the microcavity transmission peak which has a maximum transmittance of  $T_{\max}$ .

<sup>e</sup>Maximum reflectance of the microcavity.

<sup>f</sup>Wavelength width of the high reflectivity region of the reflectance spectrum.

<sup>g</sup>Age of the microcavities when the measurements have been performed.

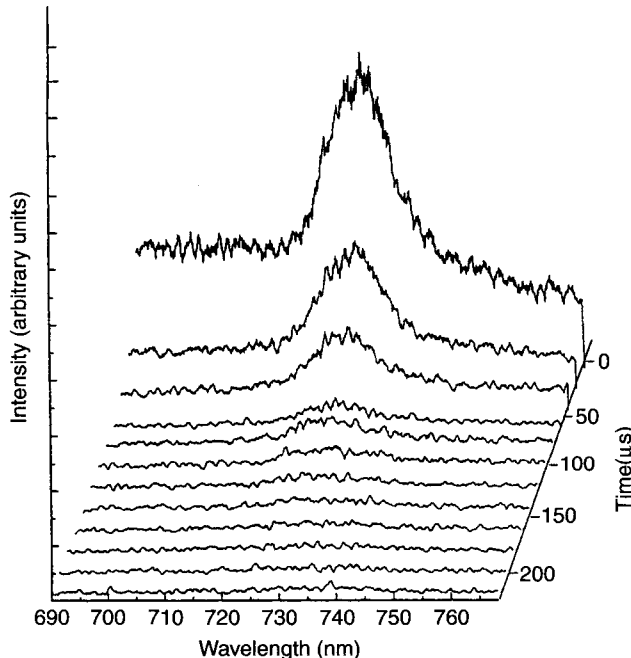


Fig. 78. Time-resolved luminescence taken at room temperature for the  $\lambda/2$  PSM. The time interval between the spectra is 25  $\mu$ s. Each spectrum has been integrated for 25  $\mu$ s. 0  $\mu$ s coincides with the excitation laser pulse. The different spectra are vertically displaced for clarity. Reprinted with permission after Ref. [2].

would have expected a shortening of the decay at  $\lambda_c$  and not for  $\lambda \neq \lambda_c$ .

The time decay of the luminescence at  $\lambda_c$  is shown in Figure 79 [2], where the time decay of a reference PS sample at the same observation wavelength also is reported for comparison. A faster decay for the PSM than for the PS is observed. The luminescence decays with a stretched

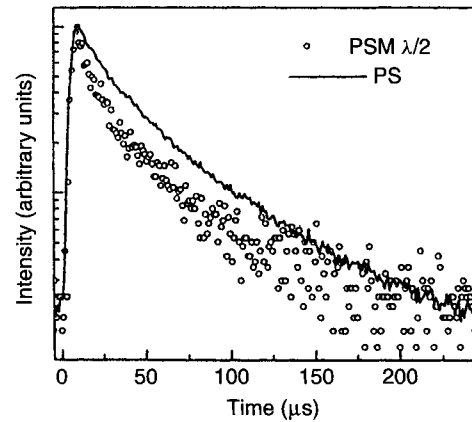


Fig. 79. Room-temperature time decay of the luminescence for the  $\lambda/2$  PSM (dots) and the reference PS sample (line) at the PSM resonance wavelength. Reprinted with permission after Ref. [2].

exponential lineshape (Eq. (12)) for both the PSM and the PS. A summary of the wavelength dependence of the  $\tau$  and  $\beta$  parameters is given in Figure 80. For the reference PS sample, an increasing  $\tau$  and an almost constant  $\beta$  are observed as  $\lambda$  increases. On the contrary, a bell-shaped  $\tau$  versus  $\lambda$  relation centered on  $\lambda_c$  is observed for the PSM sample (see also Table X). By comparing the absolute  $\tau$  value at  $\lambda_c$  of the PSM with that of the reference PS sample, decreases by a factor 1.2 or 1.9 for the  $\lambda_c$  or  $\lambda_c/2$  cavities, respectively, are measured. The  $\tau$  values for  $\lambda \neq \lambda_c$  could be compared with those measured for the mirror sample (Table X, second row).

A strong dependence on the excitation power intensity ( $J_{\text{exc}}$ ) has been observed. The time-integrated data under pulsed excitation are reported in Figure 81, where

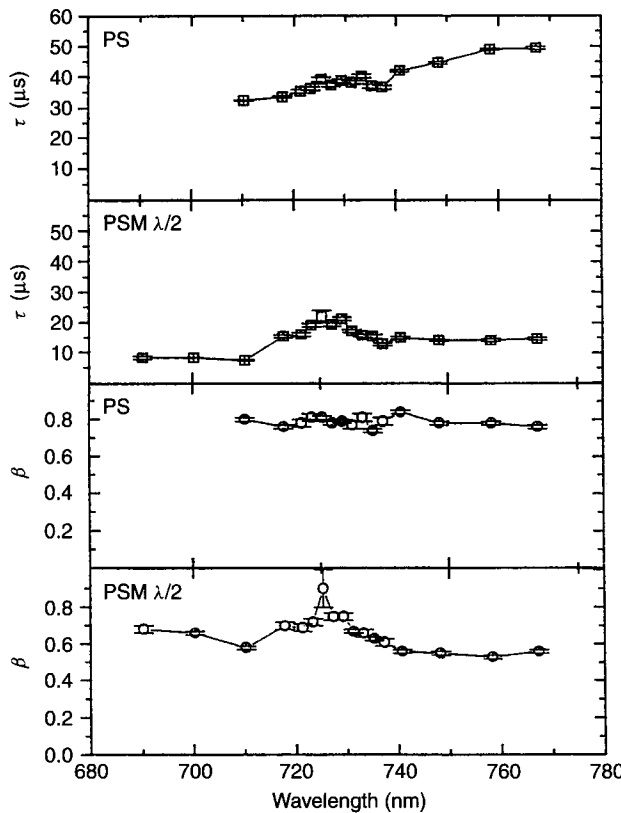


Fig. 80. Wavelength dependence of the  $\tau$  and  $\beta$  parameters extracted with a stretched exponential fit of the luminescence decays for the  $\lambda/2$  PSM and the reference sample. Reprinted with permission after Ref. [2].

the luminescence spectra for three different  $J_{\text{exc}}$  values are reported. As  $J_{\text{exc}}$  increases, the peak at  $\lambda_c$  is enhanced and some luminescence appears from the background, as a result of the mirror emission. A saturation of the mirror absorption is observed, which leads to an increased direct excitation of excitons in the central layer. This feature is also discussed in Section 6.5 and, in light of the temperature-dependent data, a qualitative model for this behavior is proposed.

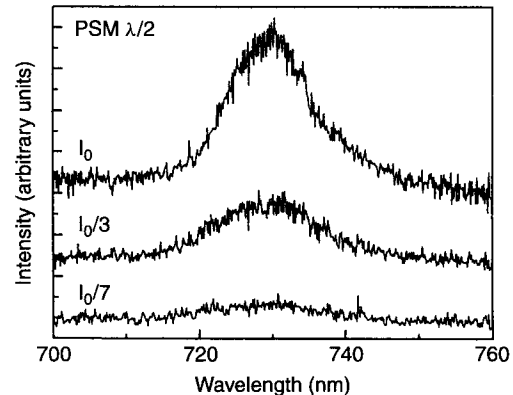


Fig. 81. Plot of the room-temperature time-integrated luminescence spectra of the  $\lambda/2$  PSM for different excitation powers (indicated on the left in units of  $I_0 = 500 \text{ W cm}^{-2}$ ). The spectra are vertically displaced for clarity. Reprinted with permission after Ref. [2].

The  $J_{\text{exc}}$  dependence of  $\tau$  is reported in Table XI. For  $\lambda \neq \lambda_c$  the  $\tau$  are almost independent on  $J_{\text{exc}}$ , whereas they increase at  $\lambda_c$ . This is due to increased central layer emission. In fact, at  $\lambda_c$  one can observe the emission of both the mirrors (fast decay) and the central layer (slow decay). As the  $J_{\text{exc}}$  increases and the mirror emission is saturated, the central layer emission dominates and the decay is lengthened. Complementary information can be derived from the dependence on the observation angle  $\phi$  of  $\tau$  and  $\beta$  as reported in Figure 82. As soon as  $\phi$  is increased, the photon confinement in the optical cavity weakens, and a lower exciton–photon coupling is observed. Because the coupling between the exciton and the photon weakens, as a result of the lower confinement of the photon modes, the luminescence decay time shortens and eventually becomes equal to those typical for the mirror emission. A very weak  $\phi$  dependence is expected for the mirror luminescence. Indeed,  $\phi$  dependence has been observed for the luminescence decay at wavelengths longer or shorter than  $\lambda_c$ .

The theoretical predictions report that no change in the luminescence lifetimes should be expected for

Table X Some Characteristics of the Aged Microcavities Compared with a Porous Silicon Layer (Here Named Ps) Obtained by Using the Same Etching Parameters as the Microcavity Central Layer and with a Dielectric Bragg Reflector (Here Named Mirror) Obtained by Using the Same Etching Parameters as the Microcavity Mirrors<sup>a</sup>

	$I_{\text{integ}}$	$I(\lambda_c)$	$\tau_{700} (\mu\text{s})$	$\beta_{700}$	$\tau_{730} (\mu\text{s})$	$\beta_{730}$	$\tau_{760} (\mu\text{s})$	$\beta_{760}$
PS	0.87	0.14	$32.4 \pm 0.2$	$0.80 \pm 0.01$	$37.4 \pm 0.6$	$0.78 \pm 0.01$	$49.0 \pm 0.4$	$0.78 \pm 0.01$
Mirror	0.68	0.07	$18.4 \pm 0.3$	$0.61 \pm 0.01$	$20.6 \pm 0.3$	$0.62 \pm 0.01$	$29.4 \pm 0.7$	$0.55 \pm 0.01$
$\lambda$ -cavity	0.97	0.97	$10.9 \pm 0.4$	$0.54 \pm 0.01$	$30.9 \pm 0.7$	$0.69 \pm 0.01$	$24 \pm 1$	$0.44 \pm 0.01$
$\lambda/2$ -cavity	1	1	$8.3 \pm 0.2$	$0.66 \pm 0.01$	$19.5 \pm 0.6$	$0.75 \pm 0.02$	$19.9 \pm 0.8$	$0.51 \pm 0.01$

Source: Adapted from [2].

<sup>a</sup> $I_{\text{integ}}$  refers to the spectrally integrated luminescence intensity,  $I(\lambda_c)$  to the peak emission intensity at the wavelength of the microcavity resonance ( $\lambda_c = 730 \text{ nm}$ ); the  $\tau$  and  $\beta$  refer to the parameters obtained from a least squares fitting with a stretched exponential lineshape for the luminescence decay at the wavelength indicated as subscripts (units of nanometers).

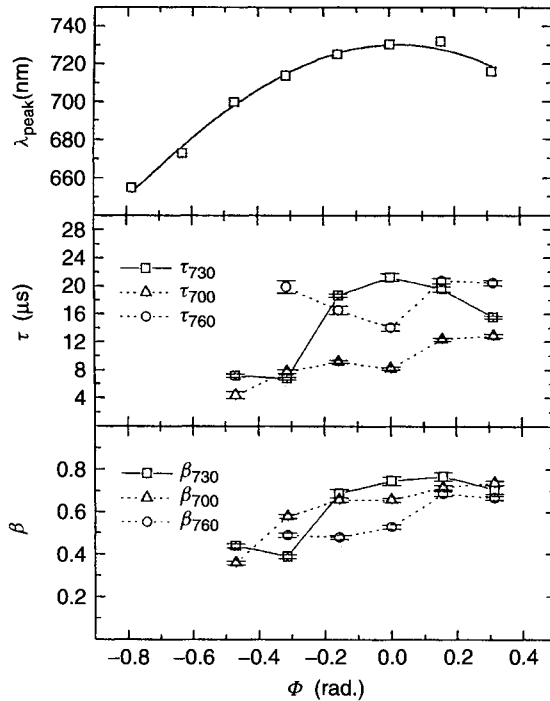


Fig. 82. The observation angle ( $\phi$ ) dependence of the luminescence maximum wavelength ( $\lambda_c$ ) and of the  $\tau$  and  $\beta$  parameters for the  $\lambda/2$  PSM.  $\Phi$  is calculated with respect to the normal to the microcavity surface. The subscripts to the  $\tau$  and  $\beta$  labels refer to the wavelength given in nanometers. Reprinted with permission after Ref. [2].

microcavities formed with DBRs [185]; the observed shortening can be explained by investigation of the effects of varying the refractive index of the central layer ( $n_c$ ) while keeping constant the parameters of the Bragg reflectors. In this way, the effect of the photon confinement by the optical cavity is separated from the bulk excitonic effect. A series of three PSMs with 45, 62, and 75% porosities of the central layer have been investigated together with the corresponding reference PS samples (Table IX). A comparison of the respective reflectivity spectra is given in Figure 83. The luminescence intensity of these samples is reported in Figure 84 and compared with that of a reference DBR and of the reference PS samples. Note that the reference

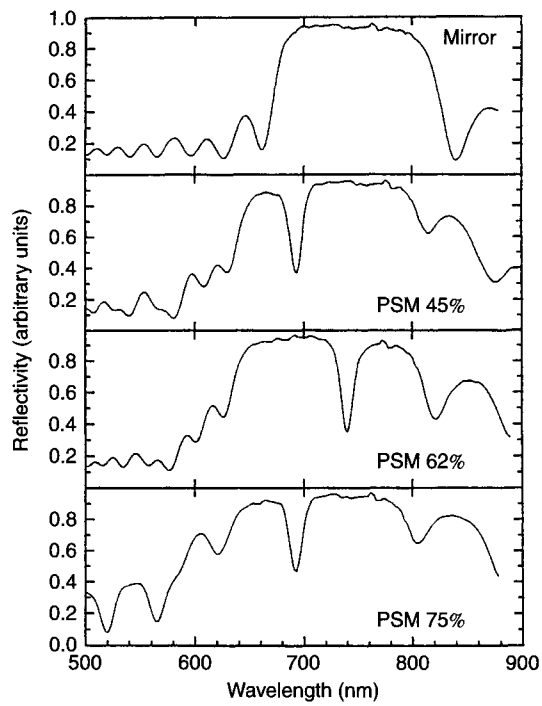


Fig. 83. Plot of the room-temperature reflectance spectra of PSM with different porosities (labeled as PSM NN%) for the central layer. As a reference the reflectance of a DBR obtained by using the same etching parameters as those for the PSM mirrors is reported in the top panel. Reprinted with permission after Ref. [2].

PS sample with a porosity of 45% does not show any luminescence within the sensitivity of the experimental setup used. Looking at Figure 84 and at Tables XII and XIII, many comments are possible:

- the luminescence intensity of the PSM samples shows an enhancement of  $\lambda_c$  with respect to both the mirror luminescence and the PS reference luminescence;
- this enhancement is dependent on  $n_c$  it increases with increasing  $n_c$ ;
- the overall luminescence intensity increases with increasing  $n$  for the reference PS samples, whereas it decreases with increasing  $n_c$  for the PSM samples.

Table XI Excitation Power Dependence of the Luminescence Decay of the  $\lambda/2$ -Cavity<sup>a</sup>

	$\tau_{700}$ ( $\mu$ s)	$\beta_{700}$	$\tau_{730}$ ( $\mu$ s)	$\beta_{730}$	$\tau_{760}$ ( $\mu$ s)	$\beta_{760}$
$I_0$	$8.3 \pm 0.2$	$0.66 \pm 0.01$	$19.5 \pm 0.6$	$0.75 \pm 0.02$	$14.1 \pm 0.4$	$0.55 \pm 0.01$
$I_0/3$	$10.9 \pm 0.5$	$0.60 \pm 0.02$	$14.0 \pm 0.9$	$0.64 \pm 0.03$	$17.6 \pm 0.9$	$0.49 \pm 0.02$
$I_0/7$	$12 \pm 1$	$0.35 \pm 0.02$	$10 \pm 1$	$0.48 \pm 0.03$	$19 \pm 2$	$0.36 \pm 0.02$

Source: Adapted from [2].

<sup>a</sup> $I_0 \simeq 500 \text{ W cm}^{-2}$  is the excitation power intensity;  $\tau$  and  $\beta$  refer to the parameters extracted from a stretched exponential fit of the luminescence decay at the wavelength indicated as subscripts (units of nanometers).

Table XII Some Characteristics of Microcavities (Here Named PSM) with Different Central Layer Porosities (Indicated as  $NN\%$ ) Compared with Porous Silicon Layers (named PS  $NN\%$ ) Obtained by Using the Same Etching Parameters as the Microcavity Central Layers and with Dielectric Bragg Reflectors (Named Mirror) Obtained by Using the Same Etching Parameters as the Microcavity Mirrors<sup>a</sup>

	$I_{\text{integ}}$	$I(\lambda_c)$	$\tau_{\text{cavity}} (\mu\text{s})$	$\beta_{\text{cavity}}$	$\tau_{650} (\mu\text{s})$	$\beta_{650}$	$\tau_{750} (\mu\text{s})$	$\beta_{750}$
PS 45%	—	—	—	—	—	—	—	—
PS 62%	0.13	0.03	$22 \pm 2$	$0.50 \pm 0.03$	$9.5 \pm 0.6$	$0.67 \pm 0.04$	$25 \pm 3$	$0.73 \pm 0.08$
PS 75%	0.26	0.08	$20.2 \pm 0.5$	$0.72 \pm 0.01$	$9.6 \pm 0.3$	$0.62 \pm 0.01$	$28 \pm 2$	$0.69 \pm 0.03$
Mirror (45%)	0.84	0.23	$7.5 \pm 0.3$	$0.47 \pm 0.01$	$5.2 \pm 0.3$	$0.52 \pm 0.02$	$11.8 \pm 0.5$	$0.48 \pm 0.01$
(62%)		0.20	$9.2 \pm 0.4$	$0.49 \pm 0.01$				
(75%)		0.24	$7.5 \pm 0.3$	$0.47 \pm 0.01$				
PSM 45%	1	0.81	$9.8 \pm 0.1$	$0.62 \pm 0.01$	$3.4 \pm 0.1$	$0.54 \pm 0.01$	$8.4 \pm 0.1$	$0.43 \pm 0.01$
PSM 62%	0.95	0.66	$13.3 \pm 0.1$	$0.62 \pm 0.01$	$2.4 \pm 0.4$	$0.38 \pm 0.01$	$10.7 \pm 0.4$	$0.44 \pm 0.01$
PSM 75%	0.92	1	$15.2 \pm 0.1$	$0.62 \pm 0.01$	$5.5 \pm 0.1$	$0.40 \pm 0.01$	$8.9 \pm 0.1$	$0.48 \pm 0.01$

Source: Adapted from [222].

<sup>a</sup>All the microcavities had the same etching parameters and central layer porosity.  $I_{\text{integ}}$  refers to the spectrally integrated luminescence intensity,  $I(\lambda_c)$  to the peak emission intensity at the wavelength of the microcavity resonance ( $\lambda_c$ );  $\tau$  and  $\beta$  refer to the parameters extracted from a stretched exponential fit of the luminescence decay at the wavelength indicated as subscripts (in units of nanometers or as *cavity* at  $\lambda_c$ ). The  $\tau$  and  $\beta$  at  $\lambda_c$  for the mirror are reported for the different  $\lambda_c$  of the various PSMs.

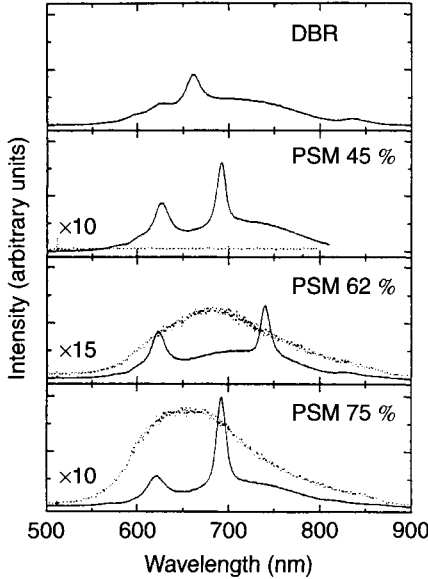


Fig. 84. Plot of the room-temperature luminescence spectra of PSM with different porosities (labeled as PSM  $NN\%$ ) for the central layer. For each PSM  $NN\%$  spectrum (solid line) the corresponding spectrum for a porous layer of porosity  $NN\%$  is shown (dotted line) after multiplication by the factor indicated on the left. For a comparison the luminescence of a dielectric Bragg reflector obtained by using the same etching parameters as those for the PSM mirrors is shown in the top panel. The spectra are in relative units. Reprinted with permission after Ref. [2].

The time-resolved measurements are summarized in Tables XII and XIII. Also for the  $\tau$  some comments are worthwhile:

Table XIII Ratio of the Peak Emission Intensity  $I^{\text{PSM}}(\lambda_c)/I^{\text{PS}}(\lambda_c)$  and Luminescence Decay Time  $\tau^{\text{PSM}}/\tau^{\text{PS}}$  of the Porous Silicon Microcavities versus the Reference PS Samples

$n_c$	$\frac{I^{\text{PSM}}(\lambda_c)}{I^{\text{PS}}(\lambda_c)}$	$\frac{\tau^{\text{PSM}}}{\tau^{\text{PS}}}$
PSM 45%	2.2	$\infty$
PSM 62%	1.52	22
PSM 75%	1.30	12.5

Source: Adapted from [222].

- the  $\tau$  values at  $\lambda_c$  increase as  $n_c$  decreases;
- the ratio of the  $\tau$  value at  $\lambda_c$  for the PSM, with respect to that of the reference sample, increases as  $n_c$  decreases; its value is always  $\leq 1$ .

Two main experimental observations merit detailed discussion: (a) the shortening of  $\tau$  for the PSM at  $\lambda_c$  with respect to the reference PS samples and as a function of  $n_c$ ; (b) the faster decay observed for  $\lambda \neq \lambda_c$  than for  $\lambda_c$  in the PSM.

The theoretical treatment of the coupling of the electronic resonance with the optical mode inside a microcavity has been reviewed in [185] by using classical arguments. It has been shown that dielectric microcavities differ from ideal or metallic microcavities for the finite reflection angle where the coupling is effective and for the penetration of the optical mode into the distributed Bragg reflectors. The finite reflection angle is reversed in that the spontaneous emission rate is modified only for the light emitted into such high reflectivity angles and it is virtually unmodified for all the other emission angles where the emission radiates into leaky waveguide modes.

As a consequence, the planar microcavity does not modify the spontaneous emission rate by any appreciable amount, and the emission is simply redistributed in the available space. In addition, inside a Bragg mirror the reflections are distributed over most of the interfaces, the optical mode confined in the central layer penetrates into the Bragg mirrors and, hence, part of the energy is stored in the mirrors.

On the basis of these facts, the modified continuous-wave (CW) luminescence lineshapes in PSM are explained by the redistribution of the emission in the space available to the photon mode, whereas while one would not expect any variation in the emission lifetime. The observed variations are then due to the change of the local dielectric environment caused by the finite penetration depth of the optical modes into the mirrors.

The spontaneous emission rate  $R_{sp}(\hbar\omega)$  for a bulk material is given by Eq. (29), where the photon mode density  $G(\hbar\omega)$  is

$$G(\hbar\omega) = \frac{n^3(\hbar\omega)^2}{\pi^2 c^3 \hbar^3} \quad (45)$$

and  $n$  is the refractive index of the material.

In Eq. (29) the electronic transitions couple with the optical mode, which has an energy  $\hbar\omega$  equal to the transition energy. In a microcavity the electronic transition occurs in the central layer; however, the optical mode, to which the excitonic transition couples, extends inside the DBR. Consequently, the refractive index used in Eq. (45) is not that of the central layer but an average of the refractive indexes of the layers where the optical mode extends.

An estimate of the penetration length ( $\ell_p$ ) of the photon mode into the DBR is given in [216],

$$\ell_p = \frac{\lambda_c}{4n_c} \frac{q}{1-p} \frac{(1+a^2 p^{m-1})(1-p^m)}{(1+q^2 a^2 p^{2m-2})} \quad (46)$$

where  $q = n_c/n_L$ ,  $p = n_L/n_H$ ,  $a = n_H/n_{air}$  or  $a = n_H/n_{Si}$ , depending on whether the top DBR or the bottom DBR is considered,  $n_{air}$  and  $n_{Si}$  are the refractive index of air and silicon, respectively, and  $m$  is the number of stacks in the DBR.

The effective refractive index  $n_{DBR}$  of the DBR can be approximated by the spatial average of the high and the low refractive indexes, that is,  $n_{DBR} = (n_H \ell_H + n_L \ell_L)/(\ell_H + \ell_L)$  where  $\ell_H$  and  $\ell_L$  are the respective thicknesses of the various layers of the DBR.

Hence the effective refractive index  $n_{eff}$  entering into Eq. (45) is approximated by the average over the spatial extent of the optical mode

$$n_{eff} = \frac{n_{DBR} \ell_p^{Si} + n_{DBR} \ell_p^{air} + \lambda_c/2}{\ell_p^{air} + \ell_p^{Si} + \lambda_c/(2n_c)} \quad (47)$$

Table XIV Optical Mode Extension into the DBR (with a Medium Refractive Index  $n_{DBR}$ ) and Effective Refractive Index ( $n_{eff}$ ) for Various Porous Silicon Microcavities<sup>a</sup>

	$n_{DBR}$	$\ell_p^{air}$ (nm)	$\ell_p^{Si}$ (nm)	$n_{eff}$
PSM $\lambda$	1.884	200	198	1.528
PSM $\lambda/2$	1.884	200	198	1.632
PSM 45%	1.835	559	459	1.872
PSM 62%	1.867	338	327	1.774
PSM 75%	1.835	511	469	1.721

Source: Adapted from [222].

<sup>a</sup> $\ell_p^{air}$  and  $\ell_p^{Si}$  are the penetration lengths on the air and silicon sides, respectively.

where  $\ell_p^{air}$  and  $\ell_p^{Si}$  are the penetration lengths on the air side and on the Si side, respectively.

Table XIV reports the results of such a calculation. Let us note that:

- the  $\ell_p$  for the two one-year-old samples are shorter than for the other three samples, because for the former the central layer is embedded between two high refractive index layers;
- the penetration depths are longer on the air side than on the Si side;
- the large dielectric mismatch between the average refractive index of the DBR and that of the central layer is greatly reduced if one considers  $n_{eff}$  instead of  $n_c$ ;
- for the second set of samples, because of the small thickness of the central layer with respect to the penetration depth of the optical mode into the DBR,  $n_{eff}$  has a weaker dependence on the central layer porosity than  $n_c$ .

If one could neglect the contribution of the nonradiative transitions, the measured luminescence decay times would be related to the radiative lifetime and, hence, should fit the  $n$ -dependence given by Eq. (45). Again, this hypothesis is better discussed in Section 6.5. Figure 85 reports  $\tau^{-1}$  as a function of  $n$  [215]. All the data for a representative set of PSMs, summarized in Table XII, are reported there.  $n_{DBR}$  and  $n_{eff}$  have been used for the mirror and PSM data. A power-law fit to the data yields  $1/\tau \propto n^{3.4}$ , which is very similar to the cubic dependence predicted by Eq. (45).

One conclusion is now possible from this figure: the measured  $1/\tau$  values show a dependence on the refractive index that explains most of the observed results. In particular:

- the luminescence decay is faster for the mirror than for the PSM because of the larger refractive index of the mirror than for the PSM;

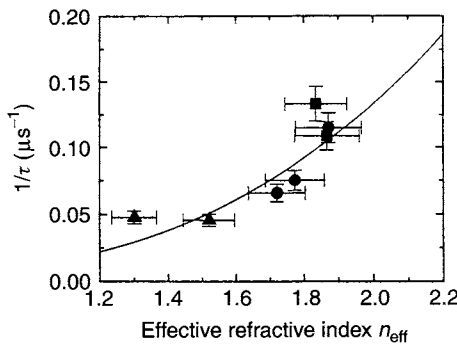


Fig. 85. Effective refractive index dependence of  $1/\tau$ . The various symbols refer respectively to (triangles) reference samples, (squares) DBR, and (discs) PSM. All the data correspond to the resonance wavelength of the PSM. See Table XII. Adapted from [215].

- the reduced lifetimes observed in the PSM with respect to the reference PS samples are due to the different refractive indexes ( $n_c$  versus  $n_{\text{eff}}$ );
- the dependence of the luminescence enhancement on  $n_c$  (see Table XIII) is a consequence of the dependence of the luminescence intensity on  $n$  (Eq. (5)). In fact,  $I_{\text{PL}} \propto 1/\tau \simeq n^3$ .

### 6.5. Temperature Dependence of Porous Silicon Microcavities

Figure 86 shows the PL spectra of a PSM for various temperatures  $T$  [211].

As  $T$  increases to room temperature (RT), the lineshape remains unchanged, and the main variation is in the relative emission intensity from the cavity and the mirrors.

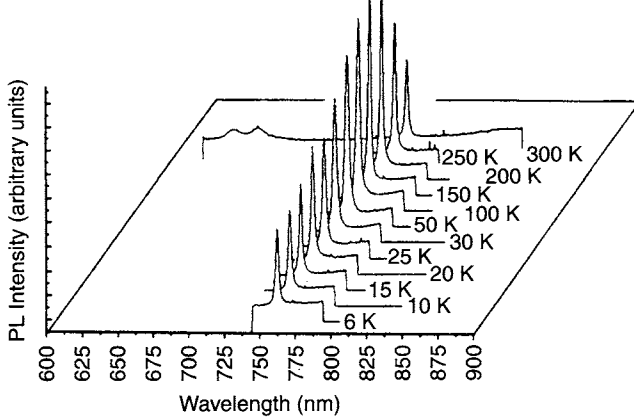


Fig. 86. Photoluminescence as a function of temperature for sample A. The spectra have been shifted for clarity. The horizontal line is the baseline for each spectrum. The measurement temperatures are given on the right. Reprinted with permission after Ref. [211].

In the figure, the various PL spectra are normalized to the mirror emission. Thus one observes an increased emission from the cavity for  $T$  up to 150 K; then for higher  $T$  the emission of the cavity weakens with respect to the mirror emission. Other details of the temperature dependence of the emissions are reported in Figure 87.

Figure 87a shows the peak intensity ( $I_{\text{PL}}$ ) of the cavity resonance mode as a function of  $T$ . A bell-shaped curve is observed as with standard PS samples [1]. This behavior has been explained already as resulting from the interplay of radiative and nonradiative recombinations. At low  $T$ , the PL is dominated by radiative recombinations, where the radiative lifetime is due to the thermal balance between occupation of the dipole-prohibited triplet state and the dipole-allowed high-energy singlet state. As  $T$  increases, the singlet population increases and the luminescence intensity increases. When  $T$  is high enough, fast nonradiative recombinations occur and the luminescence intensity decreases. This general trend is respected in Figure 87a.

Figure 87b reports the  $T$  dependence of the cavity peak position. As  $T$  decreases from RT to 150 K,  $\lambda_c$  diminishes. In addition, decreasing  $T$ ,  $\lambda_c$  remains constant within the experimental error bars. The decrease in  $\lambda_c$  reflects the temperature variation of  $n_c$ :  $\lambda_c = n_c \times d$ , where  $d$  is the cavity thickness. The FWHM of the emission peak ( $\Delta\lambda$ )

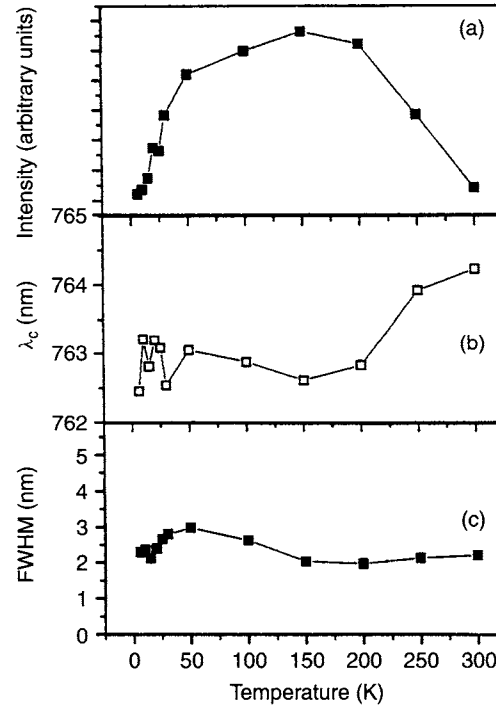


Fig. 87. Summary of the temperature dependence of some parameters extracted from the luminescence of sample A: (top) peak intensity of the cavity mode; (center) spectral position; (bottom) full width at half maximum. Reprinted with permission after Ref. [211].

is given in Figure 87c. The near constance of  $\Delta\lambda$  versus  $T$  indicates that the linewidth of the cavity mode is determined only by the microcavity structure and not by the excitonic thermalization for all of the  $T$  range here investigated.

It is of interest to know how the enhancement of the emission intensity ( $I_{PL}$ ) observed for PSMs depends on  $T$ . In Figure 88 reports the emission intensity and the ratio ( $\gamma$ ) of  $I_{PL}$  at  $\lambda_c$  for a PSM and for a reference PS sample as a function of  $T$ . For this sample,  $\gamma \approx 2$  at room temperature.  $\gamma$  is almost independent of  $T$  as long as  $T > 100$  K, whereas it increases strongly at lower temperatures. The inset shows the  $T$  dependence of  $I_{PL}$  at  $\lambda_c$  for the PSM and the reference PS sample. A bell-shaped  $I_{PL}$  profile is measured for both the samples but the  $I_{PL}$  maximum occurs at lower  $T$  for PSM than for PS. The  $T$  dependence of  $\tau$  is reported in Figure 89 for PSM and PS at  $\lambda_c$ . The same trend as that observed for the usual PS samples is seen [172]. For  $\beta$  (not shown in the figure), it is constant from 300 K to 100 K, and then decreases as  $T$  is decreased. Both these trends have been explained already: for  $\tau$ , by introducing a two-level system (singlet and triplet excitons) and by assuming the exciton thermalization between them [173]; for  $\beta$ , by assuming a dispersive diffusion of excitons in a disordered Si-nanocrystals arrangement and by introducing the trap-controlled hopping of excitons [172].

The  $\tau$  versus  $T$  dependence can be described by the temperature dependence of the occupation of the singlet and triplet levels [173]:

$$\tau_{rad}(T) = \tau_{trip} \left[ \frac{1 + (1/3) \exp(-\Delta E_x/k_B T)}{1 + (1/3)(\tau_{trip}/\tau_{sing}) \exp(-\Delta E_x/k_B T)} \right] \quad (48)$$

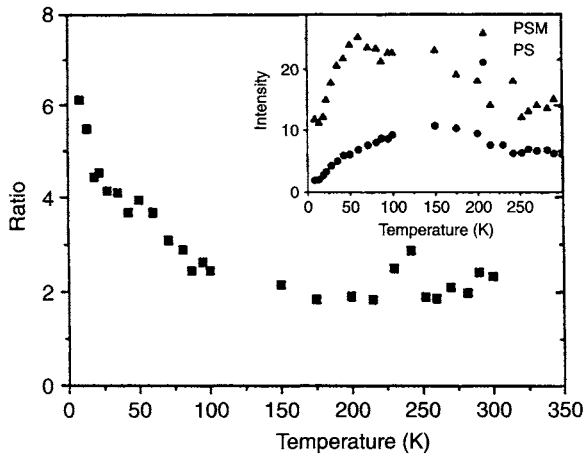


Fig. 88. Comparison of the PL intensity ratio of a PSM (sample B) and of a reference PS sample as a function of the temperature, at the cavity emission wavelength. The inset shows the bare data for the reference PS sample (circles) and the PSM (triangles). Reprinted with permission after Ref. [211].

where  $\tau_{trip}$  is the triplet lifetime,  $\tau_{sing}$  is the singlet lifetime, and  $\Delta E_x$  is the singlet-triplet energy splitting. A fit of the experimental data for  $T < 150$  K (see Fig. 89) yields the parameters reported in Table XV.  $\Delta E_x$  is essentially unchanged by the cavity structure, whereas the singlet and triplet lifetimes show different values in PSM and PS. In the last column of the table, the data for  $\lambda \neq \lambda_c$ , that is, representative of the mirror emission, are reported.

The inset of Figure 89 shows the ratio of the PSM and PS lifetimes at  $\lambda_c$ . Its value is less than 1 (i.e., the lifetime of PSM is shorter than that of PS within the error bars) down to 40 K, where it starts to grow. This is the temperature region where recombination from the triplet states dominates.

The variations of the PL spectra at room temperature for various excitation intensities ( $J_{exc}$ ) are reported in Figure 90. As  $J_{exc}$  increases, the cavity mode emerges

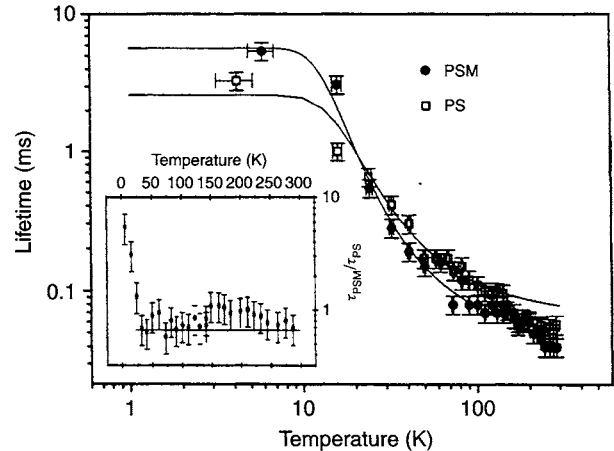


Fig. 89. Temperature dependence of the luminescence decay time at the wavelength of the cavity mode ( $\lambda_c$ ) for the PS (empty squares) and the PSM sample (filled circles) as deduced from a stretched exponential fit of the experimental decays. The lines are fits with Eq. (4), which yields the parameters reported in Table I. The inset shows the ratio between the lifetimes of PSM ( $\tau_{PSM}$ ) and of PS ( $\tau_{PS}$ ). The horizontal line indicates  $2/3$ , which is the value theoretically expected for ideal microcavities. Reprinted with permission after Ref. [211].

Table XV Results of the Least Squares Fitting of the Temperature Dependence of the Luminescence Lifetimes Shown in Figure 89 with Eq. (48)<sup>a</sup>

Sample	$\Delta E_x$ (meV)	$\tau_{trip}$ (ms)	$\tau_{sing}$ (μs)
PS (at $\lambda_c$ )	$6 \pm 0.4$	$2.6 \pm 0.7$	$17 \pm 1$
PSM (at $\lambda_c$ )	$7 \pm 0.3$	$5.9 \pm 0.6$	$10 \pm 1$
PSM (at $\lambda = 695$ nm)	$7 \pm 0.6$	$1 \pm 0.2$	$8 \pm 1$

Source: Adapted from [222].

<sup>a</sup> $\Delta E_x$ ,  $\tau_{trip}$ , and  $\tau_{sing}$  are the triplet-singlet splitting energy, the triplet lifetime, and the singlet lifetime, respectively.

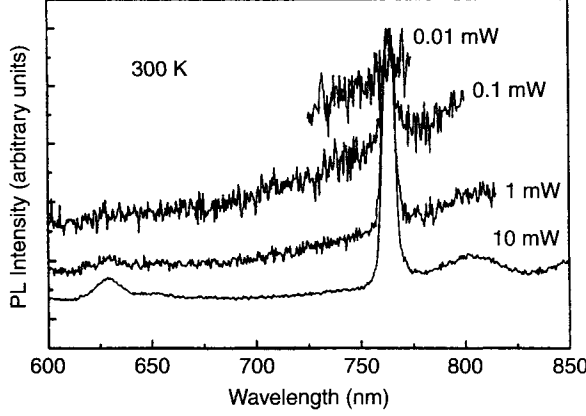


Fig. 90. Incident intensity dependence of the luminescence spectrum of sample B. The various spectra have been normalized to their maximum. The temperature was 300 K. The excitation area was  $3 \times 10^{-4} \text{ cm}^3$ . Reprinted with permission after Ref. [211].

from the background of the mirror luminescence and a well-resolved peak is measured.

The  $J_{\text{exc}}$  dependence of  $I_{\text{PL}}$  is shown in Figure 91 for various  $T$ .

$I_{\text{PL}} \propto J_{\text{exc}}^\alpha$  with  $\alpha \leq 1$ ,  $\alpha$  versus  $T$  is shown in Figure 92. An almost constant  $\alpha$  is observed. Only at low  $T$  does  $\alpha$  go to the value of about 0.5. On the other hand,  $\tau$  and  $\beta$  are approximately constant when  $J_{\text{exc}}$  is varied.

The present experimental data support the conclusions reached in [215], which are based on the theoretical work of [185]. In addition, the following points can be stated:

- The coupling of the singlet state with the photon mode reduces the singlet lifetime in the PSM. This contributes to the increase in the overall luminescence intensity and to the fractional shortening of the time decay of the

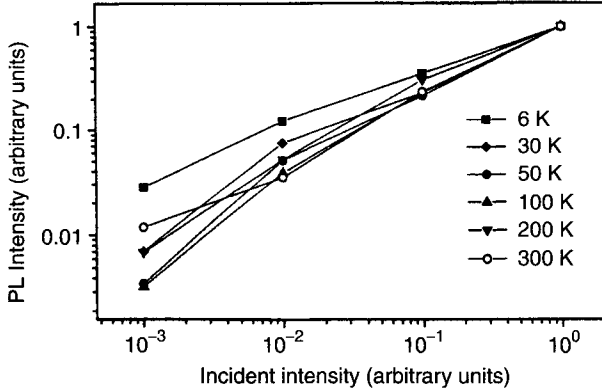


Fig. 91. Incident intensity dependence of the PL peak intensity at the cavity mode for the various temperatures indicated in the figure. The intensity has been normalized to the maximum intensity used. Reprinted with permission after Ref. [211].

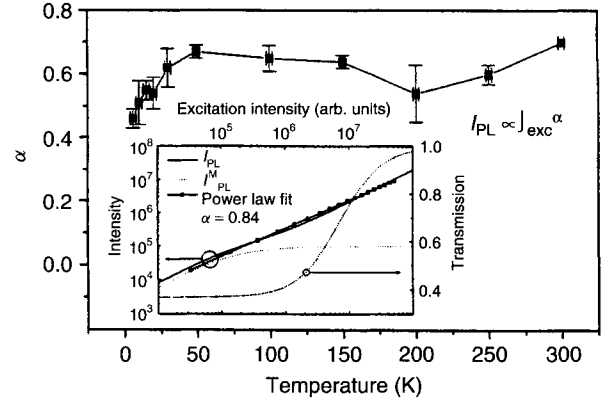


Fig. 92. Temperature dependence of the  $\alpha$  exponent defined with the formula given in the figure, where  $I_{\text{PL}}$  is the cavity wavelength and  $J_{\text{exc}}$  the excitation intensity. PSM sample B has been used: (inset) result of the simple model described in Section IV; (dashed line) transmission coefficient  $T$ ; (dotted line) luminescence from the mirror; (solid line) total luminescence intensity; (squares) result of a power-law fit with  $\alpha = 0.84$ . Reprinted with permission after Ref. [211].

luminescence (which is also dependent on the local dielectric environment).

- The luminescence lifetime at low temperatures (here identified with  $\tau_{\text{trip}}$ ) is due to the balance between the nonradiative and the radiative recombinations, but not the dipole-allowed recombinations (see Figure 2 in [172]). The results for the different samples are due to sample-dependent properties rather than to the microcavity structures.
- It is mainly in the intermediate temperature range, where the thermal population of the singlet state is important, that the two-level internal structure of the excitons in PS plays a role. The different  $T$  of the maxima of  $I_{\text{PL}}$  for PSM and PS are explained by the lower  $\tau_{\text{sing}}$  in PSM than in PS. In PSM samples with a very long  $\tau_{\text{trip}}$  as those reported in [203],  $I_{\text{PL}}$  increases monotonously even at low  $T$ . At room temperature, the lifetime is again governed by the balance of the radiative and nonradiative recombinations. However, as already observed in [217]

$$W_{\text{tot}}(n) = W_{\text{nr}} + W_{\text{r}} \simeq W_{\text{nr}} + f(n)W_{\text{r}} \quad (49)$$

where  $W_{\text{xxx}}$  are the total ( $\text{xxx} = \text{tot}$ ), nonradiative ( $\text{xxx} = \text{nr}$ ), and radiative ( $\text{xxx} = \text{r}$ ) recombination rates, respectively;  $f(n)$  is a function that gives the dependence of the radiative recombination rate on the effective refractive index, already introduced in Eq. (45) and discussed in [215];  $W_{\text{nr}}$  is independent of  $n$ . Equation (49) explains why the microcavity effects, that is, the variation of  $W_{\text{r}}$  with  $n$  through  $f(n)$ , are observed even at room temperature, where  $W_{\text{nr}}$  is large.

- The  $J_{\text{exc}}$  dependence of the PL spectra shown in Figure 90 is due to the saturation of the mirror absorption as the excitation intensity is increased. As more excitons are directly photogenerated into the cavity layer as a result of the increased transparency of the mirror (result of the absorption saturation), the luminescence at the cavity wavelength increases with respect to that at different wavelengths.
- The power dependence of the PL intensity at  $\lambda_c$  and the temperature dependence of the  $\alpha$  exponent are due to the saturation of the mirror emission at  $\lambda_c$ . In fact, the luminescence at  $\lambda_c$  is due to the sum of the mirror luminescence ( $I_{\text{PL}}^{\text{M}}$ ) and the cavity emission ( $I_{\text{PL}}^{\text{C}}$ ):

$$I_{\text{PL}} = I_{\text{PL}}^{\text{M}} + I_{\text{PL}}^{\text{C}} \quad (50)$$

Even though  $I_{\text{PL}}^{\text{C}}$  can have a linear dependence on  $J_{\text{exc}}$ ,  $I_{\text{PL}}$  has a sublinear dependence related to the mirror contribution. In fact, the absorption saturation of the mirror luminescence can be modeled as

$$I_{\text{PL}}^{\text{M}} \propto (1 - T) J_{\text{exc}} \quad (51)$$

where  $T$  is the transmission coefficient of the mirror; that is,  $(1 - T)$  is the absorbance in the mirror layers,

$$T \simeq \exp[-\chi(J_{\text{exc}})d_M] \quad (52)$$

where  $\chi(J_{\text{exc}})$  is the excitation intensity dependent absorption coefficient of the mirror layers (with a total thickness of  $d_M$ ). In a simple model

$$\chi \simeq \frac{\chi^0}{(1 + J_{\text{exc}}/J^{\text{Sexc}})} \quad (53)$$

and the  $J^{\text{Sexc}}$  is the saturation intensity. As  $J_{\text{exc}}$  increases,  $T$  increases,  $(1 - T)$  decreases, and the contribution from the recombination in the mirror spatial region decreases, which causes an  $\alpha < 1$ . A schematic idea of this behavior is shown in the inset of Figure 92, where a power-law fit of the resulting  $I_{\text{PL}}$  yields an  $\alpha \simeq 0.84$ . As  $J^{\text{Sexc}}$  depends on the temperature and increases for low  $T$ , this causes a larger contribution of  $I_{\text{PL}}^{\text{M}}$  to  $I_{\text{PL}}$ , which in turn causes a decrease in  $\alpha$  because most of the excitons are photoexcited in the mirror region, which exhibits the strongest absorption saturation.

- No variations in  $\Delta E_x$  caused by the PSM are observed because a weak exciton–photon coupling is present in PSM.

## 6.6. Coupled Porous Silicon Microcavities

Coupled cavities made of III–V semiconductors have been grown and characterized [218–221]. These structures consist of two coupled planar Fabry-Perot microcavities, surrounded by an external DBR: the coupling is

achieved via a central Bragg mirror (see Fig. 93 [213]). The coupling of the degenerate cavity modes through the central DBR induced by the coherent optical field leads to an optical splitting of the eigenmodes [218, 221]. Dual wavelength lasing has also been observed in vertical cavity surface emitting laser structures [219, 220]. The coupled cavity structure adds another degree of freedom in the tailoring of spatially confined light–matter coupling; it may lead to interesting effects such as, for example, the transfer of the excitation from one cavity to another.

In this section we describe the growth of coupled PSM with good optical properties. The layer sequence used to form the coupled PSM is as follows: air–HL... (×8) ...HL–S<sub>1</sub>–LH... (×4.5) ...L–S<sub>2</sub>–LH... (×8) ...LH–substrate, where S<sub>1</sub> and S<sub>2</sub> are the first and second cavities. The final structure is depicted in Figure 93 and is composed of three DBRs (top mirror DBR<sub>1</sub>, central mirror DBR<sub>2</sub>, and bottom mirror DBR<sub>3</sub>) formed by  $\lambda/4$  stacks and two  $\lambda/2$  cavity regions, S<sub>1</sub> and S<sub>2</sub>. In the balanced PSM, that is, in a sample in which S<sub>1</sub> and S<sub>2</sub> are equal, their thickness is  $L_c = \lambda_c/(2n_c)$ . The various samples are characterized by different values of the thicknesses of S<sub>1</sub> and S<sub>2</sub> as detailed in Table XVI.

In Figure 94, the reflectivity spectrum of the balanced coupled PSM is proposed. The characteristic high-reflectivity region due to the stop bands of the three DBRs extends from 650 to 850 nm. Within this wavelength ( $\lambda$ ) region, two reflectivity resonances are observed at 739 and 766 nm due to the coupling between the optical modes confined in the first and second cavities. A maximum transmittivity of 0.44 and 0.27 is associated with the low and high  $\lambda$  resonance, respectively. Even though the two

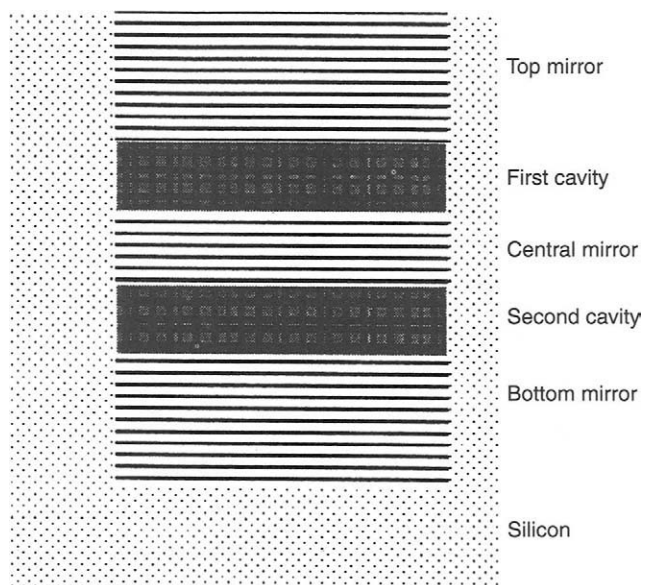


Fig. 93. Schematic sketch of the coupled microcavity structure. Adapted from [213].

Table XVI Thicknesses of the Two Cavity Layers ( $S_1$  and  $S_2$ ) in Units of  $L_c = \lambda_c/(2n_c)$  of the Various Samples Studied<sup>a</sup>

Sample	$S_1$	$S_2$	$\lambda_1$ (nm)	$\lambda_2$ (nm)	FWHM <sub>1</sub> (nm)	FWHM <sub>2</sub> (nm)	$A_1/A_2$	$L_1/L_2$
c	$L_c + L_c/50$	$L_c - L_c/50$	701.4	729.4	5.2	5.5	0.1	0.11
b	$L_c + L_c/100$	$L_c - L_c/100$	734.6	760.5	8.9	8.1	0.42	0.4
a	$L_c$	$L_c$	738.9	764.9	4.7	5.7	0.6	0.71
d	$L_c - L_c/100$	$L_c + L_c/100$	733.9	763.0	6.2	6.8	0.96	1.1
e	$L_c - L_c/50$	$L_c + L_c/50$	757.9	784.7	7.4	11.4	0.97	1.5

Source: Adapted from [222].

<sup>a</sup>The resonance wavelength  $\lambda_c$  in vacuum is 750 nm.  $\lambda_1$ ,  $\lambda_2$ , FWHM<sub>1</sub>, and FWHM<sub>2</sub> are the wavelengths and FWHM of the first (lower  $\lambda$ ) and second (higher  $\lambda$ ) cavity resonance, respectively.  $A_1/A_2$  ( $L_1/L_2$ ) is the ratio between the integrated (peak) emission intensities of the two resonances.

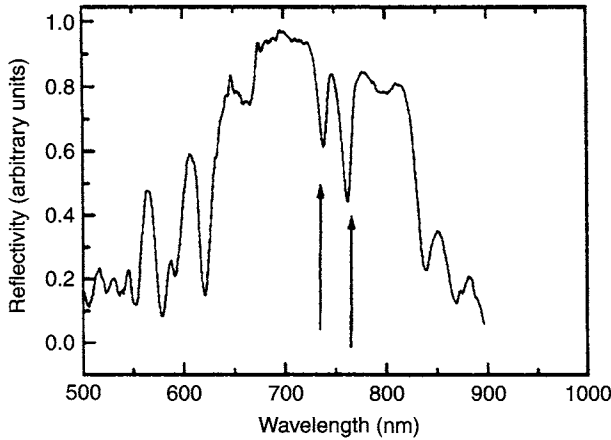


Fig. 94. Reflectance spectrum of the balanced all-porous silicon-coupled microcavity (sample a). The arrows point to the cavity modes. Adapted from [213].

cavities are equal, a different transmittivity is observed, probably as a result of the residual absorption of the central DBR at these wavelengths.

To study the coupled PSM in a deeper way, a series of samples with different mismatches between the two cavity layers has been produced and characterized. Figure 95 shows the PL spectra at room temperature for the various samples. Some information extracted from these spectra is summarized in Table XV.

The overall shape of the luminescence spectra is similar for all the samples and is very different from that typical of PS. Instead of a wide emission band characteristic of PS, several peaks are observed corresponding to the reflectivity minima of the PSM structure (see, e.g., Fig. 94). At the wavelengths of the coupled cavity modes, two peaks are observed whose intensities depend on the mismatch between the  $S_1$  and  $S_2$  cavities. The peculiar features of the PSM luminescence compared with that of PS are a consequence of the photon confinement in the cavity structure and have been discussed at length in preceding sections of this chapter and in [2, 203, 222].

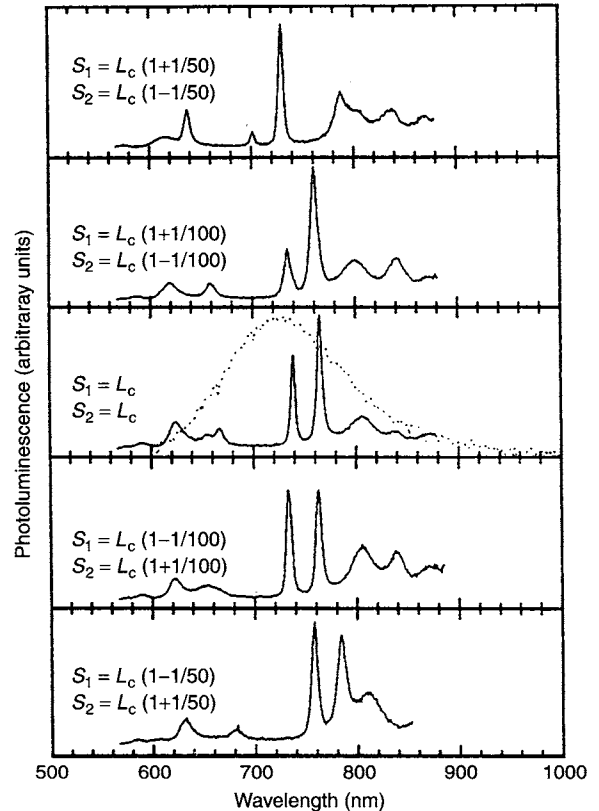


Fig. 95. Luminescence spectra of the coupled microcavities for the various thicknesses of the cavity layers indicated on the left. The spectra are in relative units. The spectra are in relative units. The dotted line in the central panel refers to a luminescence spectrum of a reference PS sample grown with the same etching parameters as the cavity layers. The spectrum has been normalized to its maximum and should be multiplied by a factor 0.09 to be reduced to the same relative units as the spectrum of the PSM. Adapted from [213].

Let us here concentrate only on the novel phenomena introduced by the coupled cavity structure. For the balanced sample labeled "a" (central spectrum in Fig. 95), two narrow peaks are observed at 739 and 765 nm corresponding to the transmittivity maxima measured in the reflectivity spectrum shown in Figure 94.

By varying the mismatch between  $S_1$  and  $S_2$ , several observations are possible:

- The growth process is well controlled as similar spectra are observed for the various samples, so we can conclude that all the variations are due to the different etching parameters used.
- The peak intensities vary as a function of the  $\Delta L_c$  (the thickness difference between  $S_1$  and  $S_2$ ). In particular, the low  $\lambda$  peak is stronger for sample labeled “c” and the high  $\lambda$  peak is strongest for the sample “e.” In the balanced sample “a,” an intensity difference between the emission of the two cavity modes is observed related to a residual absorption present in the DBR and to the wavelength dependence of the PS emission band (in the following we will refer to this fact as an asymmetry in the intensity).
- The spectral position does not change as a function of  $\Delta L_c$  except for samples “c” and “e,” in which a peak is spectrally aligned with those measured for the other samples, whereas the other peak is shifted to smaller (larger) wavelengths in the case of sample “c” (sample “e”).
- The linewidth of the luminescence peaks is almost independent of  $\Delta L_c$  and is significantly smaller than that typical of PS [222].

The theoretical modeling of the experimental results is done by assuming the dielectric constant  $\varepsilon(\omega) = \varepsilon_\infty + 4\pi\chi(\omega)$  in each layer, where  $\varepsilon_\infty = n^2$  is the background dielectric constant, and  $\chi(\omega)$  is a contribution arising from optical transitions close to the band gap. We assume for each PS layer a model of nanocrystals with dispersion of sizes, and assume the energies of spatially confined oscillators to be distributed according to a Gaussian function centered at  $\omega_0$ :

$$P(\omega) = \frac{1}{\Delta\sqrt{\pi}} \exp\left(-\frac{(\omega - \omega_0)^2}{\Delta^2}\right) \quad (54)$$

The width  $\Delta$  of the distribution corresponds to the width of the bulk PS PL [2]. Both  $\omega_0$  and  $\Delta$  depend on the porosity, with a trend of increasing  $\omega_0$  for increasing porosity, probably because of a smaller size for the Si nanocrystals. However, because the distribution of the PS PL is much larger than the energy range of interest (i.e., it extends well outside the stop band of the PSM structure), the same values for all PS layers are assumed. For the same reason, the results shown next do not depend on the precise form of the resonance frequency distribution: a different form, as assumed in [203], yields similar results. The resonant susceptibility is then obtained by a convolution of the single-oscillator form with the frequency

distribution:

$$\chi(\omega) = \int_{-\infty}^{\infty} P(x) \frac{\beta x^2}{x^2 - \omega^2 - 2i\gamma\omega} dx. \quad (55)$$

The susceptibility (55) can be expressed in terms of the complementary error function. Reflectivity and absorption spectra are then calculated by solving Maxwell equations by the usual transfer-matrix method [181, 223].

The calculations have been performed with the experimental parameters as the input. The external (central) DBR have  $N_1 = N_3 = 8$  ( $N_2 = 4.5$ ) pairs, respectively. The parameters of the oscillator model are  $\hbar\omega_0 = 1.65$  eV ( $\lambda_0 = 750$  nm),  $\Delta = 285$  meV, and  $\gamma = 15$  meV.

Useful analytical results for the double-microcavity configuration can be obtained by parameterizing the transfer matrix of the Bragg mirrors in terms of their amplitude reflection coefficients: this allows us to obtain the transfer matrix of the whole structure and to calculate the energies of the system eigenmodes, as the poles of the global transmission coefficient  $t(\omega)$  (the procedure was first applied to single microcavities in [207]). For a structure with two identical cavities, the optically coupled Fabry-Perot modes can be classified in terms of their symmetric (S) and antisymmetric (A) states; their splitting at normal incidence is calculated as

$$\Delta_{S-A} = \frac{\hbar c \sqrt{1 - R_2}}{n_c L_{\text{eff}}} \quad (56)$$

where  $R_2 = 1 - 4(n_H/n_c)^2(n_L/n_H)^{2N_2+1}$  is the reflectivity of the central mirror, and  $L_{\text{eff}} = L_c + L_{\text{DBR}}$  is an effective cavity length that includes the penetration depth of the electric field into the DBRs. Using the approximate formula  $L_{\text{DBR}} = L_c n_L n_H / [n_c (n_H - n_L)]$  [207, 223], we find  $L_{\text{eff}} = 1.35$   $\mu\text{m}$  and  $\Delta_{S-A} = 54.6$  meV: this agrees with the experimental splitting of 50–55 meV shown in Figure 95. This comparison shows that the coherence of the optical field is maintained over the whole thickness of the central DBR and therefore that the PSM have a quality that enables coherent coupling effects of the kind first reported for III–V coupled microcavities [218].

The parameter  $\beta$  appearing in Eq. (55) is proportional to the oscillator strength of the optical transitions in the nanocrystals. As already discussed earlier in this chapter and in [203], a comparison is possible between the calculated absorption spectrum and the experimental PL spectrum in view of the nearly symmetric lineshapes of the PS luminescence spectra, which is a sign that the thermal contribution to the occupation of the high-energy states is not as important as in other semiconductor systems. When comparing with PL measurements, where only the lowest lying states of each nanocrystal are probed,  $\beta$  has to be interpreted as the oscillator strength “at the band gap” for each nanocrystal in the corresponding PS layer, averaged

over the nonhomogeneous size distribution. This oscillator strength is known to decrease with nanocrystal size [224], because it must go to zero in the limit of a bulk Si crystal with indirect gap. Figure 96 shows the calculated absorption for different values of the parameter  $\beta$  (which for simplicity is taken to be frequency-independent and the same in all the layers). When  $\beta < 10^{-5}$  absorption is concentrated in the cavity peaks, whereas for  $\beta > 10^{-4}$  most of the absorption takes place in the sideband of the mirrors. The experimental indication that the PL intensities in the cavity peaks and in the sideband are comparable (see Fig. 95) points to an optimal value of  $\beta$  between  $10^{-5}$  and  $10^{-4}$ . In the following,  $\beta = 3 \times 10^{-5}$  is assumed.

The parameter  $\beta$  is related to the oscillator strength by

$$\beta = \frac{e^2}{m\omega_0^2} \frac{f}{V} \quad (57)$$

where  $f/V$  is the oscillator strength per unit volume. Taking the volume of a unit cell, the oscillator strength per

cell  $f_{\text{cell}} \simeq 4 \times 10^{-5}$ . This compares well with the values calculated by Delley and Steigmeier [224] for the larger nanocrystals. Also, with this value for the oscillator strength, a radiative decay rate  $\Gamma = 2ne^2\omega f_{\text{cell}}/(3mc^2) \sim 2 \text{ ms}^{-1}$  is obtained, close to the values calculated in [214] for a band gap of 1.6 eV. We may then conclude that the present PSM structures are characterized by nanocrystals with a small oscillator strength; this is consistent with the explanation of the visible PL band in terms of radiative recombination of electron–hole pairs (or excitons) at the band gap of Si nanocrystals, with a slow radiative lifetime in the millisecond range.

Figure 97 shows the calculated absorption (a) and reflectivity (b) for the parameters of the five samples. Note that when the refractive index is a real number, a cavity mismatch alone does not yield a different intensity of luminescence peaks or of the reflectivity dips: on the other hand, a cavity mismatch combined with a complex refractive index produces an appreciable asymmetry between the two peaks, which is similar to the observed one. In our case the imaginary part of the refractive index is provided by the resonance frequency distribution when a finite value of  $\gamma$  is considered: the precise value of  $\gamma$  is unimportant. Because the cavity  $S_1$  (the outer one) gives the largest contribution to the reflectivity and the absorption spectra, when the outer cavity is thicker, the peak at higher wavelengths is more intense (samples “b” and “c”); on the other hand, when the outer cavity  $S_1$  is thinner (samples “d” and “e”), the peak at lower wavelengths is more pronounced. Comparing with the experimental results shown in Figure 95, we can see that the qualitative features with increasing cavity mismatch are well reproduced. In the calculations, the peak positions change very little with the cavity mismatch: the variations observed in Figure 95 are due to slight deviations of sample parameters from the nominal ones.

The results of Figure 96 show two discrepancies compared with the experimental results in Figure 95: the stop band is wider, and the cavity peaks are narrower. Thus it could be asked whether a different choice of the refractive indexes might lead to a better agreement with experiment; in particular, the stop band can be made narrower by choosing a smaller ratio of “high-to-low” refractive index in the DBR. Figure 97 shows the influence of a different refractive index ratio on the absorption spectra. Although with this choice the width of the stop band agrees with the experimental one (not reported here), the peak separation increases because of a decrease of the reflectivity  $R_2$  of the central DBR in Eq. (56), and the peak asymmetry in the presence of a cavity mismatch is reduced; the linewidth of the peaks also increases as a result of the decrease of the reflectivity of the external DBR. Thus a different choice of the refractive indexes would spoil the good agreement between measured and calculated optical

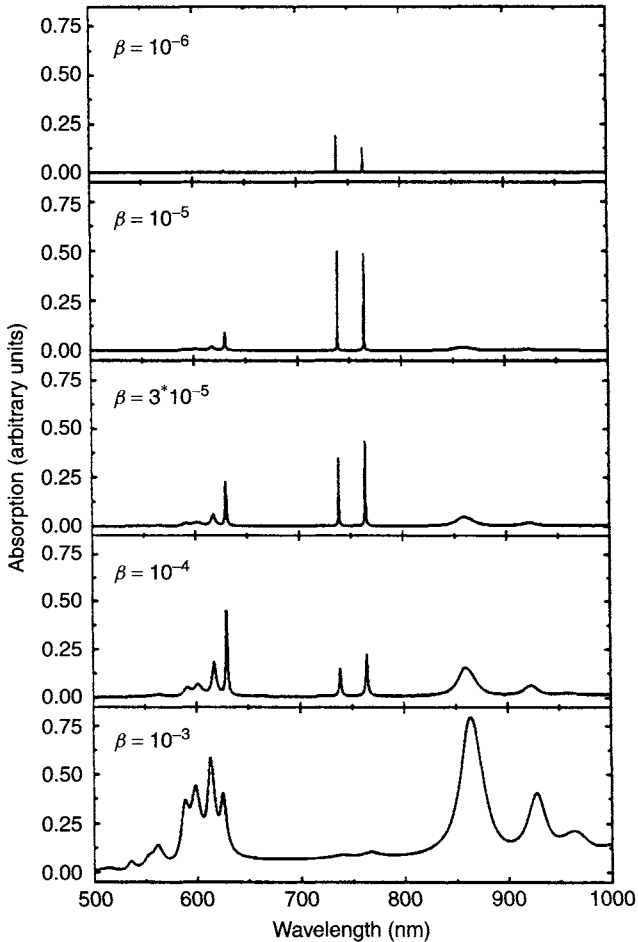


Fig. 96. Absorption of a balanced coupled microcavity as a function of the parameter  $\beta$ . The structure is the same as that used experimentally in Figure 94; parameters of the calculation are given in the text. Adapted from [213].

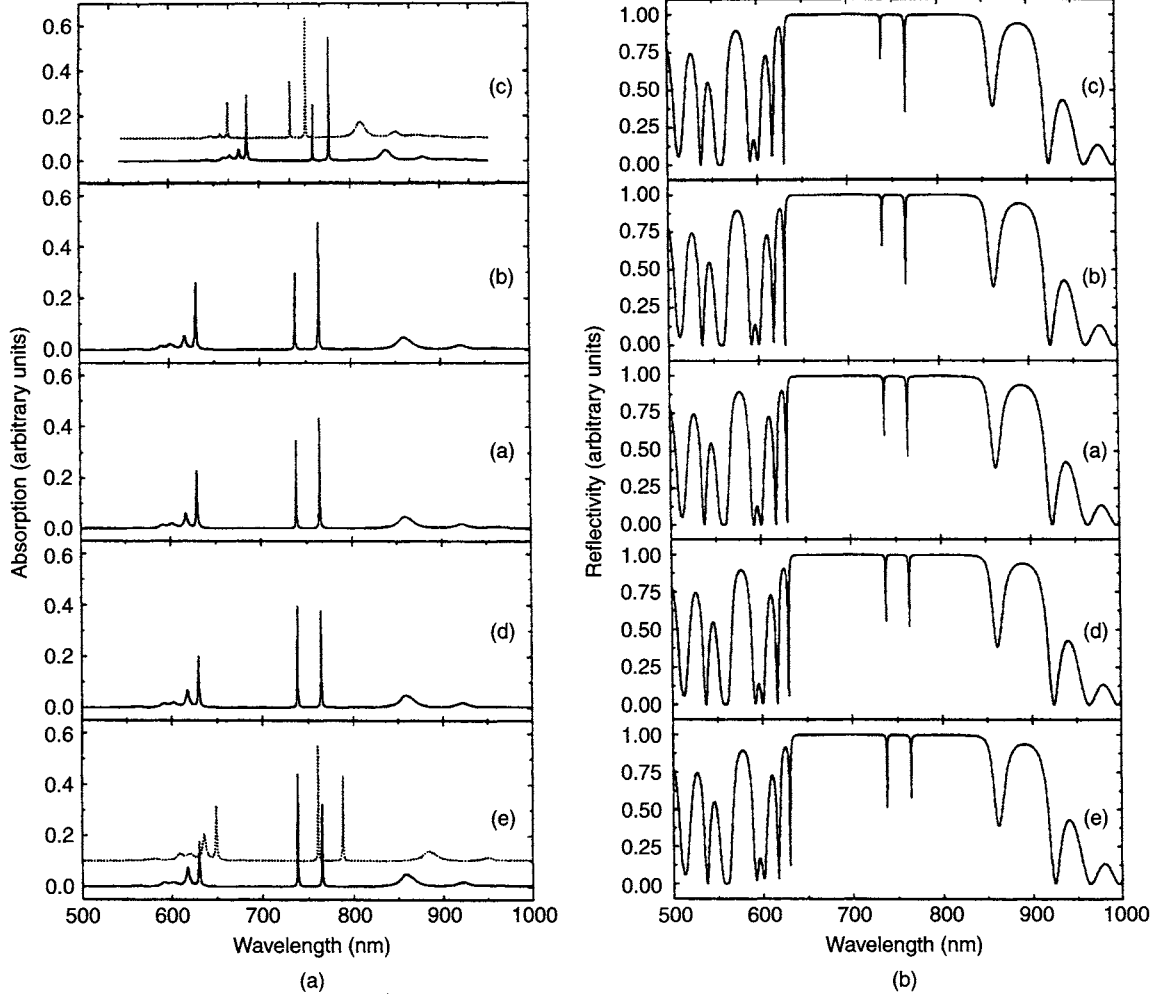


Fig. 97. Absorption (a) and reflectivity (b) spectra of the coupled microcavities for the same structures used in Figure 95. Dotted curve in upper (lower) panel in (a): refractive indexes reduced (increased) by 5% (3%). The labels on the spectra refer to the names of the various samples. Adapted from [213].

splitting. We conclude that the narrower stop band and the broader peaks observed in the experiment do not originate from different values of the refractive indexes, but rather from disorder effects in the DBR [213].

## 7. APPLICATIONS OF POROUS SILICON MULTILAYERS AND MICROCAVITIES

### 7.1. Waveguides

The possibility of varying the refractive index with depth immediately gives the idea of producing PS-based waveguides [225, 226]. This is important in view of the realization of an all-Si-based integrated circuit in which the information is routed through waveguides in form of photons. As an example, a fully integrated optical circuit based on PS has been proposed by Lazarouk et al. [227].

A planar waveguide is composed of a high refractive index layer surrounded by lower refractive index cladding layers. In [225] both planar and strip PS waveguides have been formed on  $0.1 \Omega \text{ cm}$  *p*-type doped silicon wafers by etching a three-layer structure, in which a core layer of 62% porosity is sandwiched between two cladding layers of 75% porosity. Light guidance has been demonstrated for  $1.28 \mu\text{m}$  in as-prepared samples and for  $0.63 \mu\text{m}$  in oxidized samples. Interface roughnesses in the range of 50–100 nm have been observed to concur to the losses in the waveguide. In as-anodized samples losses between  $10$ – $20 \text{ dB cm}^{-1}$  have been measured with multimode guidance for the planar waveguide and single mode behavior for the strip waveguide. The oxidation removes the absorption in the visible and consequently lets the  $0.63 \mu\text{m}$  light be guided. In oxidized samples the losses were between  $6.7$  and  $14 \text{ dB cm}^{-1}$ . This has been attributed to roughness scattering at the interface between the cladding layer and the core layer.

An alternative structure has been proposed in [226], where a core PS region ( $1\text{ }\mu\text{m}$  thick with a refractive index of 1.8 at  $800\text{ nm}$ ) is between a bottom cladding PS layer ( $3\text{-}\mu\text{m}$  thick with  $n = 1.5$ ) and a thin top cladding layer of evaporated Al ( $\simeq 35\text{ nm}$  thick). By surface excitation and looking at the edge, guiding of the light has been observed with polarization dependence. Transverse-electrical (TE) modes are efficiently guided at  $850\text{ nm}$  whereas Transverse-magnetic (TM) modes are not.

## 7.2. Enhancement of Weak Absorption Signals

The possibility of enhancing the absorption intensity of species present in the porous silicon layer embedded by Bragg mirrors [228] has been demonstrated. This is accomplished by tuning the Fabry-Perot maximum of the energy of the absorption transition one wants to enhance. For example, an increase up to 14 times in the infrared absorption band of the Si-H vibration ( $2088\text{ cm}^{-1}$ ) has been measured [228]. This demonstrates the potentiality of PSM for studying the incorporation of species at the surface of PS (see Fig. 98). It also is worth mentioning the proposal to use PSMs, to enhance the Raman intensity of the PS layer embedded in the cavity [228, 229].

## 7.3. Optical Nonlinearities

Another interesting application of PSM can be foreseen in the field of nonlinear optics. The narrow emission line and light confinement effect in the planar optical resonator can be exploited in several nonlinear optical applications such as, for example, second harmonic generation, optical bistability, and all-optical switching. Figure 99 [187] shows the reflectance spectrum of PSM in the resonance

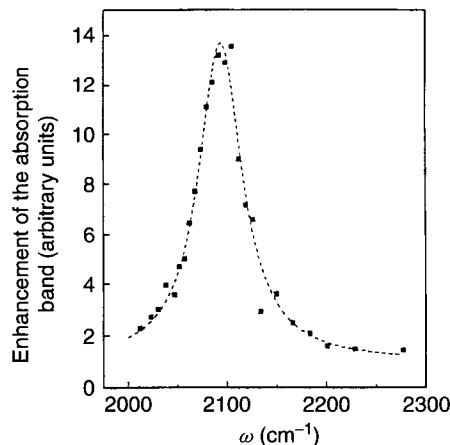


Fig. 98. Enhancement of the absorption band of the Si-H vibration around  $2088\text{ cm}^{-1}$  as a function of the frequency position of the microcavity mode: (black squares) experimental data; (dotted line) a fitting curve. Adapted from [228].

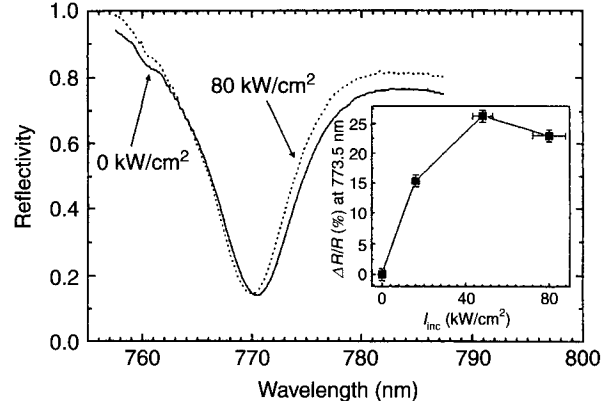


Fig. 99. Normal incidence reflectivity spectra of a PSM for two different CW incident pump powers (at  $514.5\text{ nm}$ ): (dashed line)  $80\text{ kW cm}^2$ ; (solid line) no pump power. The inset shows the pump power dependence of the reflectivity at a fixed observation wavelength. Reprinted with permission after Ref. [187].

region for two different continuous wave pump intensities and in the inset the reflectance for a fixed  $\lambda$  as a function of the CW pump intensity [187, 195]. Two effects were observed comparing low and high pump intensity results: (1) the resonance is shifted at low wavelength, and (2) the reflectance is increased at a fixed  $\lambda$ . Both these facts are a result of the saturation of the absorption at high pump intensities and are observed at a much lower pump power than in single porosity PS samples [230]. The blueshift of the reflectance dip is attributed to a lower effective refractive index value reflecting the saturated absorption. Thermal effects cannot explain these observation because they would yield an increased  $n_c$  and a redshift of the resonance dip. The role of photochemical effects these observations is still unclear.

Second harmonic generation in PSM structures has been reported too [231].

## 7.4. Resonant Cavity Light-Emitting Diodes

The implementation of PSM in light-emitting devices will realize some advantages with respect to conventional LEDs [232–234]:

- (i) spectral purity of the emission with a narrow emission band, which will improve both the color sharpness in flat-panel display applications and the transmission bandwidth for interconnections or data communications;
- (ii) improved directionality in the emission pattern, which will improve the coupling efficiency between the source and the transmission line, and the power efficiency in flat-panel displays, avoiding the loss of optical power along undesired lateral directions;

- (iii) high spontaneous emission intensity, which will increase the internal and external quantum efficiency, resulting in an improved yield of the device.

Two examples of these so-called resonant cavity light emitting diodes (RCLEDs) have been reported in the literature, and some of these properties have been demonstrated [186, 235]. However, both RCLED structures were based on metal contact, which produces an inefficient electrical injection [236].

In [186] by evaporating a thin Al layer (15 nm) on top of a PSM sample a RCLED was realized. When forward biased, the diode showed a weak but measurable electroluminescence. The light intensity versus injected current characteristic (see Fig. 187) is almost linear for low currents and saturates at high current [187]. The RCLED yielded the same light intensity as a reference LED, formed by a  $\lambda_c$ -thick PS layer, but at current densities one order of magnitude lower or at a factor 8 lower electrical power (see the inset of Fig. 100). This was a consequence of a geometrical factor, that is, better collection efficiency of the detection system when the RCLED is used because of the directional emission, and probably of the increased spontaneous emission intensity for the microcavity-based LED. A further, unexpected result was a reduced degradation of the electroluminescence with time for the RCLED with respect to the reference LED.

It is known that atmospheric impregnation causes a degradation of the emission properties of PS LEDs [237]. Vacuum operation [238], deposition of a protective cap layer (e.g., alumina or polycrystalline silicon films) [239],

and oxidation [240] have been used to avoid such problems. It also has been demonstrated that the use of a multilayer film on top of the active layer can have beneficial effects in stabilizing the emission properties: the emission intensity of the reference LED decreased by more than an order of magnitude after 30 min, whereas that of the RCLED decreased by a factor of 4 after 120 min.

In [235] a slightly different structure of RCLED has been demonstrated (Fig. 101) [235]. An active layer was embedded between a bottom DBR and a top 12-nm thick Au layer that served both as top mirror to form the optical cavity (reflectivity of about 40%) and as top electrode to inject the current. When the bias voltage was  $\geq 40$  V, a significant current was flowing through the device and electroluminescence was observed both for forward and inverse biases. This is due to the large RCLED thicknesses caused by the formation of the DBR. The electroluminescence spectrum is shown in Figure 102 in comparison with the PL spectrum of the same sample [235]. One can

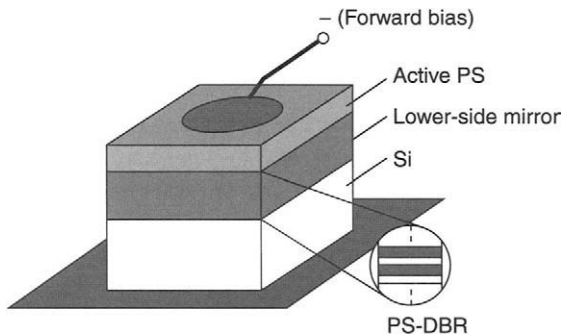


Fig. 101. Schematic structure of the RCLED based on a metal-PS microcavity. Adapted from [235].

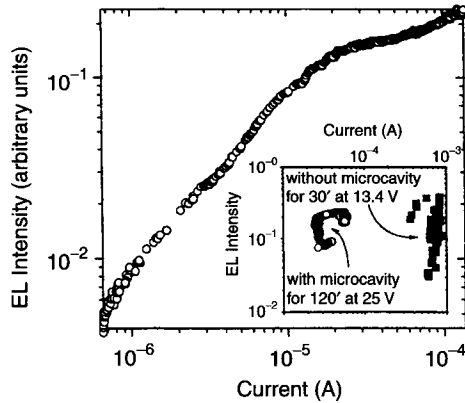


Fig. 100. Electroluminescence intensity versus current (EL-I) curve of a RCLED. Both curves are measured for forward bias (top metal contact negative). The inset shows the EL-I data of the RCLED and of a standard metal-PS LED measured at a fixed voltage as a function of time. In the inset the time goes clockwise. Reprinted with permission after Ref. [187].

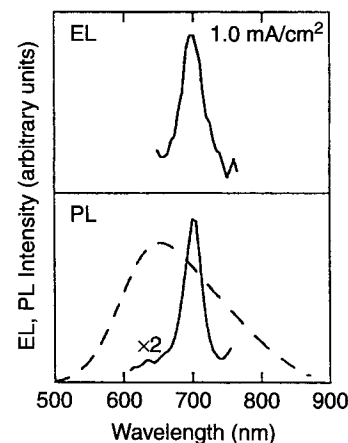


Fig. 102. Electroluminescence (EL) and photoluminescence (PL) spectra of the RCLED shown in Figure 101: (dashed line) luminescence of a reference PS. Adapted from [235].

easily notice that the narrowing of the luminescence band also is preserved in the electroluminescence experiment. The spectral shape is independent of the bias voltage.

### 7.5. Optical Sensor

Nowadays, on-line material and process control rely heavily on optical methods because of their spectral sensitivity, contactless way of measuring and velocity in data evaluation. A simple optical sensor that permits quantitative absorption spectroscopy has been demonstrated using PS-DBR [241]. The layout of the sensor is shown in Figure 103 [242]. It exploits the narrow stopband of the DBR to accomplish the necessary spectral decomposition. The light transmitted or reflected by the sample under investigation impinges onto various DBR and is back-reflected to the detector. The sensor output for a sample to be analyzed is the set of detector readings for each DBR. Several applications of this sensor are reported in [242]:

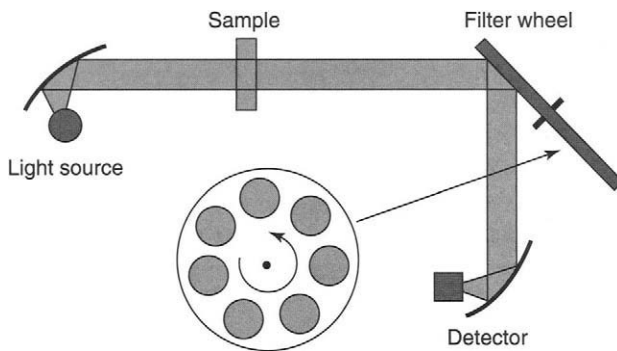


Fig. 103. Basic scheme of an optical sensor. Due to the difficulty in obtaining transmission filters a reflection design has been realized. Various PS DBR form the filter wheel. Reprinted with permission after Ref. [242].

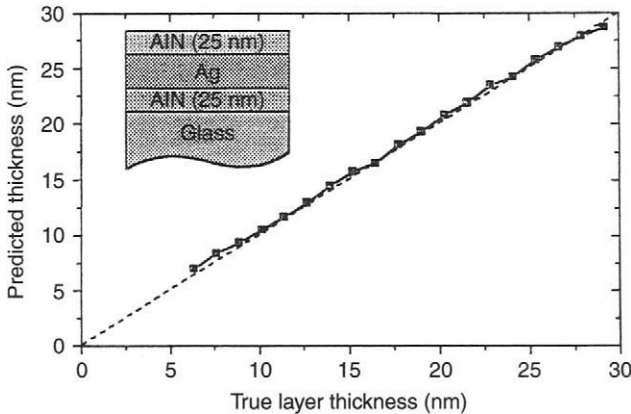


Fig. 104. Comparison of the true Ag layer thicknesses to the ones predicted by the PS-based sensor. The Ag layer was formed by sputtering and was embedded between two AlN layers (25 nm each). Reprinted with permission after Ref. [242], [2].

color recognition, thickness monitoring, and analysis of IR absorption bands. An example is given in Figure 104, where the thickness of a Ag layer deposited onto a glass plate has been measured by measuring the transmittance of the layer with the PS-based optical sensor.

### 7.6. Color Sensitive Photodiodes

Color-sensitive Si photodiodes have been fabricated by using PS interference filters integrated in the  $p^+$  doped part of conventional Si photodiode based on  $p-n$  junctions [243]. The proposed device structure is shown in Figure 105, where the formation of the optical element (either a DBR or a FP) on the top [243] is evidenced. Because of the transparency (at the right wavelengths) and the high resistivity of the PS multilayer, the photoelectrons are mainly generated in the bottom Si layer and not in the PS layer. Hence the PS layer acts simply as a passive element. The processing of the samples is very simple and it has the main advantage over the other approaches of being an inexpensive technology (compared with the cost of depositing multilayers of  $\text{Si}_3\text{N}_4$ ,  $\text{SiO}_2$ , or  $\text{TiO}_2$  by sputtering). A complication appeared for the formation of the PS multilayer structures, as the  $p-n$  diode has to be reverse biased to form PS in the  $p$ -type region. The structure has to be illuminated during etching, which causes a variation both in the porosities and in the thicknesses of the layers. In turn this caused a deterioration of the reflectance quality of the DBR or FP structures so formed. However, preliminary demonstrators have been fabricated and the performance tested. Figure 106 shows the external quantum efficiency in short-circuit conditions of a diode with a DBR in comparison with a reference diode and with the reflectance of the DBR [243]. The spectral response

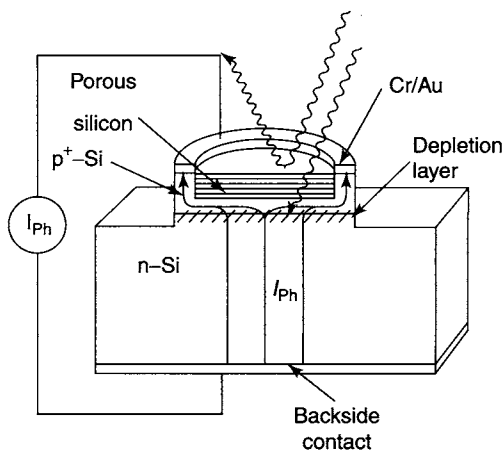


Fig. 105. Device geometry of the Si photodiode with a PS multilayer stack in the  $p^+$ -type-doped top layer of the  $p-n$  photodiode. The photocurrent flows through the crystalline Si as indicated. Adapted from [243].

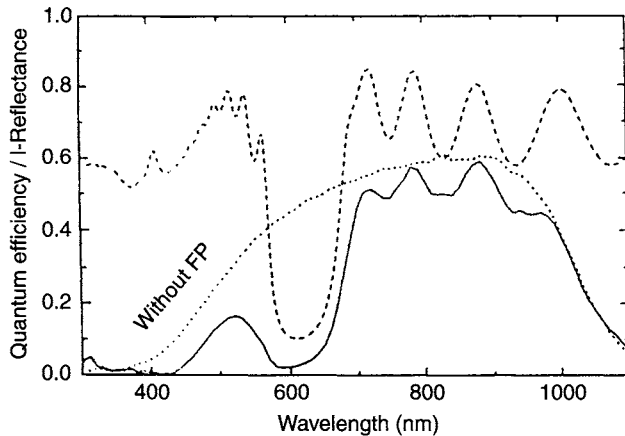


Fig. 106. External quantum efficiency (full line) of the photodiode of Figure 105 integrated with a DBR. This is compared with a reference diode without the FP filter (dotted line). The transmission through the DBR is estimated as  $1 - R$  (dashed line). Adapted from [243].

of the  $p-n$  diode is modified with almost no signal in the DBR stop band region at 600 nm.

### 7.7. Metal–Porous Silicon Microcavities

Figure 107 shows the processing steps for metal–porous silicon microcavities [206, 244]. A  $0.4\text{--}0.6 \Omega \text{ cm}$   $p$ -type doped substrate was employed. First, the active layer was formed by anodization with a current density of  $200 \text{ mA cm}^{-2}$  and a time duration of  $8\text{--}10 \text{ s}$ . The time duration was adjusted such that  $nd = m\lambda_c$ , where  $m$  is an integer.

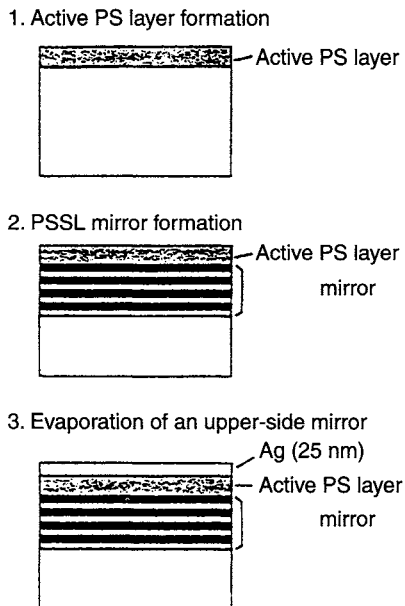


Fig. 107. Schematic structure and fabrication process of a metal–porous silicon microcavity. Adapted from [244].

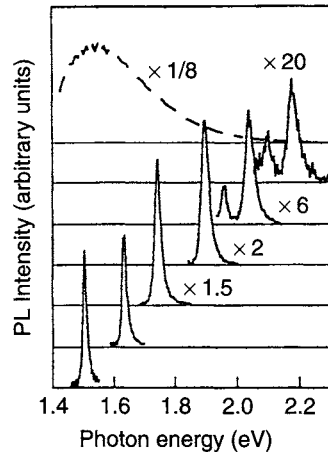


Fig. 108. The narrowed luminescence emission of six metal–porous silicon microcavities (solid curves) compared with the luminescence of a reference PS layer (dashed curve). Adapted from [244].

Then a DBR was formed, which was made by 20 periods of PS layers with  $n_H = 2.5$  and  $n_L = 1.5$  (current densities 20 and  $200 \text{ mA cm}^{-2}$ , respectively). Finally, a thin Ag film ( $\approx 25 \text{ nm}$  thick) was evaporated onto the top surface and used as a mirror and electrical contact. The reflectivity of the Ag film was higher than 90% in the wavelength region of interest. The reflectivity of the bottom DBR had a value of about 0.9 in the stop band [206].

This microcavity structure is thus different with respect to the PSM of the previous sections because the top DBR is substituted by the Ag mirror.

The luminescence spectra of some metal–porous silicon microcavities are reported in Figure 108 [244]. A narrowing of the emission line down to 17 meV, that is,  $\Delta\lambda = 7.7 \text{ nm}$ , is obtained. The emission energy can be continuously tuned across the visible range by simply changing the thickness of the active PS layer (and accordingly of the layers composing the Bragg reflectors) [244]. No enhancement in the emission intensity was detected for the metal–porous silicon microcavities, probably because of the low values for the reflectivity of the confining cavity. One could expect a stronger shortening of the time decays of the luminescence than for PSM, as a result of the better properties of the top metallic mirror with respect to the DBR.

By increasing the active layer thickness, multimode behavior in the waveguide-like structure is observed, and the emission linewidth is significantly decreased [206]. Side-mode peaks become apparent as a result of the narrowing of the free spectral range as the cavity length is increased. The narrowest linewidth (6 meV, i.e.,  $\Delta\lambda = 2.7 \text{ nm}$ ) is measured for  $nd = 10\lambda_c$ .

## 8. CONCLUSIONS

The fascinating world of low-dimensional Si structures has only now entered its infancy. It is our belief that low-dimensional Si structures coupled with low-dimensional photonic systems can play a major role in photonics, as we have underlined throughout this chapter. However, there are still many unfolded properties of these systems.

We are now starting to understand the physics of PS and to control its physical parameters to exploit its various properties. Table XVII indicates many prospective applications of PS. In Table XVIII a comparison of PS with other Si-based light-emitting systems is performed. As a result, PS emerges as the most promising material

for developing Si-based LEDs. The recent improvements in the engineering of the PS surface, the demonstration of a full integration of PS-LEDs with both BJT or CMOS circuits, and the use of microcavities to control the PS spontaneous emission are all recent results that point to an even brighter future for PS.

The mastering of the etching process to form PS layers of designed parameters has allowed the formation of high-quality dielectric multilayers with a competitive technique. VLSI compatibility, easy procedure, and low cost of the experimental apparatus are all characteristics that render the anodic dissolution of Si very appealing, toward the realization of Si-compatible dielectric films. Optical devices (mirrors, filters, waveguides), optoelectronic

Table XVII Potential Application Areas of PS

Application area	Role of PS	Key property
Optoelectronics	LED	Efficient electroluminescence
	Waveguide	Tunability of refractive index
	Field emitter	Hot carrier emission
	Optical memory	Nonlinear properties
Microoptics	Fabry-Perot filters	Refractive index modulation
	Photonic band gap	
	Structures	Regular macropore array
Energy conversion	All optical switching	Highly nonlinear properties
	Antireflection coatings	Low refractive index
	Photoelectrochemical cells	Photocorrosion cells
Environmental monitoring	Gas sensing	Ambient sensitive properties
	Microcapacitor	High specific surface area
	Insulator layer	High resistance
Microelectronics	Low- <i>k</i> material	Electrical properties
	Buffer layer in heteroepitaxy	Variable lattice parameter
	SOI wafers	High etching selectivity
Wafer technology	Thick sacrificial layer	Highly controllable etching parameters
	Tissue bonding	Tunable chemical reactivity
Micromachining	Biosensor	Enzyme immobilization
Biotechnology		

Source: Adapted from [1].

Table XVIII Comparison Among Some Properties of Various Si-Based Light-Emitting Systems and of Prospective Applications<sup>a</sup>

Material	Starting date	LED efficiency (%)	Modulation speed (MHz)	Peak emission ( $\mu\text{m}$ )	Spectral width (meV)	Stability
PS	1990	>1	10	0.65–0.8	200 <sup>b</sup>	≥ Weeks
SiGe	1974	—	11	1.32	100	Good
Er:Si	1983	0.05	1	1.54	16	Years
Nano-Si	1992	0.05	>10	0.4	200	Hours
Silicides	1995	0.02	—	1.5	3.5	—
Multilayers	1995	0.01	—	0.5–0.8	200	Hours (Si/CaF <sub>2</sub> ) Weeks (Si/SiO <sub>2</sub> )
Displays		>1	>0.001	BGR	100 meV	10 <sup>3</sup> –10 <sup>5</sup> Hours
Interconnects		>10	>100	any	—	>10 <sup>5</sup>

<sup>a</sup>The presented data comes from a survey performed at the EMRS meeting (June 1998).

<sup>b</sup>With PSM it can be as small as 4 meV.

devices (optical sensors, photodiodes, LEDs), and microcavities have all been demonstrated, based on these structures.

In particular, for microcavities, both interesting fundamental physical properties and appealing device applications can be envisaged in the near future. The study of their physics is at the very beginning. The fundamental problem of a microcavity filled with a disordered array of silicon quantum dots still has to be tackled theoretically. Experimentally the luminescence and transport properties of the microcavities are beginning to be unfolded and more work should be performed. All the nonlinear optical properties, such as the possibility of observation of superradiance effects or of stimulated emission, have not yet been addressed.

We think, then, that PS as a material basis for optoelectronics is going to reach maturity in the near future, as the recent appearance of all-PS-based optoelectronics devices demonstrates.

## ACKNOWLEDGMENTS

The first author acknowledges the Department of Physics of the University of Pittsburgh for support during the writing of the manuscript, in particular Prof. J. Levy and Prof. S. A. Dytman.

The second author acknowledges the Department of Physics of Trinity College in Dublin, in particular Prof. J. G. Lunney.

The work on PS has been carried out within the POESIA (Porosity Effects in Silicon for Applications) collaboration of the University of Trento. We acknowledge fruitful discussions and exchanges with C. Andreani, P. Bellutti, O. Bisi, G. Björk, A. Borghesi, L. T. Canham, N. Capuj, H. Cruz, A. Kavokin, N. Koshida, D. Luis, G. Mariotto, S. Ossicini, L. G. Panzarini, V. Pellegrini, B. Pivac, F. Rocca, E. H. Roman, A. Tredicucci, and E. Zanghellini. The hard work of previous students and group members has permitted attainment of many of the results presented in these notes: C. Armellini, M. Ceschini, R. Chierchia, P. Dubos, Z. Gaburro, G. Giebel, R. Guardini, C. Mazzoleni, E. Moser, V. Mulloni, and G. Pucker are gratefully thanked.

The work at University of Pittsburgh was supported by a research assistantship of the Physics Department there.

The work at Trinity College was supported by a studentship of the Physics Department.

The work at University of Trento is presently supported by CNR Grant 97.01383.PF48, by EC within programs INCO-COPERNICUS 977037 and ESPRIT MEL-ARI 28741, by NATO Grant HTECH CRG 971562, by INFM program LUNA. The fine Si wafers have been provided by MEMC Electronic Materials (Novara/Merano Italy).

## REFERENCES

1. A. G. Cullis, L. T. Canham, and P. D. J. Calcott, *J. Appl. Phys.* 82, 909 (1997).
2. L. Pavesi, *Riv. Nuovo Cimento* 10, 1 (1997).
3. L. Pavesi and P. Dubos, *Semicond. Sci. Technol.* 12, 570 (1997)
4. A. Uhlir, *Bell Syst. Tech. J.* 35, 333 (1956).
5. L. Pavesi, *Microelectron. J.* 27, 437 (1996).
6. S. Setzu, G. Lerondel, and R. Romestain, *J. Appl. Phys.* 84, 3129 (1998).
7. A. Halimaoui, in "Properties of Porous Silicon" (L. T. Canham, Ed.), p. 12. IEE INSPEC, London, 1997.
8. R. L. Smith and S. D. Collins, *J. Appl. Phys.* 71, R1 (1992).
9. L. Canham, *New Scientist* 23 (April 1993).
10. H. Foll, *Appl. Phys. A* 53, 8 (1991).
11. M. I. J. Beale, J. D. Benjamin, M. J. Uren, N. G. Chew, and A. G. Cullis, *J. Cryst. Growth* 73, 622 (1985).
12. M. J. Eddowes, *J. Electroanal. Chem.* 280, 297 (1990).
13. C. Pickering, M. I. J. Beale, D. J. Robbins, P. J. Pearson, and R. Greef, *Phys. C* 17, 6535 (1984).
14. V. Lehmann and H. Foll, *J. Electrochem. Soc.* 137, 653 (1990).
15. V. Lehmann and U. Gösele, *Appl. Phys. Lett.* 58, 856 (1991).
16. L. Pavesi and V. Mulloni, *J. Lumin.* 80, 43 (1999).
17. L. Pavesi, *J. Appl. Phys.* 80, 216 (1996).
18. V. Lehmann, in "Porous Silicon Science and Technology" (J. C. Vial and J. Derrien, Eds. Editions de Physique, Paris 1995).
19. C. Mazzoleni, Tesi di Laurea, Università di Trento, unpublished, 1995.
20. L. T. Canham, A. G. Cullis, G. Pickering, O. D. Dosser, T. I. Cox, and T. P. Lynch, *Nature* 368, 133 (1994).
21. G. Amato and N. Brunetto, *Mater. Lett.* 26, 295 (1996).
22. O. Belmont, D. Bellet, and Y. Brechet, *J. Appl. Phys.* 79, 7586 (1996).
23. U. Gruning and A. Yelon, *Thin Solid Films* 255, 135 (1995).
24. D. Bellet, in "Properties of Porous Silicon" (L. T. Canham, Ed.) p. 38 IEE INSPEC, London, 1997.
25. L. Pavesi and R. Guardini, *Brazilian J. Phys.* 26, 151 (1996).
26. D. Bellet, S. Billat, G. Dolino, M. Ligeon, and F. Muller, *Solid State Commun.* 86, 51 (1993).
27. J. M. Perez, J. Billabo, P. McNeill, J. Prasad, R. Cheek, J. Kelber, J. P. Stevens, and R. Glosser, *Appl. Phys. Lett.* 61, 563 (1992).
28. S. Schupper, S. L. Friedman, M. A. Marcus, D. L. Adler, Y. H. Xie, F. M. Ross, T. D. Harris, W. L. Brown, Y. J. Chabal, L. E. Brus, and P. H. Citrin, *Phys. Rev. Lett.* 72, 2648 (1994).
29. A. G. Cullis and L. T. Canham, *Nature* 353, 335 (1991).
30. A. Borghesi, A. Sassella, B. Pivac, and L. Pavesi, *Solid State Commun.* 87, 1 (1993).
31. A. Borghesi, G. Guizzetti, A. Sassella, O. Bisi, and L. Pavesi, *Solid State Commun.* 89, 615 (1994).
32. L. T. Canham and A. J. Groszek, *J. Appl. Phys.* 72, 1558 (1992).
33. M. S. Brandt and M. Stutzmann, *Appl. Phys. Lett.* 63, 2569 (1992).
34. F. Koch and V. Petrova-Koch, in "Porous Silicon" Z. C. Feng and R. Tsu, Eds.) p. 133; World Scientific, 1995; F. Koch, V. Petrova-Koch, and T. Muschik, *J. Lumin.* 57, 271 (1993).
35. P. Buseck, J. Cowley, and Le Roy Eyring, "High Resolution Transmission Electron Microscopy and Associated Techniques." Oxford Science, Oxford, 1992.
36. Y. H. Xie, W. L. Wilson, F. M. Ross, J. A. Nucha, E. A. Fitzgerald, J. M. Macauley, and T. D. Harris, *J. Appl. Phys.* 71, 2403 (1992).
37. N. Noguchi, I. Suemune, M. Yamanishi, G. C. Hua, and N. Otsuka, *Jpn. J. Appl. Phys.* 31, L490 (1992).

38. A. G. Cullis, L. T. Canham, and O. D. Dosser, in "Light Emission from Silicon" (S. S. Iyer, R. T. Collins, and L. T. Canham, Eds.), p. 7, Materials Research Society, Pittsburgh, 1992.
39. A. G. Cullis, L. T. Canham, G. M. Williams, P. W. Smith, and O. D. Dosser, *J. Appl. Phys.* 75, 493 (1994).
40. S. F. Chuang, S. D. Collins, and R. L. Smith, *Appl. Phys. Lett.* 55, 1540 (1989).
41. R. Herino, A. Perio, K. Barla, and G. Bomchil, *Mater. Lett.* 2, 519 (1984).
42. G. Bomchil, A. Halimaoui, and R. Herino, *Microelectron. Eng.* 8, 293 (1988).
43. M. W. Cole, J. F. Harvey, R. A. Lux, D. W. Eckhart, and R. Tsu, *Appl. Phys. Lett.* 60, 2800 (1992).
44. K. H. Jung, S. Shih, D. L. Kwong, T. George, T. L. Lin, H. Y. Liu, and J. Zavada, *J. Electrochem. Soc.* 139, 3363 (1992).
45. V. Lehmann, *Adv. Mater.* 4, 762 (1992).
46. V. Lehmann, B. Jobst, T. Muschik, A. Kux, and V. Petrovsk Koch, *Jpn. J. Appl. Phys.* 32, 2095 (1993).
47. A. Nakajima, Y. Oshima, T. Itakura, and Y. Goto, *Appl. Phys. Lett.* 62, 2631 (1993).
48. O. Teschke, M. C. Goncalves, and F. Galembeck, *Appl. Phys. Lett.* 63, 1348 (1993).
49. O. Teschke, F. Alvarez, L. Tessler, and M. U. Kleinke, *Appl. Phys. Lett.* 63, 1927 (1993).
50. I. Berbezier and A. Halimaoui, *J. Appl. Phys.* 74, 5421 (1993).
51. I. Berbezier, in "Porous Silicon Science and Technology" (J. C. Vial and J. Derrien, Eds.). Editions de Physique, Paris 1995.
52. A. Halimaoui, "Porous Silicon Science and Technology" (J. C. Vial and J. Derrien, Eds.). Editions de Physique, Paris 1995.
53. A. Albu-Yaron, S. Bastide, D. Bouchet, N. Brun, C. Colliex, and C. Levy-Clement, *J. Phys. I* 4, 1181 (1994).
54. S. Gardelis, U. Bangert, A. J. Harvey, and B. Hamilton, *J. Electrochem. Soc.* 142, 2094 (1995).
55. A. Grosman, C. Ortega, Y. S. Wang, and M. Gandais, in "Structural and Optical Properties of Porous Silicon Nanostructures," (G. Amato, C. Delerue, and H.-J. von Baerdeleben Eds.). Gordon & Breach Science, Amsterdam, 1997.
56. J. P. Gonchond, A. Halimaoui, and K. Ogura, in "Microscopy of Semiconducting Materials" (A. G. Cullis and N. J. Long, Eds.). IOP Publishing, Bristol, 1991.
57. G. Amato, N. Brunetto, and A. Parisini, *Thin Solid Films* 297, 73 (1997).
58. A. Bruska, E. V. Atrova, U. Falke, T. Raschke, Ch. Radehaus, and M. Hietschold, *Thin Solid Films* 297, 79 (1997).
59. J. M. Gomez-Rodriguez et al., *Appl. Surf. Sci.* 44, 185 (1990).
60. G. B. Amisola, R. Behrensmayer, J. M. Galliga, F. A. Otter, F. Namavar, and N. M. Kalkoran, *Appl. Phys. Lett.* 61, 2595 (1992).
61. T. Yu et al., *J. Vac. Sci. Technol., B* 12, 2437 (1994).
62. C. Tsai et al., *J. Electron. Mater.* 21, 995 (1992).
63. J. L. Coffer, S. C. Lilley, R. A. Martin, and L. A. Files-Sesler, *J. Appl. Phys.* 74, 2094 (1993).
64. E. Ettedgui et al., *Mater. Res. Soc. Symp.* 283, 173 (1993).
65. H. J. Lee et al., *J. Appl. Phys.* 75, 8060 (1994).
66. F. Ruisz et al., *J. Vac. Sci. Technol., A* 12, 2565 (1994).
67. P. M. Fauchet et al., *SPIE Proce.* 2141, 155 (1994).
68. D. Schwall, F. A. Otter, and J. M. Galligan, *Philos. Mag. B* 75, 887 (1997).
69. Ph. Dumas, M. Gu, C. Syrykh, J. K. Gimzewski, I. Makarenko, A. Halimaoui, and F. Salvant, *Europhys. Lett.* 23, 197 (1993).
70. A. Pavlov and Y. Pavlova, *Thin Solid Films* 297, 132 (1997).
71. R. Laiho and A. Pavlov, *Phys. Rev. B* 51, R14774 (1995).
72. R. Laiho, A. Pavlov, and Y. Pavlova, *Thin Solid Films* 297, 138 (1997).
73. E. zur Mühlen, and H. Niehus, *Phys. Status. Solidi B* 190, 21 (1995).
74. O. Teschke, *Appl. Phys. Lett.* 68, 2129 (1996).
75. Y. Tao, R. Laiho, and L. Heikkilä, *J. Vac. Sci. Technol., B* 12, 2437 (1994).
76. Ph. Dumas, M. Gu, C. Syrykh, A. Halimaoui, F. Salvant, J. K. Gimzewski, and R. R. Schlitter, *J. Vac. Sci. Technol., B* 12, 2064 (1994).
77. Ph. Dumas, M. Gu, C. Syrykh, A. Halimaoui, F. Salvant, and J. K. Gimzewski, *J. Vac. Sci. Technol., B* 12, 2067 (1994).
78. K. Ito, S. Ohayama, Y. Uehara, and S. Ushioda, *Appl. Phys. Lett.* 67, 2536 (1995).
79. V. Labunov, V. Bondarenko, L. Glinenko, A. Dorofeev, and L. Tabulina, *Thin Solid Films* 137, 123 (1986).
80. V. Labunov, V. Bondarenko, V. E. Borisenko, and A. Dorofeev, *Phys. Status. Solidi A* 102, 193 (1987).
81. K. Barla, G. Bomchil, R. Herino, J. C. Pfister, and J. Baruchel, *J. Cryst. Growth* 68, 721 (1984).
82. K. Barla, R. Herino, G. Bomchil, J. C. Pfister, and A. Freund, *J. Cryst. Growth* 68, 727 (1984).
83. D. Bellet and G. Dolino, *Thin Solid Films* 276, 1 (1996).
84. H. Sugiyama and O. Nittono, *Jpn. J. Appl. Phys.* 28, 12013 (1989).
85. H. Sugiyama and O. Nittono, *J. Cryst. Growth* 103, 156 (1990).
86. D. Buttard, D. Bellet, and G. Dolino, *J. Appl. Phys.* 79, 8060 (1996).
87. I. M. Young, M. I. J. Beale, and J. D. Benjamin, *Appl. Phys. Lett.* 46, 1133 (1985).
88. K. H. Kim, G. Bai, M. A. Nicolet, and A. Venezia, *J. Appl. Phys.* 69, 2201 (1991).
89. T. Itoh, H. Kiyama, T. Yasumatsu, H. Watanabe, and H. Hiraki, *Physica B* 170, 535 (1991).
90. V. Vezin, P. Goudeau, A. Naudon, A. Halimaoui, and G. Bomchil, *J. Appl. Cryst.* 24, 581 (1991).
91. A. Naudon, P. Goudeau, and V. Vezin, in "Porous Silicon Science and Technology" (J. C. Vial and J. Derrien, Eds.), p. 255. Editions de Physique, Paris 1995.
92. B. K. Teo and D. C. Joy, "EXAFS Spectroscopy and Related Techniques," Plenum, New York, 1981; B. K. Teo, "EXAFS: Basic Principles and Data Analysis," Springer-Verlag, Berlin Heidelberg, 1986.
93. J. Stöhr, in "X-Ray Absorption. Principles, Applications, Techniques of SEXAFS and XANES" (D. C. Koningsberger and R. Prins, Eds.), Vol. 92, p. 443. Wiley, New York, 1988.
94. M. De Crescenzi and M. N. Piancastelli, "Electron Scattering and Related Spectroscopies," World Scientific, Singapore, 1996.
95. G. Dalba, P. Fornasini, M. Grazioli, R. Grisenti, Y. Soldo, and F. Rocca, *Nucl. Instrum. Methods B* 97, 322 (1995).
96. S. Schuppler, S. L. Friedman, M. A. Marcus, D. L. Adler, Y. H. Xie, F. M. Ross, T. D. Harris, W. L. Brown, Y. J. Chabal, L. E. Brus, and P. H. Citrin, *Phys. Rev. Lett.* 72, 2648 (1994).
97. S. Schuppler, S. L. Friedman, M. A. Marcus, D. L. Adler, Y. H. Xie, F. M. Ross, Y. J. Chabal, T. D. Harris, L. E. Brus, W. L. Brown, E. E. Chaban, P. F. Szjowski, S. B. Christman, and P. H. Citrin, *Phys. Rev. B* 52, 4910 (1995).
98. T. van Buuren, Y. Gao, T. Tiedje, J. R. Dhan, and B. M. Way, *Appl. Phys. Lett.* 60, 3013 (1992).
99. T. van Buren, T. Tiedje, S. N. Patitsas, and W. Weydanz, *Phys. Rev. B* 50, 2719 (1994).
100. J. R. Dahn, B. M. Way, E. W. Fuller, W. J. Weydanz, J. S. Tse, D. D. Klug, T. Van Buuren, and T. Tiedje, *J. Appl. Phys.* 75, 1946 (1994).
101. Q. Zhang, and S. C. Bayliss, *J. Appl. Phys.* 79, 1351 (1996).
102. S. C. Bayliss, D. A. Hunt, Q. Zhang, N. Danson, and A. Smith, *Solid State Commun.* 91, 371 (1994).

103. T. K. Sham, D. T. Jang, I. Coulthard, J. W. Lorimer, X. H. Feng, K. H. Tang, S. P. Frigo, R. A. Rosenberg, D. C. Houghton, and B. Bryskiewicz, *Nature* 363, 331 (1993).
104. S. Gardelis, U. Bangert, B. Hamilton, R. F. Pettifer, D. A. Hill, R. Keyse, and D. Teehan, *Appl. Surf. Sci.* 102, 408 (1996).
105. R. F. Pettifer, A. Glanfield, S. Gardelis, B. Hamilton, P. Dawson, and A. D. Smith, *Physica B* 208/209, 484 (1995).
106. G. Dalba, N. Daldosso, D. Diop, P. Fornasini, R. Grisenti, and F. Rocca, *J. Lumin.* 80, 103 (1999).
107. G. Dalba, P. Fornasini, R. Grisenti, N. Daldosso, and F. Rocca, *Appl. Phys. Lett.* 74, 1454 (1999).
108. G. Dalba, N. Daldosso, P. Fornasini, R. Graziola, R. Grisenti, and F. Rocca, *J. Non-Cryst. Solids* 232/234, 232 (1998).
109. W. Lang, in "Properties of Porous Silicon" (L. T. Canham, Ed.) p. 138. IEE INSPEC, London, 1997.
110. G. Gesele, J. Linsmelier, V. Drach, J. Frike, and R. Arens-Fischer, *J. Phys. D* 30, 2911 (1997).
111. D. Bellet, in "Properties of Porous Silicon" (L. T. Canham, Ed.) p. 127 IEE INSPEC, London, 1997.
112. L. J. Gibson and M. F. Ashby, in "Cellular Solids: Structure and Properties." Pergamon, New York, 1988.
113. K. Barla, R. Herino, G. Bomchil, J. C. Pfister, and A. Freund, *J. Cryst. Growth* 68, 727 (1984).
114. T. H. Metzger et al., in "Properties of Porous Silicon" (L. T. Canham, Ed.), p. 112. IEE INSPEC, London, 1997.
115. G. Dolino, G. Bellet, and C. Faivre, *Phys. Rev. B* 54, 17919 (1996).
116. H. Yoon and M. S. Goorsky, *Mater. Res. Soc. Symp. Proc.* 378, 893 (1995).
117. T. Ito, T. Yasamatsu, H. Watabe, and A. Hirachi, *Jpn. J. Appl. Phys.* 29, 1201 (1990).
118. D. Buttard, D. Bellet, and G. Dolino, *J. Appl. Phys.* 79, 8060 (1996).
119. G. Dolino and G. Bellet, in "Properties of Porous Silicon" (L. T. Canham, Ed.), p. 118. IEE INSPEC, London, 1997.
120. S. P. Duttagupta and M. P. Fauchet, in "Properties of Porous Silicon" (L. T. Canham, Ed.), p. 132. IEE INSPEC, London, 1997.
121. G. Mariotto, F. Ziglio, and F. L. Freire, Jr., *J. Non-Cryst. Solids* 192/193, 253 (1995).
122. H. Richter, Z. P. Wang, and L. Ley, *Solid State Commun.* 39, 625 (1981).
123. I. H. Campbell and M. P. Fauchet, *Solid State Commun.* 58, 739 (1986).
124. N. Daldosso, F. Rocca, G. Dalba, P. Fornasini, and R. Grisenti, *J. Porous Mater.* 169–172 (1998).
125. R. Bomchil, R. Herino, K. Barla, and J. C. Pfister, *J. Electrochem. Soc.* 130, 1611 (1983).
126. R. Herino, in "Properties of Porous Silicon" (L. T. Canham, Ed.) p. 89. IEE INSPEC, London 1997.
127. S. Braunauer, P. H. Emmett, and E. Teller, *J. Am. Chem. Soc.* 60, 309 (1938).
128. E. P. Barrett, L. G. Joyner, and P. P. Halenda, *J. Am. Chem. Soc.* 73, 373 (1951).
129. A. Halimaoui, in "Porous Silicon Science and Technology" (J. C. Vial and J. Derrien, Eds.) p. 50 Editions de Physique, Paris, 1995.
130. A. Venkateswara, F. Ozanam, and J. N. Chazalviel, *J. Electrochem. Soc.* 138, 153 (1991).
131. A. Grosman and C. Ortega, in "Properties of Porous Silicon" (L. T. Canham, Ed.) p. 145 IEE INSPEC, London 1997.
132. N. Hadj Zoubir, M. Vergnat, T. Delatour, A. Burneau, and P. de Donato, *Appl. Phys. Lett.* 65, 82 (1994).
133. L. T. Canham, M. R. Houlton, W. Y. Leong, C. Pickering, and J. M. Keen, *J. Appl. Phys.* 70, 422 (1991).
134. S. Banerjee, K. L. Narasimhan, and A. Sardesai, *Phys. Rev. B* 49, 2915 (1994).
135. D. Petit, J. N. Chazalviel, F. Ozanam, and F. Devreux, *Appl. Phys. Lett.* 70, 191 (1997).
136. C. Ortega, J. Siejka, and G. Vizkelethy, *Nucl. Instrum. Methods* 45, 622 (1990).
137. L. Calliari, M. Anderle, M. Ceschin, L. Pavesi, G. Mariotto, and O. Bisi, *J. Lumin.* 57, 83 (1993); L. Pavesi, L. Calliari, E. Zanghellini, G. Mariotto, M. Anderle, and O. Bisi, in "Porous Silicon Science and Technology" (J. C. Vial and J. Derrien, Eds.) p. 61 Editions de Physique, Paris 1995.
138. H. J. Von Bardeleben, D. Stivenard, A. Grosman, C. Ortega, and J. Siejka, *Phys. Rev. B* 47, 10889 (1993).
139. B. Pivac, B. Rakvin, and L. Pavesi, *Appl. Phys. Lett.* 65, 3260 (1994).
140. R. F. Pettifer, A. Glanfield, S. Gardelis, B. Hamilton, P. Dawson, and A. D. Smith, *Physica B* 208/209, 484 (1995).
141. A. Loni, A. J. Simons, L. T. Canham, H. J. Philips, and L. G. Earwaker, *J. Appl. Phys.* 76, 2825 (1994).
142. L. Pavesi, G. Mariotto, O. Bisi, M. Anderle, and L. Calliari, in "Physical Concepts and Materials for Novel Optoelectronic Device Applications II," SPIE, Vol. 1985, p. 632, 1993.
143. L. T. Canham, "Optical Properties of Low Dimensional Silicon Structures" (D. C. Benshuel, L. T. Canham, and S. Ossicini, Eds.), NATO ASI Series Vol. 244, p. 81. Kluwer Academic, Dordrecht, 1993.
144. A. Bsiesy, A. Gaspard, R. Herino, M. Ligeon, F. Muller, and J. C. OBerlin, *J. Electrochem. Soc.* 138, 3450 (1991).
145. L. T. Canham, in "Properties of Porous Silicon" (L. T. Canham, Ed.), p. 158, IEE INSPEC, London, 1997.
146. A. Nakajima, T. Itakura, S. Watanabe, and N. Nakayama, *Appl. Phys. Lett.* 61, 46 (1992).
147. X. Y. Hou et al., *Appl. Phys. Lett.* 62, 1097 (1992).
148. T. Giaddui et al., *J. Phys. D: Appl. Phys.* 29, 1580 (1996).
149. S. P. Duttagupta, L. Tsybeskov, P. M. Fauchet, E. Ettegui, and Y. Gao, *Mater. Res. Soc. Symp. Proc.* 358, 381 (1995).
150. A. C. Dillon, M. B. Robinson, M. Y. Han, and S. M. George, *J. Electrochem. Soc.* 139, 537 (1992).
151. J. A. Glass, E. A. Wovchko, and J. T. Yates, *Mater. Res. Soc. Symp. Proc.* 358, 537 (1995).
152. E. J. Lee, J. S. Ha, and M. J. Sailor, *Mater. Res. Soc. Symp. Proc.* 358, 387 (1995).
153. N. Y. Kim and P. E. Laibinis, *J. Am. Chem. Soc.* 119, 2297 (1997).
154. K. H. Li, C. Tsai, J. C. Campbell, M. Kovar, and J. M. White, *J. Electron. Mater.* 23, 409 (1994).
155. J. L. Cofer, S. C. Lilley, R. A. Martin, and L. A. Files-Sesler, *J. Appl. Phys.* 74, 2094 (1993).
156. P. D. J. Calcott, in "Properties of Porous Silicon" (L. T. Canham, Ed.) p. 203 IEE INSPECs, London, 1997.
157. W. Thei, *Festerkörperprobleme—Advances in Solid State Physics* 33, 149 (1994).
158. J. C. Maxwell-Garnett, *Philos. Trans. Roy. Soc. London.* 203, 385 (1904).
159. D. A. G. Bruggeman, *Ann. Phys.* 24, 636 (1925).
160. H. Looyenga, *Physica* 31, 401 (1965).
161. L. Pavesi and V. Mulloni, *J. Lumin.* 90, 43–52 (1999).
162. P. M. Fauchet, L. Tsybeskov, S. P. Duttagupta, and K. D. Hirschman, *Thin Solid Films* 297, 254 (1997).
163. H. Mizuno, H. Koyama, and N. Koshida, *Appl. Phys. Lett.* 69, 3779 (1996).
164. P. M. Fauchet, and J. von Behren, *Phys. Status. Solidi B* 204, R7 (1997).
165. L. T. Canham, *Appl. Phys. Lett.* 57, 1046 (1990).

166. L. Tsybeskov, Y. V. Vandyshov, and P. M. Fauchet, *Phys. Rev. B* 49, 7821 (1994).
167. A. Kux, D. Kovalev, and F. Koch, *Appl. Phys. Lett.* 66, 49 (1995); A. Kux, D. Kovalev, and F. Koch, *Thin Solid Films* 255, 143 (1995).
168. P. M. Fauchet, E. Ettedgui, A. Raisanen, L. J. Brillson, F. Seifert, S. K. Kurinec, Y. Gao, C. Peng, and L. Tsybeskov, *Mater. Res. Soc. Symp. Proc.* 298, 271 (1993).
169. F. Koch, *Mater. Res. Soc. Symp. Proc.* 298, 319 (1993).
170. G. Pfister and H. Scher, *Adv. Phys.* 27, 747 (1978).
171. H. Scher, M. F. Shlesinger, and J. T. Bendler, *Phys. Today* 44, 26 (January 1991).
172. H. E. Roman and L. Pavesi, *J. Phys.: Condens. Matter* 8, 5161 (1996).
173. P. D. J. Calcott, K. J. Nash, L. T. Canham, M. J. Kane, and T. Brumhead, *J. Phys.: Condens. Matter* 5, L91 (1993).
174. T. Maruyama and S. Ohtani, *Appl. Phys. Lett.* 65, 1346 (1994).
175. F. Muller, R. Herino, M. Ligeon, F. Gaspard, R. Romestain, J.-C. Vial, and A. Bsiesy, *J. Lumin.* 57, 283 (1993); I. Mihalcescu, F. Muller, R. Romestain, and J.-C. Vial, *J. Lumin.* 57, 111 (1993).
176. S. Shih, C. Tsai, H. K. Li, K. H. Jung, J. C. Campbell, and D. L. Kwong, *Appl. Phys. Lett.* 60, 633 (1992).
177. V. Petrova-Koch, T. Muschik, A. Kux, B. K. Meyer, F. Koch, and V. Lehmann, *Appl. Phys. Lett.* 61, 943 (1992).
178. H. J. Von Bardeleben, C. Ortega, A. Grosman, V. Morazzani, J. Siejka, and D. Stivenard, *J. Lumin.* 57, 301 (1993).
179. M. A. Tischler, R. T. Collins, J. H. Stathis, and J. C. Tsang, *Appl. Phys. Lett.* 60, 639 (1992).
180. R. Czaputa, R. Friztl, and A. Popitsch, *Thin Solid Films* 255, 212 (1995).
181. M. Born and E. Wolf, "Principle of Optics." Pergamon, Oxford, 1980.
182. C. Weisbuch, in "Proceedings of the 22nd International Conference on the Physics of Semiconductors" (D. J. Lockwood, Ed.) p. 1839. World Scientific, Singapore, 1995.
183. S. Haroche and D. Kleppner, *Phys. Today* 24 (January 1989).
184. E. M. Purcell, *Phys. Rev. B* 69, 681 (1946).
185. G. Björk and Y. Yamamoto, in "Spontaneous Emission and Laser Oscillation in Microcavities" (H. Yokoyama and K. Ujihara, Ed.), p. 189. CRC Press, London, 1995.
186. L. Pavesi, R. Guardini, and C. Mazzoleni, *Solid. State Commun.* 97, 1051 (1996).
187. L. Pavesi, C. Mazzoleni, R. Guardini, M. Cazzanelli, V. Pellegrini, and A. Tredicucci, *Nuovo Cimento D* 18 1213 (1996).
188. E. Yablonovitch, *J. Opt. Soc. Am. B* 10, 283 (1993).
189. Y. Yamamoto, S. Machida, K. Igeta, and G. Björk, in "Coherence, Amplification and Quantum Effects in Semiconductor Lasers" (Y. Yamamoto Ed.), p. 561. Wiley, New York, 1991.
190. V. Savona, C. Piermarocchi, A. Quattropani, P. Schwendimann, and F. Tassone, in "New Aspects in Optical Properties of Nanostructures," special issue of *Phase Transitions* (1998).
191. J. F. McGilp, *Prog. Surf. Sci.* 49, 1 (1995).
192. St. Frohnhoff, M. G. Berger, M. Thonissen, C. Dieker, L. Vescan, H. Munder, and H. Luth, *Thin Solid Films* 255, 59 (1995).
193. G. Vincent, *Appl. Phys. Lett.* 64, 2367 (1994).
194. M. G. Berger, C. Dieker, M. Thonissen, L. Vescan, H. Luth, H. Munder, W. Thei, M. Wernke, and P. Grosse, *J. Phys. D: Appl. Phys.* 27, 1333 (1994).
195. M. Cazzanelli, Tesi di Laurea, Università degli Studi di Trento, unpublished, 1996.
196. S. Frohnhoff and M. Berger, *Adv. Mater.* 12, 963 (1994).
197. M. G. Berger, R. Arens-Fisher, M. Thonissen, M. Kruger, S. Billat, H. Luth, S. Hilbrich, W. Theiss, and P. Grosse, *Thin Solid Films* 297, 237 (1997).
198. C. Mazzoleni and L. Pavesi, *Appl. Phys. Lett.* 67, 2983 (1995).
199. L. Pavesi, C. Mazzoleni, A. Tredicucci, and V. Pellegrini, *Appl. Phys. Lett.* 67, 3280 (1995).
200. M. G. Berger, M. Thonissen, R. Arens-Fisher, H. Munder, H. Lutz, M. Arntzen, and W. Thei, *Thin Solid Films* 255, 313 (1995).
201. L. Pavesi, G. Giebel, F. Ziglio, G. Mariotto, F. Priolo, S. U. Campisano, and C. Spinella, *Appl. Phys. Lett.* 65, 2182 (1994).
202. M. G. Berger, R. Arens-Fisher, S. Frohnhoff, C. Dieker, K. Winz, H. Munder, H. Luth, M. Artzen, W. Theiss, *Mater. Res. Soc. Symp. Proc.* 358, 327 (1995).
203. V. Pellegrini, A. Tredicucci, C. Mazzoleni, and L. Pavesi, *Phys. Rev. B* 52, R14328 (1995).
204. M. Thonissen, M. G. Berger, M. Kruger, W. Theiss, S. Hilbrich, R. Arens-Fisher, S. Billat, and H. Luth, *Mater. Res. Soc. Symp. Proc.* 45, 643 (1997).
205. G. Lerondel, P. Ferrand, and R. Romestain, *Mater. Res. Soc. Symp. Proc.* 452, 711 (1997).
206. M. Araki, H. Koyama, and N. Koshida, *Jpn. J. Appl. Phys.* 2B 35, 1041 (1996).
207. V. Savona, L. C. Andreani, P. Schwendimann, and A. Quattropani, *Solid State Commun.* 93, 733 (1995).
208. Y. Yamamoto, S. Machida, and G. Björk, *Surf. Sci.* 267, 605 (1992).
209. A. Tredicucci, Y. Chen, V. Pellegrini, and C. Deparis, *Appl. Phys. Lett.* 66, 2388 (1995).
210. J. C. Vial, A. Bsiesy, F. Gaspard, R. Herino, M. Ligeon, F. Muller, R. Romestain, and R. M. MacFarlane, *Phys. Rev. B* 45, 14171 (1992).
211. M. Cazzanelli, C. Vinegoni, and L. Pavesi, *J. Appl. Phys.* 85, 1760 (1999).
212. V. Mulloni, C. Mazzoleni, and L. Pavesi, unpublished.
213. L. Pavesi, G. Panzarini, and L. C. Andreani, *Phys. Rev. B* 58, 15794 (1998).
214. C. Delerue, M. Lannoo, and G. Allan, *J. Lumin.* 57, 249 (1993).
215. L. Pavesi, M. Cazzanelli, and O. Bisi, *Mater. Res. Soc. Symp. Proc.* 452, 717 (1997); M. Cazzanelli and L. Pavesi, *Phys. Rev. B* 56 15264 (1998).
216. D. I. Babic and S. W. Corzine, *IEEE J. Quantum Electron.* 28, 514 (1992).
217. E. Snoeks, A. Lagendijk, and A. Polman, *Phys. Rev. Lett.* 74, 2459 (1995).
218. R. P. Stanley, R. Houdré, U. Oesterle, M. Illegems, and C. Weisbuch, *Appl. Phys. Lett.* 65, 2093 (1994).
219. P. Michler, M. Hilpert, and G. Reiner, *Appl. Phys. Lett.* 70, 2073 (1997).
220. P. Pellandini, R. P. Stanley, R. Houdré, U. Oesterle, M. Illegems, and C. Weisbuch, *Appl. Phys. Lett.* 71, 864 (1997).
221. A. Armitage et al., unpublished.
222. M. Cazzanelli, and L. Pavesi, *Phys. Rev. B* 56, 15264 (1997).
223. H. A. McLeod, "Thin-Film Optical Filters," 2nd ed. Hilger, London, 1986.
224. B. Delley and E. F. Steigmeier, *Phys. Rev. B* 47, 1397 (1993).
225. A. Loni, L. T. Canham, M. G. Berger, R. Arens-Fischer, H. Munder, H. Luth, H. F. Arrand, and T. M. Benson, *Thin Solid Films* 276, 143 (1996).
226. M. Araki, H. Koyama, and N. Koshida, *Appl. Phys. Lett.* 68, 2999 (1996).
227. S. Lazarouk, P. Jaguir, and V. Borisenko, *Phys. Status Solidi A* 1, 87–89 1998.

228. G. Mattei, A. Marucci, and V. A. Yakovlev, *Mater. Sci Eng. B* 51, 158 (1998).
229. A. Fainstein, B. Jusserand, and V. Thierry-Mieg, *Phys. Rev. Lett.* 75, 3764 (1995).
230. V. Dneprovskii, A. Eev, N. Gushina, D. Okorokov, V. Panov, V. Karavanskii, A. Maslov, V. Sokolov, and E. Dovidenco, *Phys. Status Solidi B* 188, 297 (1995).
231. L. A. Golavan et al., *JETP Lett.* 69, 300 (1999).
232. E. F. Schubert, Y. H. Wang, A. Y. Cho, L. W. Tu, and G. J. Zydzik, *Appl. Phys. Lett.* 60, 921 (1992).
233. E. F. Schubert, N. E. J. Hunt, M. Micovic, R. J. Malik, D. L. Sivco, A. Y. Cho, and G. J. Zydzik, *Science* 265, 943 (1994).
234. M. Selim Unlu and S. Strite, *J. Appl. Phys.* 78, 607 (1995).
235. M. Araki, H. Koyama, and N. Koshida, *Appl. Phys. Lett.* 69, 2956 (1996).
236. W. Lang, P. Steiner, and F. Kozlowski, *J. Lumin.* 57, 341 (1993).
237. D. Zhang, Z. Li, W. Hu, and B. Cheng, *Appl. Phys. Lett.* 67, 2431 (1995).
238. A. Loni, A. J. Simmons, T. I. Cox, P. D. J. Calcott, and L. T. Canham, *Electron. Lett.* 31, 1288 (1995).
239. S. Lazarouk, P. Jaguiro, S. Katsouba, G. Masini, S. La Monica, G. Maiello, and A. Ferrari, *Appl. Phys. Lett.* 68, 2108 (1996).
240. K. D. Hirschmann, D. Tsybeskov, S. P. Duttagupta, P. M. Fauchet, *Nature* 384, 338 (1996).
241. S. Hilbrich, R. Arens-Fischer, L. Kupper, W. Theiss, M. G. Berger, M. Kruger, and M. Thonissen, *Thin Solid Films* 297, 250 (1997).
242. W. Thei, R. Arens-Fischer, S. Hilbrich, D. Scheyen, M. G. Berger, M. Kruger, and M. Thonissen, *Mater. Res. Soc. Symp. Proc.* 452, 637 (1997).
243. M. Kruger, M. Marso, M. G. Berger, M. Thonissen, S. Billat, R. Loo, W. Reetz, H. Luth, S. Hilbrich, R. Arens-Fischer, and P. Grosse, *Thin Solid Films* 297, 241 (1997).
244. M. Araki, H. Koyama, and N. Koshida, *J. Appl. Phys.* 80, 4841 (1996).